GROUND PENETRATING RADAR SURVEYING AND SEDIMENT CORING ANALYSIS OF A POST-GLACIAL LAKE, EASTERN NEWFOUNDLAND

by © Jianguang Chen,

A Thesis submitted to the School of Graduate Studies in partial fulfillment of the requirements for the degree of

Master of Science, Department of Earth Sciences /Faculty of Science

Memorial University of Newfoundland

October 2018

St. John’s, Newfoundland and Labrador

Abstract

Ground penetrating radar (GPR) is a relatively newly developed high-frequency electromagnetic technique that has been widely used in the shallow subsurface investigation for the last few decades. Recently, a GPR survey of a small organic-rich post-glacial lake (Grassy Pond) in Eastern Newfoundland shows significant continuous laminations within the lake sediments in the GPR profiles. Since there have been very few GPR stratigraphy studies of lacustrine sediments, the main focus of this project is on the correlation between the sediment stratigraphy and the GPR sub-bottom profiles. Secondary interests are: to estimate the carbon content of a typical small inland lake to help assess how such bodies have contributed to the carbon budget since the last glaciation; and to investigate chemical variability within the sediments.

The work in this project includes GPR surveying, sediment coring, and sediment physical, geochemical and chronostratigraphic data acquisition, calibration and correlation. First of all, 50 and 100 MHz GPR surveys were completed on Grassy Pond when the lake surface was frozen in the winter. Bathymetric and depth-to-bedrock maps were created from the GPR profiles. Based on these two maps, a sediment distribution map was also created and this was used to choose sediment coring locations. Four sediment cores were collected by using a rod-driven piston corer, and additional GPR profiles were collected over these core locations. The cores were then scanned by a Multi-Sensor Core Logger (MSCL) to determine the physical properties. After that, the cores were sub-sampled and geochemically analyzed by ICP-OES. Selected sediment samples were also analyzed for C and N contents and isotopes, and radiocarbon dated. Lastly, the

linkage was made between the geophysical and geochemical data, and a simple GPR forward model was created based on the sediment physical properties to enhance the data interpretation and correlation.

The results show that the lake sediments of Grassy Pond are highly-organic and water-rich. Forward models of EM wave reflections show that the laminated GPR reflections within the sediments are caused by variations in water content. The geochemical analysis shows that the water content is anti-correlated to the lithic elemental concentrations. Since the lithic inputs can reflect past climate changes, we suggest that paleoclimatic changes may ultimately be responsible for the laminations seen in the GPR profiles. The carbon budge of Grassy Pond is calculated based on the sediment volume and average carbon content of the sediments, and it is estimated as 29 kg/m^2, which is significantly higher than forest soils.

Besides these major results, one of our basal sediment samples is dated back to 8.6 radiocarbon years ago, which corresponds to the end of last glaciation in the same region of Newfoundland. The sediments of Grassy Pond are found to be highly enriched in arsenic (As) and molybdenum (Mo), likely associated with the erosion of iron oxide minerals in the surrounding land, as Grassy Pond overlies the alteration zone of a gold prospect. In the deepest sediment core, many elements show a concentration peak near 6.3k years ago when the regional climate started to become drier, and erosion rates increased.

Acknowledgements

After three years of intensively hard work, today is the day: writing the acknowledgement notes is the finishing touch on my thesis. It has been a major step in my life for these years of the M.Sc. program, not only in the scientific arena, but also on a personal level, like a boy becomes a man. Finishing this degree has had a huge impact on me. Therefore, I would like to reflect on the people who have supported and helped me so much throughout this period.

First of all, I would first like to give my biggest appreciation and deepest respect to my supervisor Dr. Alison Leitch for everything. Particularly, I want to thank you for all of the opportunities I was given to conduct my research and all kinds of help during this project. Secondly, I would like to thank my co-supervisor Dr. Elliott Burden for the help with the sediment coring and related analysis.

I would also like to thank Dr. Harunur Rashid for the assistance in the early stage of this project, Dr. Charles Hurich for providing guidance in the GPR modelling, Chris Finch for performing the ICP-OES analysis, Peter Schultheiss for calibrating the MSCL, Carley Crann for the help training me with radiocarbon dating sample preparation, Alison Pye for the help with the isotopic analysis, Dr. Mike Babechuk, Dr. Penny Morrill, and Dr. Susan Ziegler for consultations on geochemical and isotopic analysis, and Adam Wall, Linden Ernst, Drew Jones, and Jason Sylvester for assisting me in the field and lab.

Finally, I want to thank two of my thesis examiners. Thank you for taking your time and effort reviewing my thesis.

Once again, thank you very much, everyone!

Jianguang Chen

St. John’s, March 26, 2018.

P.S. Most of the research in this M.Sc. project was conducted in Memorial University of Newfoundland, St. John’s campus. The financial support was provided from the Hibernia Geophysics Fund.

Table of Contents

List of Figures

List of Tables

List of Appendices

Chapter 1 Introduction

1.1 Objectives and Project Scope

Compared to conventional ground geophysical sub-bottom profiling methods, Ground Penetrating Radar (GPR) is a relatively newly developed high-frequency electromagnetic (EM) technique that has been widely used in the shallow subsurface investigation for the past few decades. Due to the nature of the short wavelength EM waves, GPR can be extremely effective for spatial surveying in the freshwater aquatic systems. Lake sediments can provide continuous, high-resolution, and easy-to-date climate proxies, which are commonly used in paleolimnological studies. Particularly, a recent GPR survey of a small post-glacial lake in the eastern Newfoundland shows significant continuous lake sediment stratigraphy in the GPR sub-bottom profiles. Since very little research effort has been put into GPR stratigraphy studies of lacustrine sediments, the main objective of this project is the correlation of the sediment stratigraphy seen in the GPR sub-bottom profiles with the physical properties of the sediments.

Freshwater aquatic systems have not been considered as important as terrestrial and marine system in the carbon cycle at either global or regional scales since they cover only a small portion of the Earth's surface area. However, a recent study shows freshwater aquatic systems can significantly affect regional carbon balances because they absorb twice as much carbon as is exported from land to the sea (Cole et al., 2007). Therefore, a secondary objective of this project is to calculate the carbon content of a typical small inland water body, to help assess how such bodies have contributed to the carbon budget since the last glaciation.

The work in the project involved GPR surveying, sediment coring, and sediment physical, geochemical and chronostratigraphic data acquisition, calibration and correlation. In the first stage, I used GPR for lake basin analysis because of its good spatial resolution, low cost, easy operation, and reasonable penetrating depth in freshwater systems. Compared with sonar of similar or shorter wavelengths, GPR has lower penetration depths in water but attenuates less in soft sediment. The GPR survey enabled the production of 3D lake bathymetry, bedrock isopach, and sediment distribution maps to guide sediments coring, and the high-resolution GPR profiles of the sub-bottom were processed and used to study the sediment stratigraphy and determine some of physical properties of the sediments. Following the GPR survey, a rod driven piston corer was used to collect lake sediments at suitable locations determined by the bathymetry map and GPR sub-bottom profiles. Then, the sediment cores were scanned by a Multi-Sensor Core Logger (MSCL) to determine physical properties such as density, magnetic susceptibility, electrical resistivity and P-wave velocity. The MSCL was originally designed for marine sediment cores, so the conductivity of freshwater sediments could not be measured effectively by this device. Then, I cut each sediment core into 10 cm intervals after the core logging, and measured the resistivity and chargeability of these samples by using a custom-configured Sample Core I.P. Tester (http://www.gddinstrumentation.com/scip-tester). Additionally, the water content of the samples was calculated by weighing them before and after desiccation, and the sediment samples were sent to the Department of Natural Resources laboratory for bulk geochemical analysis using the ICP-OES method. Selected bulk sediment samples were measured for carbon and nitrogen concentrations and isotopes at the Stable Isotope

Laboratory at Memorial University, and the same samples were taken to the A.E. Lalonde AMS Laboratory at the University of Ottawa to perform C^{14} radiocarbon dating for chronostratigraphic determination. The analyses were carried out by the author under the guidance of Carley Crann. Correlations were made between the different measurements of physical properties and with the geochemical data. Additionally, an electrical impedance log of the sediments was made based on the water content, and simple 1-D forward modelling of the reflections of EM waves from the sediments was compared with GPR profiles to enhance the data interpretation and correlation.

1.2 General Background

Paleolimnology can generally be defined as the study of lake deposits to interpret the past conditions and processes in lake basins, and it is a multi-disciplinary science that involves using physical, chemical and biological methods to investigate the information contained in these sediments (Birks, Lotter, Juggins, & Smol, 2012). Lacustrine sediments are one of the natural archives of earth and ecosystem history that may be of long duration and significantly resolved in time (Cohen, 2003). The initial development of paleolimnology can be dated back approximately two hundred years, and this science has been pursued with various goals over the past two decades. At present, paleolimnology plays a significant role in paleoclimatology, global climate changes, environmental sciences, and even hydrocarbon and mineral resource exploration and exploitation. Applications of paleolimnology range from practical environmental problems like studying the influence of lake acidification (e.g., Schindler, Curtis, Parker, & Stainton, 1996), eutrophication (e.g., Søndergaard, Jensen, & Jeppesen, 2003),

chemical contamination (e.g., Budzinski, Jones, Bellocq, Pierard, & Garrigues, 1997) and erosion (e.g., Eden & Page, 1998), to more fundamental scientific problems like examining hypotheses of biogeography (e.g., Bowman & McCuaig, 2003), evolution (e.g., Pachur, Wünnemann, & Zhang, 1995), climate change models (e.g., Overpeck et al., 1997) and theoretical ecology (e.g., Douglas, Brenner, & Curtis, 2016).

Within the numerous applications of paleolimnology, paleoclimatic reconstruction is probably the most common one because lacustrine sediments contain some of the best proxies of climate change. According to Bradley (1999), the sources of proxy records for paleoclimate reconstruction can be either natural archives, such as marine and lacustrine sediments, loess, ice, cave deposits, and subfossil biological material, or geomorphological features, such as glacial deposits and erosional features. For environmental data derived from these proxies, fine sampling intervals and dating resolutions are essential for paleoclimatic reconstruction. Lakes accumulate sediments from their surrounding environment and so sediment cores recovered from lakes can provide a continuous record of environmental change (Cohen, 2003). In addition, the accumulation rates in lakes can be high, so lacustrine sediments can offer the potential for high-resolution records of past climate, providing they can be adequately dated. Another advantage of using lacustrine sediments for paleoclimatic reconstruction, except in the high arctic, is that they are much easier to collect than other proxy sources such as ice cores and marine sediments.

Since lacustrine sediments contain abundant paleolimnological data, sediment coring or drilling is probably the most common collection method. However, before collecting any sediment samples, a complete sedimentary basin study is very helpful in

choosing coring sites. In the overall sedimentary basin study, maps of bathymetry and the distribution, thickness and stratigraphy of the sediments underlying the lake are required (Brian J Moorman, 2002). Traditional methods for lake bottom and sub-bottom profiling use acoustic techniques, including echo sounding (e.g., Moreno-Amich & Garcia-Berthou, 1989), multi-beam sonar bathymetry mapping (e.g., Morgan et al., 2003), and seismic reflection profiling (e.g., Scholz, 2002). Ground penetrating radar (GPR) is a well-developed, low-cost and non-destructive electromagnetic radiation technique that has been well adapted in the fresh water lacustrine system sub-bottom profiling over past few decades. The biggest advantage of GPR is that it can be used through an ice cover during winter time, while acoustic methods are only effective in open water. Due to the nature of GPR's short wavelength radio waves, this technique can also provide high-resolution sub-bottom profiles for stratigraphic studies, and it is particularly sensitive to changes in water content within sediments.

When the sedimentary basin study is complete, suitable coring locations can be chosen. The retrieval of an unmixed and continuous sediment core is the first and most critical step in the paleolimnological process (Scholz, 2002). There are many types of coring equipment and methods developed for sediment collecting, such as open-barrel and gravity corers (e.g., Gilbert & Glew, 1985; Glew, 1991; Wright, 1990), box corers and dredges (e.g., Hessler & JuMARS, 1974), core catching devices (e.g., Kansanen, Jaakkola, Kulmala, & Suutarinen, 1991), vibracorers (e.g., Sanders & Imbrie, 1963), etc. Lightweight and easy-to-construct rod driven piston corers were specifically developed for lacustrine sediments in the 1950s (Brown, 1956; Livingstone, 1955; Vallentyne, 1955). This coring method is also very suitable for cold-region lakes since it requires a

steady platform (ice cover) to operate.

Lacustrine sediments can reflect sensitively climatic variability and anthropogenic impacts, which can be obtained from physical properties, bulk geochemistry and paleobiological remains (Zolitschka, Mingram, Van Der Gaast, Jansen, & Naumann, 2002). Due to the high demand for research in lacustrine sediments in the recent decades, computer controlled core logging devices have been developed to supplement traditional manual subsampling methods. Now modern core logging devices can provide a non-destructive, rapid and high-resolution means to determine the physical parameters and even bulk geochemistry of sediments cores. For example, a multi-sensor core logger (MSCL) can determine water content, bulk density, magnetic susceptibility and acoustic properties, and it is often the first laboratory instrument to be used in the core logging investigation (Gunn & Best, 1998; Weber, Niessen, Kuhn, & Wiedicke, 1997).

Inductively coupled plasma optical emission spectrometry (ICP-OES) is a popular analytical technique that has been widely used for determining rare-earth elements in geological materials (Lichte, Meier, & Crock, 1987). This method can determine up to 44 elements quantitatively with high precision and accuracy. More conveniently, the CORTEX scanner, an X-ray fluorescence (XRF) scanning system developed at the Netherlands Institute for Sea Research (NIOZ), can qualitatively determine the bulk geochemical composition without breaking the core (Jansen, Van der Gaast, Koster, & Vaars, 1998).

Age determination is essential to down-core paleolimnological investigation for lake-sediment sequences. Accurate and sufficient sediment chronologies can not only help determine the sedimentation rate but also enable comparisons and correlations on

local, regional and global scales (Björck & Wohlfarth, 2002). A traditional lacustrine sediment dating method is annual varve counts (e.g., Lamoureux, 2002), but this method requires sediments deposited under certain conditions. Modern dating techniques have been developed based on the radioactive decay of certain elements, such as ^{210}Pb (e.g., Appleby, 2002) and ^{14}C (e.g., Björck & Wohlfarth, 2002), which provide more accurate and widely adopted results.

1.3 Study Sites

Tippings Pond is the first field site that we investigated during our preliminary geophysical investigation. Tippings Pond is a small inland freshwater pond, which is located at the top of Massey Drive Road, on the outskirts of the city of Corner Brook in the Western Newfoundland (Figure 1.1). It was suggested (H. Rashid, Pers. Comm.) that Tippings Pond might contain a few tens of metres thick sediments, which is ideal for the investigation of both GPR sub-bottom profiling and sediment coring. However, our preliminary geophysical survey on this pond in the winter of 2015 showed the GPR signals could penetrate only a few metres underneath the water surface due to the salinity of the pond. A 200 kHz sonar bottom-profiling survey on this pond followed in the summer of 2015. Although the bathymetry was well mapped in the sonar profiles of Tippings Pond, there was very little information about the sub-bottom of this pond. Lower frequency (12-50 kHz) and dual frequency echo sounders, incorporating a 200 kHz signal with a lower frequency, are used to map soft sediment thicknesses (e.g. Buchanan, 2005; Martin, Spooner, & Williams, 2003), however such systems were not available to us and moreover subtle structures within the soft sediment, seen in our GPR

survey, have not been reported in sonar studies. In addition, the water depth of Tippings Pond was discovered to be too deep for our available sediment coring equipment.

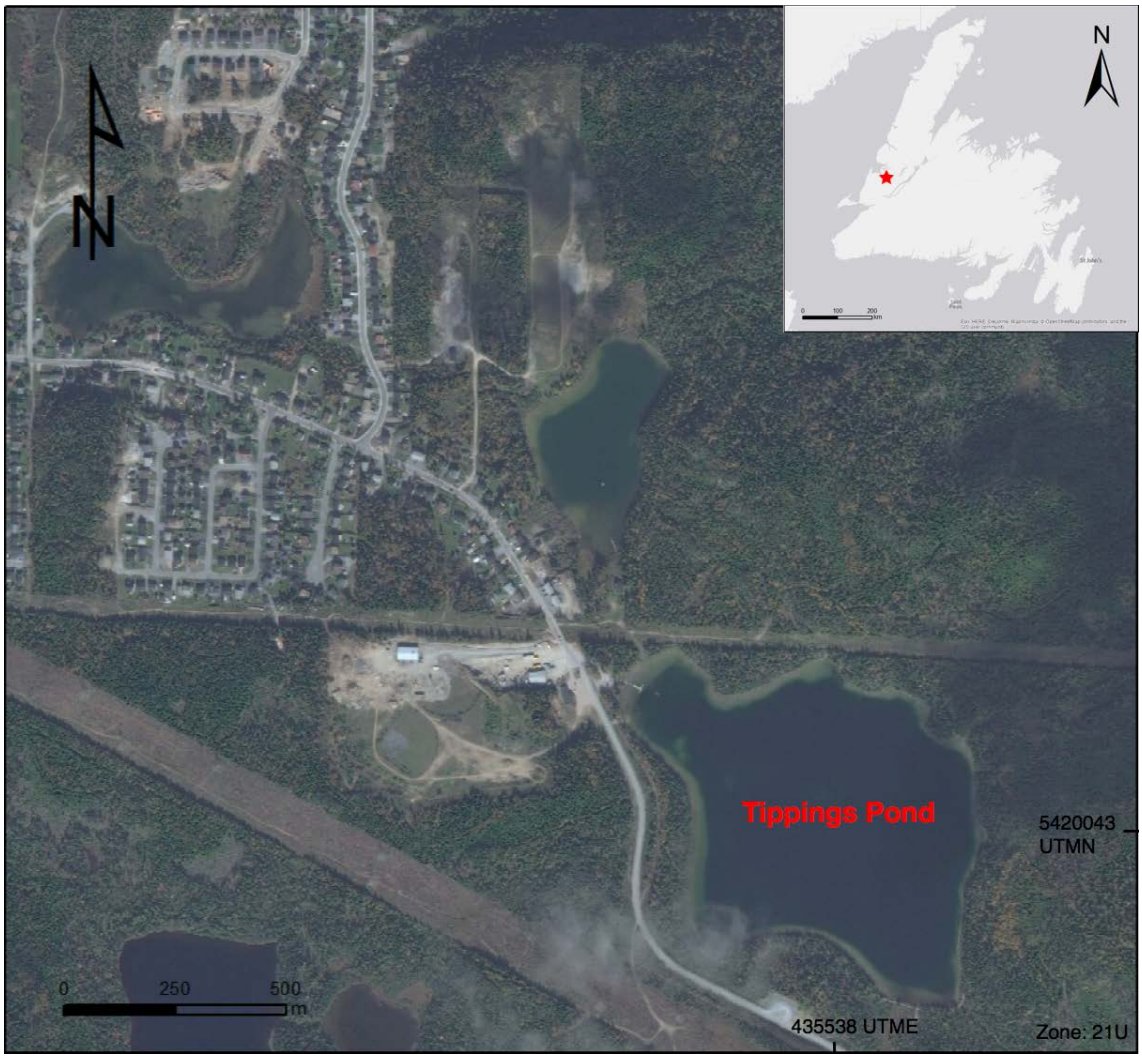

Figure 1.1 Location map of Tippings Pond. This Pond is located at the top of Massey Drive Road, the outskirt of the city of Corner Brook in the Western Newfoundland.

Grassy Pond is the second field site that we investigated during our preliminary geophysical investigation: it is located in the Big Easy Prospect near Thorburn Lake in the Eastern Newfoundland (Figure 1.2). The Big Easy prospect has been identified as a

low-sulphidation-style late-Neoproterozoic epithermal alteration system with significant gold mineralization hosted within sedimentary rocks (Sparkes & Dunning, 2014), and Grassy Pond directly overlies the alteration zone in this prospect (Wall, 2017) (Figure 1.3). Regional lake sediment geochemistry data from the Geological Survey of Newfoundland and Labrador shows that Grassy Pond is also located in the regional positive arsenic anomaly (Department of Natural Resouces, 2018) (Figure 1.3). The GPR data quality from Grassy Pond is excellent: the top and boundaries for soft lake sediments as well as continuous layered structures within the sediments all clearly appear in the GPR sub-bottom profiles. Additionally, the average water depth of Grassy Pond is only a few metres, which is suitable for our current rod-driven piston coring equipment. Therefore, Grassy Pond was chosen to replace Tippings Pond as our main field site for the majority of our studies.

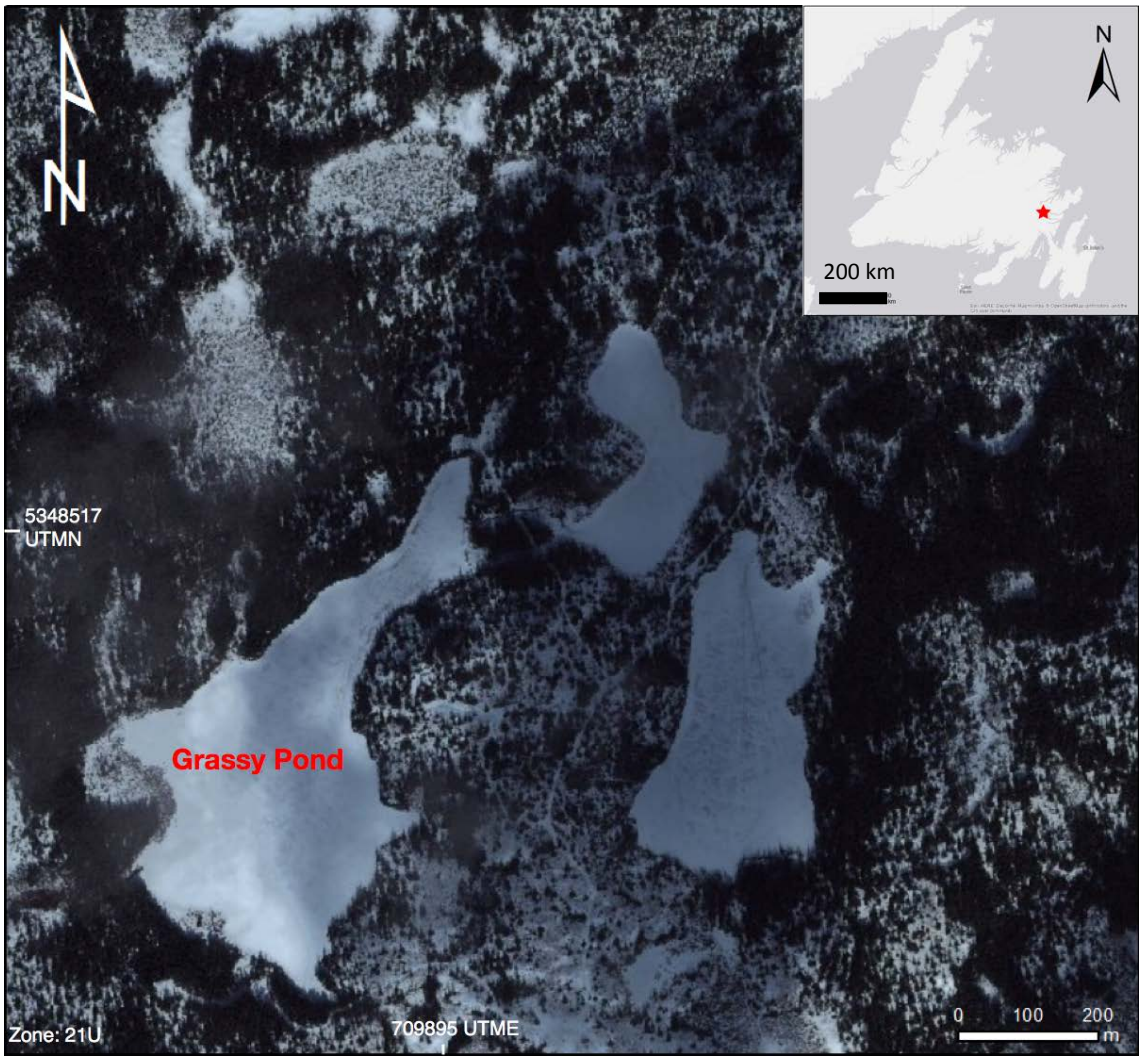

Figure 1.2 Location map of Grassy Pond. This pond is located in the Big Easy Prospect near Thorburn Lake in the Eastern Newfoundland.

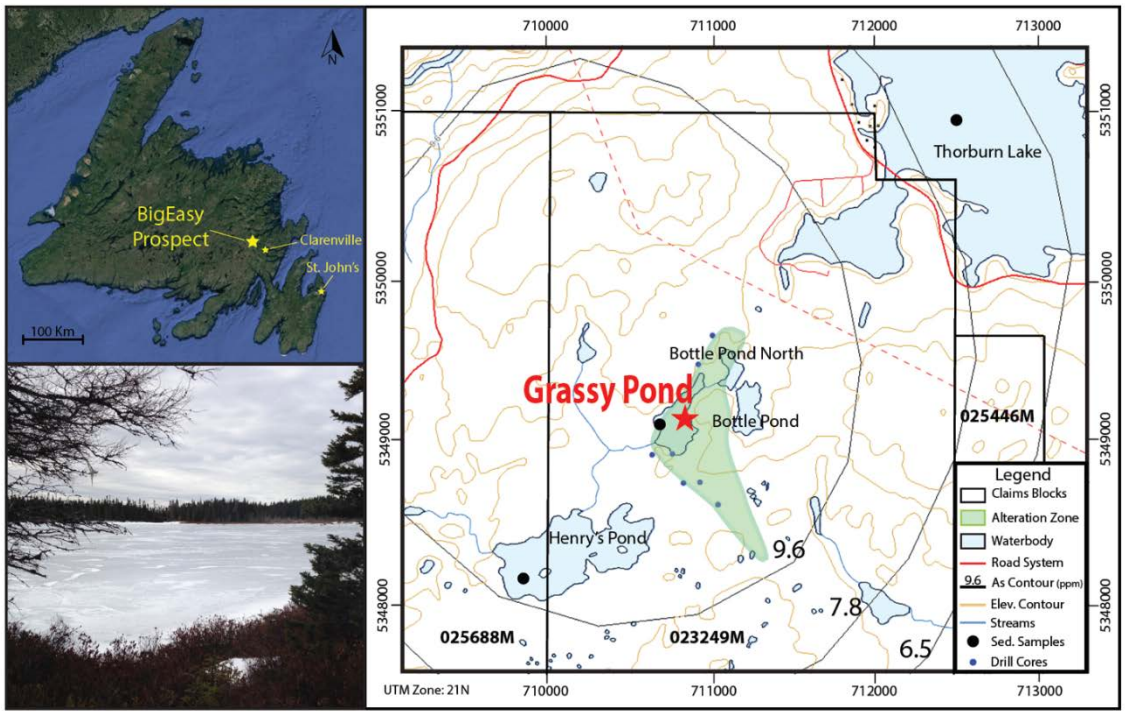

Figure 1.3 Top left: Location of the Big Easy Prospect in Eastern Newfoundland. Right: Location map of Grassy Pond in the Big Easy Prospect. This map also shows regional arsenic contours, regional sampling locations (3 black dots) and the alteration zone. Bottom left: Grassy Pond in the winter when the lake surface is frozen.

Chapter 2 Ground Penetrating Radar Background

Bathymetric and bedrock mapping is an important first step in basin analysis before undertaking any paleolimnological studies because it provides information about the distribution, thickness, and stratigraphy of the sediments underlying the lake. Ground Penetrating Radar (GPR) was chosen for constructing the bathymetric map in this project due to its high-resolution and good penetrating depth for bottom and sub-bottom profiling in the Grassy Pond freshwater system. In addition, GPR provides an excellent solution for wintertime surveying when lakes are covered by ice. Since the GPR surveying is the most important component of this project, this chapter will provide a brief discussion of theoretical concepts underlying GPR operation.

2.1 GPR Instrumentation and System Configuration

Although there have been many GPR system configurations developed for multi-purpose shallow subsurface investigation over last half century, the main components of a GPR system are all very similar. A typical GPR system consists of a transmitter and receiver pair with antennas, a control unit, and an interface, data storage and display module (Figure 2.1a). The transmitter controls the centre frequency and bandwidth of the electromagnetic pulses and generates these pulses, and the receiver amplifies and digitizes the signals reflected from the subsurface and sends them to the control unit. The antennas attached to the transmitter and receiver are usually identical, and they are used to send/capture the electromagnetic signals into/back from the ground. The size of the GPR antennas varies with frequency. The lower the centre frequency, the larger the antennas. The control unit defines the survey parameters and accepts data from the receiver. It is

also able to perform a few simple data processing tasks, such as time gain and dewow (explained in Chapter 3), before the data is real-time displayed. The interface, data storage and display module is often integrated into the control unit in recently developed GPR systems. The most common way the data is displayed is signal amplitude versus two way travel time (TWT) and is referred to as a trace (Daniels, 2004). A single trace is subject to random noise: to improve data quality, several traces are taken at each measurement location and added together in a process known as "stacking". The amplitude of random noise is inversely proportional to the number of stacks. Typically, 8 to 32 stacks are used in GPR surveys. A collection of stacked traces is illustrated as a radargram display (Figure 2.1b). The X axis represents the distance along the survey line for an individual trace, and the Y axis represents the TWT of the signal. The depth is often placed on the other Y axis opposite the TWT. However, the velocity of the EM waves must be known in order to calculate the correct depth scale from the TWT. When the velocity varies in the subsurface, as it often does, the values on the depth axis can only be approximate.

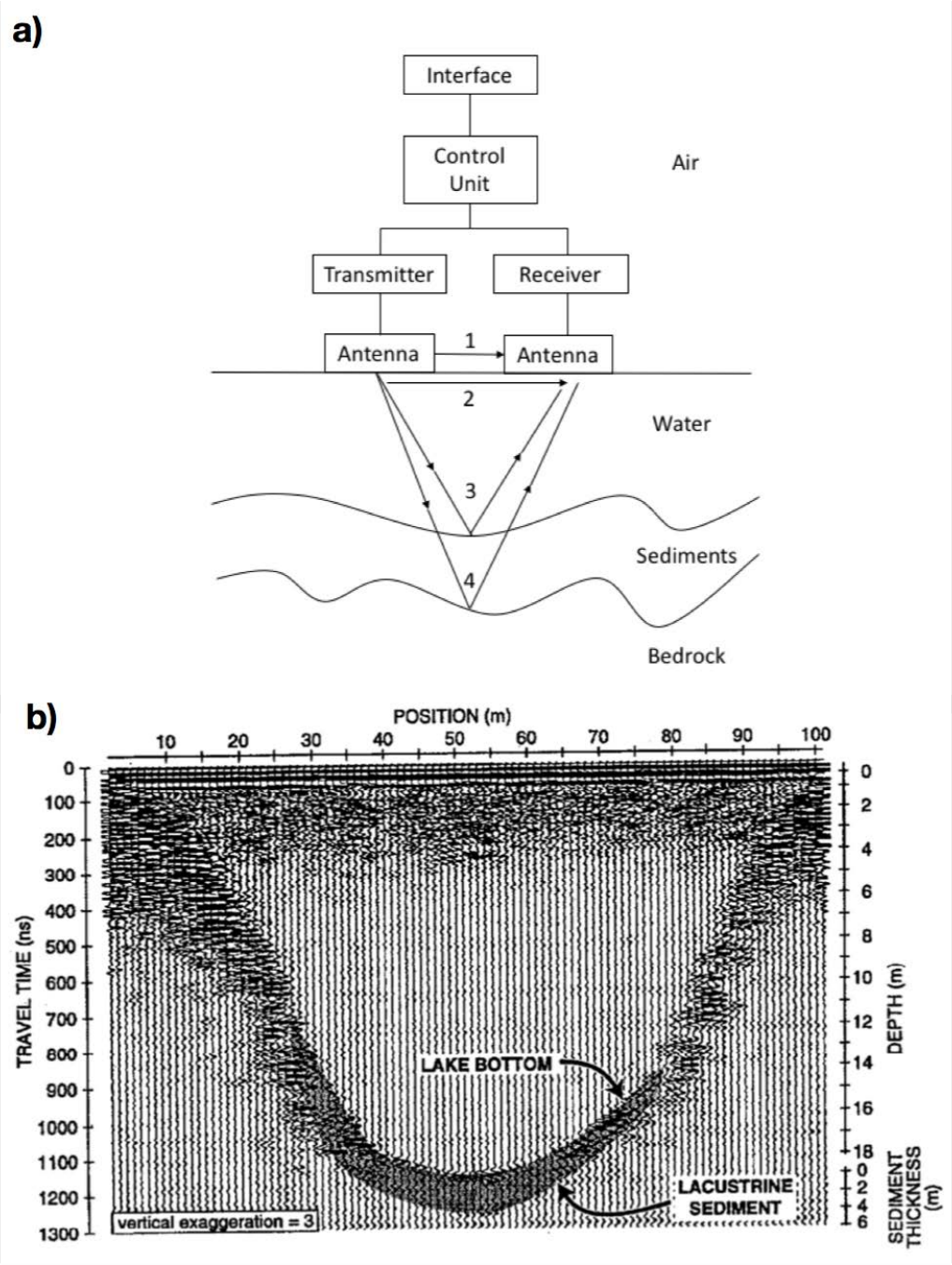

Figure 2.1 a) An overview of GPR system components and typical pulse paths in a freshwater lake. Arrows: 1) direct wave, 2) ground wave, 3 & 4) reflections. Modified from Moorman, 2002. b) GPR profile across Bulb Lake. The shaded area highlights the lacustrine sediment accumulations. (Brian J Moorman & Michel, 1997)

GPR is similar to the seismic reflection method, however GPR uses EM waves

instead of acoustic waves. Unlike seismic waves, the GPR EM waves generated from a given transmitting antenna have a narrow bandwidth with a central frequency in the range of 10 – 1000 MHz. These EM waves propagate into the subsurface until they encounter an object or material with different electrical properties than the surrounding material. The wave is then scattered, with a portion of the wave's energy continuing downward and with a portion of the energy reflected back to surface. The waves reflected back to the surface are captured by the receiver antenna, and the travel information (TWT, measured in nanoseconds) is saved, processed and displayed. As well as reflected waves from subsurface discontinuities, air waves and ground waves are also recorded on a radar trace. The air wave is the first arrival wave that travels between transmitting antenna and receiving antenna through the air at about the speed of light (0.2998 m/ns). The ground wave is the second arrival wave that travels through the ground just under the air-ground interface between these antennas. In addition, lateral waves that reflect from shallow reflectors at the critical angle and then refracted along the ground can be also shown in a radargram (Clough, 1976).

The configuration of a GPR system depends on the survey type. According to A. Annan (2009), GPR surveys can be grouped into reflection and transillumination. In reflection surveys the antennas are next to each other on the same side of the target whereas in transillumination surveys the target is between the transmitter and receiver. Reflection GPR profiling is the dominant survey type that most shallow subsurface researchers use, while transillumination GPR measurements are used mostly in borehole studies for engineering and environmental studies (Olsson, Falk, Forslund, Lundmark, & Sandberg, 1992). Since GPR transillumination surveys are more complicated and not

used in this project, the details for this type of survey will not be discussed in this chapter.

Typical GPR reflection survey types include common-offset reflection surveys (Figure 2.2a) and common midpoint (CMP) reflection surveys (Figure 2.2b). For common-offset reflection surveys, the transmitting and receiving antennas are parallel and placed in a fixed spacing. During the survey, these antennae are moved as a unit along the survey line producing a profile with subsurface reflectivity (in time) versus spatial position. A CMP survey aims to estimate the radar signal velocities in the subsurface material as a function of vertical depth at a certain point. CMP survey antennas are orientated parallel to each other and perpendicular to the survey line on either side of the point and during the survey the spacing between the transmitting and receiving antennas is increased.

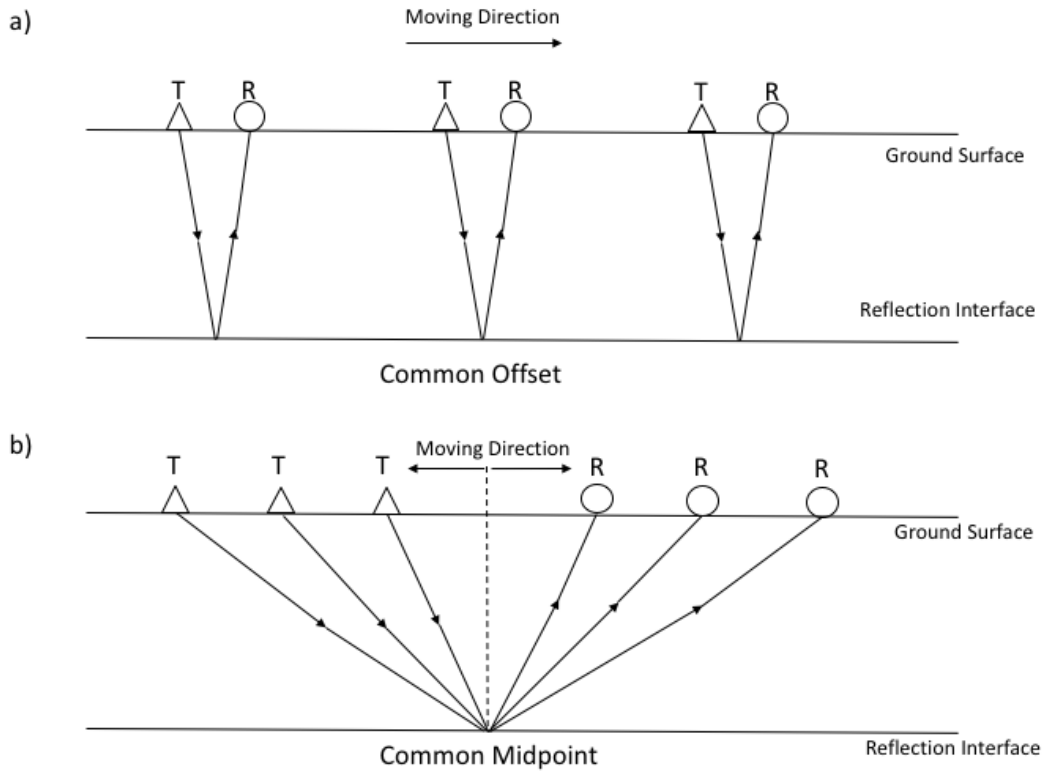

Figure 2.2 Common GPR survey types: a) common offset, b) common midpoint, where T is the transmitter and R is the receiver.

2.2 Maxwell's Equations and Electromagnetic Properties

Since GPR is an EM technique, the foundations of GPR are based on EM theory that can be mathematically described by Maxwell's equations. Cassidy (2009) writes that "Maxwell's Equations are a set of equations that quantitatively summarize the spatially and temporally varying coupled electric and magnetic fields and their interdependence". The equation set contains four basic equations including Gauss's Law for Magnetism (2.1), Faraday's Law of induction (2.2), Gauss's Law (2.3), and Ampere's Law with Maxwell's extension (2.4), which for a linear medium are expressed as follow:

$$\nabla \cdot \boldsymbol{B} = 0 \tag{2.1}$$

$$\nabla \times \boldsymbol{E} = -\frac{\partial \boldsymbol{B}}{\partial t} \tag{2.2}$$

$$\nabla \cdot \boldsymbol{D} = \rho_v \tag{2.3}$$

$$\nabla \times \boldsymbol{H} = \frac{\partial \boldsymbol{D}}{\partial t} + \boldsymbol{J} \tag{2.4}$$

where **B** is the magnetic field [T]; **E** is the electric field (strength) [V/m]; t is time [s]; **D** is the electric displacement field [C/m^2]; ρ_v is the electric charge density [C/m^3]; **H** is the magnetic field intensity [A/m]; and **J** is the electric current density [A/m^2] (Note: **B**, **E**, **D**, and **J** are all vectors).

The electrical and magnetic properties of a material are the parameters of Maxwell's Equations, which can be used to describe the behaviour of GPR's EM field in a material. Constitutive equations (Eq. 2.5, 2.6 & 2.7) can provide a means to relate these properties to an EM field in a macroscopic scale:

$$\boldsymbol{D} = \varepsilon \boldsymbol{E} \tag{2.5}$$

$$\boldsymbol{B} = \mu \boldsymbol{H} \tag{2.6}$$

$$\boldsymbol{J} = \sigma \boldsymbol{E} \tag{2.7}$$

where ε is the dielectric permittivity [F/m]; μ is the magnetic permeability [N/A^2]; and σ is the electrical conductivity [S/m] (Note: ε, μ, and σ are tensor quantities and can also be nonlinear).

Permittivity ε and electrical conductivity σ are electrical properties, while magnetic permeability μ is the magnetic property. Dielectric permittivity is a measure of the polarization of electrical charges that occurs in a medium when an electrical field is applied. Electrical conductivity (which is the reciprocal of electrical resistivity) is the measure of a material's ability to allow the transport of an electric charge. Magnetic

permittivity is a measure of the degree of magnetization that a material obtains in response to an applied magnetic field. For a linear medium, these electrical and magnetic properties are independent of field strength, and they control any EM field behavior, such as movement of charge and energy storage, in a medium.

The electrical and magnetic properties of a material and how they influence EM wave behaviors are the topics of numerous discussions (Cassidy, 2009). The discussion here will be narrowed down to common basic problems related to GPR applications in freshwater systems, such as how the electrical and magnetic material properties of the subsurface materials affect GPR wave propagation and reflection.

2.3 Electromagnetic Wave Propagation

The equation set (E.q. 2.1 – 2.4) can be used to describe the relationship between electrical field and magnetic field when they travel as a coupled electromagnetic field with time. By combining the equations, Maxwell's Equations can be rewritten as:

$$\nabla^2 \boldsymbol{B} = \mu\sigma \frac{\partial \boldsymbol{B}}{\partial t} + \mu\varepsilon \frac{\partial^2 \boldsymbol{B}}{\partial t^2} \tag{2.8}$$

$$\nabla^2 \boldsymbol{E} = \mu\sigma \frac{\partial \boldsymbol{E}}{\partial t} + \mu\varepsilon \frac{\partial^2 \boldsymbol{E}}{\partial t^2} \tag{2.9}$$

In these two equations, the $\mu\sigma \cdot \partial/\partial t$ term is related to conduction currents in the medium and it determines the rate of EM field energy dissipation, while the $\mu\varepsilon \cdot \partial^2/\partial t^2$ term is related to displacement currents due to electrical polarization or separation of charge in the medium and it determines the magnitude of EM field energy storage. The nature of EM field depends on the relative magnitude of these two terms: it can either diffuse into the subsurface (when the $\mu\sigma \cdot \partial/\partial t$ term is significantly larger) or propagate as a wave (when the $\mu\varepsilon \cdot \partial^2/\partial t^2$ term is significantly larger).

While the solving these wave equations can be very complex, there are some simple solutions (e.g., plane wave solutions) that illustrate the nature of wave propagation. Considering a planar EM wave is traveling in the +z direction, the electric and magnetic field terms **E** and **B** can be expressed in the following simplified forms:

$$\boldsymbol{B}(z,t) = \boldsymbol{B}_0 f(z - vt)e^{-\alpha z} \tag{2.10}$$

$$\boldsymbol{E}(z,t) = \boldsymbol{E}_0 f(z - vt)e^{-\alpha z} \tag{2.11}$$

where $\mathbf{E}_0$ and $\mathbf{B}_0$ are the magnitudes of the electric and magnetic field at time = 0; v is the wave propagation speed and α is an attenuation coefficient. This solution describes an EM wave where the shape of the pulse is not changed as it propagates. However, the amplitude of the wave shows an exponential decline with distance.

The relative magnitude of the energy dissipation and storage terms in the Maxwell's Equations (Eq. 8 and 9) and the value of the attenuation coefficient can be determined by the magnitude ratio (MR). Assuming the electrical field **E** and magnetic field **B** are sinusoidally oscillating with a cyclic frequency f (in Hz or cycles/s), the $\mu\sigma \cdot \partial/\partial t$ and $\mu\varepsilon \cdot \partial^2/\partial t^2$ terms in Maxwell's Equations (Eq. 2.8, 2.9) can be approximately expressed as:

$$\left|\frac{\partial \boldsymbol{E}(\boldsymbol{B})}{\partial t}\right| \approx \omega|\boldsymbol{E}(\boldsymbol{B})| \tag{2.12}$$

$$\left|\frac{\partial^2 \boldsymbol{E}(\boldsymbol{B})}{\partial t^2}\right| \approx \omega^2|\boldsymbol{E}(\boldsymbol{B})| \tag{2.13}$$

where $\omega = 2\pi f$ is the angular frequency. Thus, the magnitude ratio (MR) is given by:

$$MR = \frac{\left|\mu\varepsilon\frac{\partial^2 \boldsymbol{E}(\boldsymbol{B})}{\partial t^2}\right|}{\left|\mu\sigma\frac{\partial \boldsymbol{E}(\boldsymbol{B})}{\partial t}\right|} = \frac{\omega^2\varepsilon|\boldsymbol{E}(\boldsymbol{B})|}{\omega\sigma|\boldsymbol{E}(\boldsymbol{B})|} = \omega\frac{\varepsilon}{\sigma} = 2\pi f\frac{\varepsilon}{\sigma} \tag{2.14}$$

Some sources (e.g., Olhoeft, 1998; Santamarina, Klein, & Fam, 2001) use loss factor P

instead of the magnitude ratio MR, where P = 1/MR. If MR is greater than 1, displacement currents dominate and wave propagation occurs. If MR is smaller than 1, conduction currents dominate and diffusion occurs. In particular, if MR >> 1 (that is, P = 1/MR ≈ 0), the influence of conductivity σ can be neglected, and this is called the low-loss condition (e.g., Daniels, 1996). When MR is equal to 1, the frequency in equation (14) becomes the 'transition frequency' f_t (Davis & Annan, 1989; Reynolds, 2011):

$$f_t = \frac{\sigma}{2\pi\varepsilon} \tag{2.15}$$

If the frequency is smaller than f_t, the properties of an EM wave depends on the angular frequency ω ($2\pi f$), which indicates diffusion; if the frequency is larger than f_t, the EM wave velocity becomes frequency-independent.

Since GPR is an electromagnetic wave based method, the GPR operating frequency should always be above the transition frequency in order to insure the EM waves propagate instead of dispersing; it is most effective in low-electrical-loss materials. Then, the $\mu\sigma \cdot \partial/\partial t$ term can be neglected in equation 8 and 9 and the wave equations become:

$$\nabla^2 \boldsymbol{B} = \mu\varepsilon \frac{\partial^2 \boldsymbol{B}}{\partial t^2} \tag{2.16}$$

$$\nabla^2 \boldsymbol{E} = \mu\varepsilon \frac{\partial^2 \boldsymbol{E}}{\partial t^2} \tag{2.17}$$

or for a plane wave propagating in the +z direction:

$$\frac{\partial^2 \boldsymbol{B}}{\partial z^2} = \mu\varepsilon \frac{\partial^2 \boldsymbol{B}}{\partial t^2} \tag{2.18}$$

$$\frac{\partial^2 \boldsymbol{E}}{\partial z^2} = \mu\varepsilon \frac{\partial^2 \boldsymbol{E}}{\partial t^2} \tag{2.19}$$

.

Once the GPR operating frequency is above the transition frequency, the EM wave propagation is limited by scattering loss as the wavelengths approach the particle sizes (Neal, 2004). In addition, water will critically absorb EM energy as the frequency increases toward the relaxation frequency in the 10 – 20 GHz range (Hasted, 1973). Both of these factors limit the upper end of GPR operating frequency range. Hence, since the operating frequency has a significant influence on EM wave propagation, most GPR systems are designed in a frequency range of 10 MHz – 1 GHz.

2.4 Electromagnetic Wave Velocity and Attenuation

The behavior of GPR electromagnetic wave propagation is essentially described by velocity and attenuation (Davis & Annan, 1989). Since the GPR operating frequency (10-1000 MHz) is typically higher than the transition frequency, and magnetic permeability μ does not vary significantly in most geological materials (Davis & Annan, 1989), the velocity and attenuation of GPR EM waves is independent of the frequency but depends heavily on electrical properties (dielectric permittivity ε and electrical conductivity σ). Apart from electrical properties, geometric scattering is another factor that influences EM wave attenuation, which is positive proportional to its frequency (Olhoeft, 1998).

Dielectric permittivity ε is the main material property that controls the GPR EM wave velocity in low-loss conditions. Instead of the permittivity ε itself, the relative permittivity ε_r (referred to as κ in some older sources) is usually used:

$$\varepsilon_r = \frac{\varepsilon}{\varepsilon_0}, \tag{2.20}$$

where ε_0 is dielectric permittivity in a vacuum, and $\varepsilon_0 = 8.85 \times 10^{-12}$ F/m. The velocity of EM waves can be derived from Maxwell's Equations to be:

$$v = \frac{c_o}{\sqrt{\varepsilon_r \mu_r \frac{1 + \sqrt{1 + (\frac{\sigma}{\omega\varepsilon})^2}}{2}}}, \tag{2.21}$$

where c_0 is the velocity of EM waves in a vacuum (3×10^8 m/s), μ_r is the relative magnetic permeability, $\sigma/\omega\varepsilon$ is the loss factor, and $\omega = 2\pi f$ is the angular frequency. In low-loss material, the influence of electrical conductivity σ is minimal, so the loss factor can be neglected (assuming $\sigma/\omega\varepsilon \approx 0$) (A. P. Annan, 2005). Since most common geological materials are nonmagnetic, the relative magnetic permeability can be treated as a constant ($\mu_r \approx 1$) (Davis & Annan, 1989; Neal, 2004; Reynolds, 2011). Thus, the velocity in Eq. (21) can be simplified as:

$$v = \frac{c_0}{\sqrt{\varepsilon_r}} \tag{2.22}$$

The electrical conductivity σ has the greatest influence on the attenuation constant α (In Eq. 10 &11) when an EM wave is propagating (Olhoeft, 1998). The attenuation constant α becomes frequency-independent in low-loss materials, and it can be derived as:

$$\alpha = \frac{\sigma}{2}\sqrt{\frac{\mu}{\varepsilon}}, \tag{2.23}$$

while the impedance Z can be expressed as:

$$Z = \sqrt{\frac{\mu}{\varepsilon}} = \frac{Z_0}{\sqrt{\varepsilon_r}}, \tag{2.24}$$

assuming the magnetic permeability variations are negligible ($\mu_r \approx 1$). Z_0 is the

impedance of a vacuum:

$$Z_o = \sqrt{\frac{\mu_o}{\varepsilon_0}} = 377, \tag{2.25}$$

where μ_0 is the magnetic permeability in a vacuum, and $\mu_0 = 1.25 \times 10^{-6}$ H/m. Thus, the attenuation constant α can be simplified as following (Theimer, Nobes, & Warner, 1994):

$$\alpha = 377 \cdot \frac{\sigma}{2 \cdot \sqrt{\varepsilon_r}} \tag{2.26}$$

Based Eq. (22) & (26), the behavior (velocity and attenuation) of EM wave propagation is mainly controlled by relative dielectric permittivity ε and electrical conductivity σ, respectively. Since the application of GPR is restricted in low-loss materials where the electrical conductivity is relatively small, the dielectric constant is the property that dominantly controls the nature of GPR EM waves. Table (2.1) provides the EM wave properties in a list of freshwater system materials (including water). From this table, freshwater has the highest dielectric constant, so the water content primarily controls the GPR EM wave behavior in these materials. However, for highly conductive materials, such as sea water, contaminated soils and earth material with high-content clay minerals, or for materials containing significant concentrations of magnetic minerals, such as magnetite or haematite, the controlling factors of the EM wave behaviors are much more complicated, and GPR usually does not perform well.

Table 2.1 A list of relative dielectric permittivity, EM wave propagation velocity, DC electrical conductivity, and attenuation constant of common geologic materials at 80 - 120 MHz. (Modified from Moorman, 2002; Neal, 2004. Original source: Davis & Annan, 1989; Theimer et al., 1994; van Overmeeren, 1997; van Heteren et al., 1998.) (Davis & Annan, 1989)(Davis & Annan, 1989)

Material	Relative dielectric	EM wave Velocity	DC Electrical conductivity	Attenuation

	permittivity			
	ε_r	v (m/ns)	σ(S/m)	α (δB/μ)
air	1	0.3	0	0
distilled water	80	0.033	0.01	0.002
fresh water	80	0.033	0.5	0.1
sea water	80	0.01	30000	1000
pure ice	3 - 4	0.16	0.01	0.01
fresh water unsaturated sand	2.55 - 7.5	0.1 - 0.2	0.01	0.01 - 0.14
fresh water saturated sand	20 - 31.5	0.05 - 0.08	0.1 - 1.0	0.03 - 0.5
fresh water unsaturated silt	2.5 - 5	0.09 - 0.12	1 - 100	1 - 300
fresh water saturated silt	22 - 30	0.05 - 0.07	100	1 - 300
silts (various)	5 - 30	0.07	1 - 100	1 - 100
fresh water unsaturated clay	2.5 - 5	0.09 - 0.12	2 - 20	0.28 - 300
fresh water saturated clay	15 - 40	0.05 - 0.07	20 - 1000	0.28 - 300
clays (various)	5 - 40	0.06	2 - 1000	1 - 300
limestone	4 - 8	0.12	0.5 - 2	0.4 - 1
shales	5 - 15	0.09	1 - 100	1 - 100
granite	4 - 6	0.13	0.01 - 1	0.01 - 1

2.5 Reflection, refraction and transmission

GPR is based on detecting and analyzing reflected EM signals from the subsurface, so it is important to understand what causes reflections. The principles of GPR are very similar to seismic reflection. A portion of EM energy will be reflected when it encounters an interface with different electromagnetic properties (ε, σ, or μ) instead of elastic properties for seismic. Since GPR is not effective in high-conductivity and magnetic materials due to attenuation and magnetic relaxation, GPR surveys are generally restricted to environments where the electrical conductivity σ is low and magnetic permeability μ is constant. Anomalies, such as high conductivity metal pipes or clay layers, produce bright reflections but the signal cannot penetrate beneath them. Except in situations where such anomalous features are sought, GPR EM wave reflection is primarily caused by significant discontinuity with relative dielectric permittivity ε_r, and the strength of reflection is proportional to the magnitude of the contrast of ε_r at the interface between two layers . Similar to seismic reflection, the Fresnel reflection coefficient R (and transmission coefficient T) can be used to determine the amount of reflected (transmitted) signal amplitude when the EM signal travels through an interface. For a normally incident ray, the reflection coefficient R is given by:

$$R = \frac{\sqrt{\varepsilon_{r2}} - \sqrt{\varepsilon_{r1}}}{\sqrt{\varepsilon_{r2}} + \sqrt{\varepsilon_{r1}}} \tag{2.27}$$

where ε_{r1} and ε_{r2} are the relative dielectric permittivity of layer 1 and 2 between a reflection interface, and σ and μ are assumed to be unimportant (Neal, 2004; Reynolds, 2011; Van Dam, 2001). Since the EM velocity is directly related to relative dielectric

permittivity (Eq. 23), the reflection coefficient can be also rewritten as:

$$R = \frac{\sqrt{v_2} - \sqrt{v_1}}{\sqrt{v_2} + \sqrt{v_1}} \tag{2.28}$$

where v_1 and v_2 are the EM wave velocity of layer 1 and 2. The value of reflection coefficient R is always in the range of -1 to +1, and the transmission coefficient T is simply:

$$T = 1 - R \tag{2.29}$$

If the ray is not normally incident, the direction of the wave propagation will change when it passes the interface. The changing angel can be determined by Snell's law:

$$\frac{sin\theta_1}{v_1} = \frac{sin\theta_2}{v_2} \tag{2.30}$$

where θ_1 is the angel of incidence, θ_2 is the angel of refraction. Especially, if $v_1 > v_2$, there is a critical angel where EM waves cannot propagate from layer 1 to layer 2 but travel along the interface. This occurs when $\theta_2 = 90^0$ ($\sin\theta_2 = 1$). Thus, the critical angel θ_{crit1} can be determined by:

$$\theta_{crit1} = \arcsin\left(\frac{v_2}{v_1}\right) \tag{2.31}$$

2.6 Resolution and Penetration Depth

Resolution is one of the most important parameters that should be considered in GPR applications because it determines how small an object can be detected. The resolution of GPR systems is the minimum distance at which it has ability to differentiate two close features, and it includes vertical resolution and horizontal resolution (Davis &

Annan, 1989). A sketch (Figure 2.3) can illustrate the mechanism of these two kinds of resolutions.

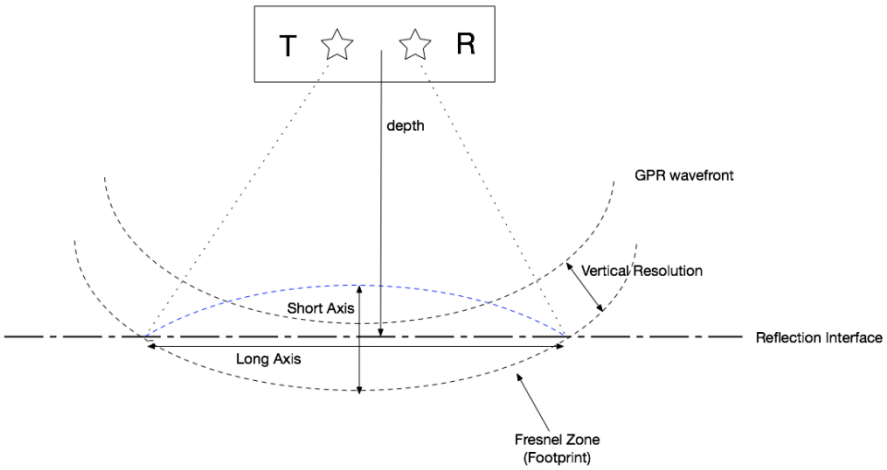

Figure 2.3 A sketch that illustrates vertical and horizontal resolution.

Since GPR detects reflected signals in time, the vertical resolution determines how the system distinguishes two close time pulses in a trace. Assuming two pulses are generated from two close-placed horizontal beds, if the vertical resolution is not sufficient to separate these two pulses, they will overlap, and these two pulses will become a single pulse with a larger amplitude. In order to separate two close-placed reflectors, the distance between the peaks of these two pulses has to be at least a half of their peak width (Davis & Annan, 1989). Thus, the greatest vertical resolution can be expressed as a quarter of the size of the signal wavelength, and it can be applied to most of the wave based methods (A. Annan, 2009):

$$Vertical\ Resolution = \frac{1}{4}\lambda = \frac{v}{4f} \tag{3.32}$$

where λ is the wavelength. Since the wavelength is controlled by the frequency of the signal and its propagation speed in the medium, the vertical resolution is determined by these two factors. A GPR system with higher frequency has finer vertical resolution and can detect smaller reflectors. The vertical resolution changes as the velocity changes between two mediums such as air and water. Overall, the frequency of GPR system is usually the most significant factor in determining resolution because the magnitude of the velocity variations in most common geological materials is not as large as the change of the GPR frequencies. Table 2.2 (Sheriff & Geldart, 1995) gives the theoretical vertical resolution of some common freshwater materials by using 50 and 100 MHz antennas.

Table 2.2 Pulse width and theoretical resolution of 100 MHz and 50 MHz GPR antennas that have a bandwidth to frequency ratio of 1. Modified from Moorman, 2002; Original source: Annan, 1992; Davis & Annan, 1989; Ulriksen, 1982.

Material	100 MHz		50 MHz	
	Pulse width (m)	Theoretical resolution (m)	Pulse width (m)	Theoretical resolution (m)
water	0.033	0.08	0.66	0.16
ice	1.6	0.4	3.2	0.8
saturated sand	0.6	0.15	1.2	0.3
saturated clay	1.0	0.25	2.0	0.5
limestone	1.2	0.3	2.4	0.6
shale	1.0	0.25	2.0	0.5
granite	1.3	0.33	2.6	0.66

The horizontal resolution is the ability to recognize two horizontally placed reflectors rather than one. It is a function of the spacing between GPR traces and the footprint of the radar pulse (Brian J Moorman, 2002). The footprint of a radar pulse is the

area over the reflection interface, and it depends on Fresnel Zone Radius and the depth of the reflector (Figure 2.3). The Fresnel Zone diameter at a reflection interface is equivalent to ½ of wavelength (¼ reflected wavelength + ½ transmitted wavelength). Thus, the footprint can be estimated by the following formula (Brian J Moorman, 2002) :

$$A = \frac{\lambda}{2} + \frac{d}{\sqrt{\varepsilon_r - 1}} \tag{33}$$

where A is the long axis diameter of the oval footprint, d is the depth of the reflecting interface, and the short axis of the oval foot print is about half length of the long axis. In most applications, the trace spacing is more important and also should be smaller than the radar pulse footprint.

The penetrating depth is another important component in GPR applications because it determines how deep the signal can reach. There are several factors that influence the GPR penetrating depth. First of all, the frequency of the GPR system is inversely proportional to the penetrating depth because the EM wave with higher frequency usually has higher scattering loss due to its shorter wavelength, which is getting close to the size of the particles of the subsurface materials. Secondly, the numbers of reflectors and their reflection coefficients (or transmission coefficients) will also affect the penetration depth. Every time the EM wave encounters an interface, its energy will decrease because only a portion of it energy will be transmitted. Thus, the more reflectors and the stronger their reflection coefficients, the shallower the penetrating depth. Last and most importantly, the attenuation rate (controlled by conductivity) has the largest impact on the GPR penetration depth. It is suggested to avoid using GPR in high conductive materials like contaminated soils and clay-rich materials. In freshwater lakes,

the penetration depth is expected to 20 – 30 meters in the water and several meters into the sub-bottom depending on the material types (A. Annan, 1992; Brian J Moorman, 2002).

Overall, the resolution and penetrating depth are two very important factors that affect the performance of GPR system. There is a trade-off between these two factors since higher (or lower) frequency will result in shallower (or deeper) penetrating depth. Consequently, the choice of the GPR antennae depends on how deep the objective is and the desired resolution of the image.

Chapter 3 Methods

In this chapter, the data collecting, analyzing and modelling methods will be described in detail. There are three main stages for the work in this thesis project, including lake basin characterization, lake sediment analysis and lake sediment structure modelling. The outline of the methodology is described in Figure 3.1.

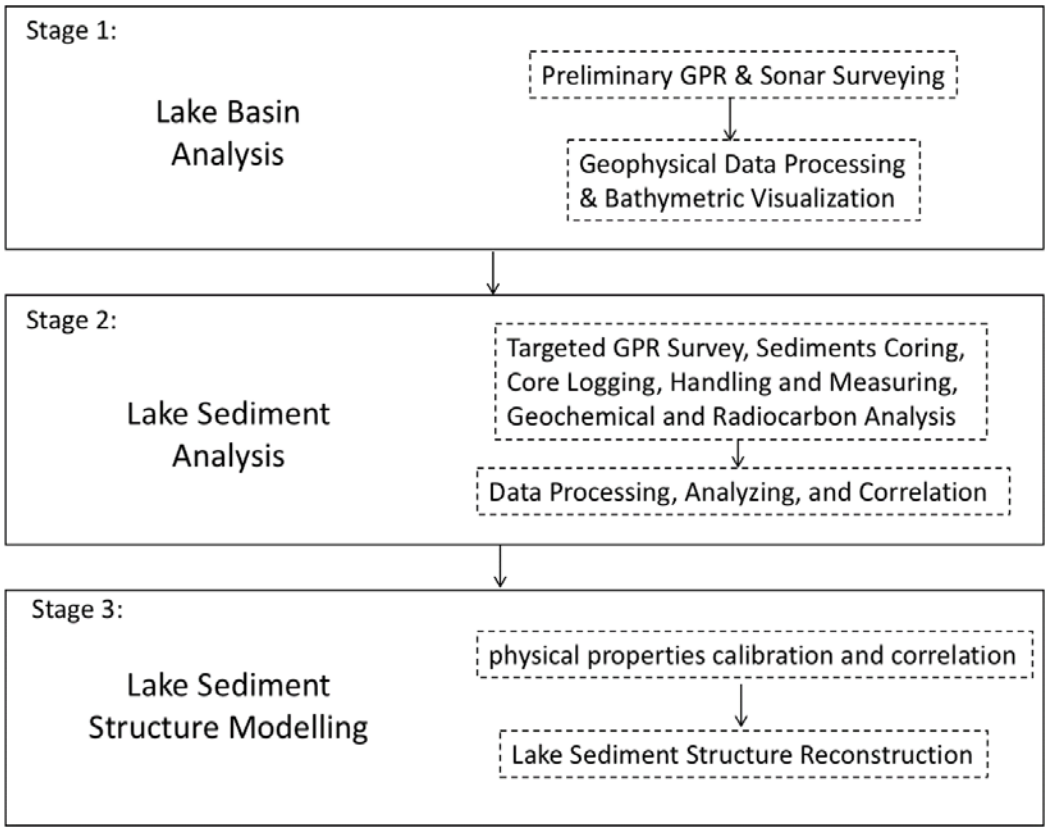

Figure 3.1 Methodology Outline

The work begins with using geophysical survey technique, such as GPR or Sonar, to conduct a full lake basin study of the lake bottom bathymetry and sediment distribution. Then, certain decisions, such as the GPR survey parameters and the coring locations and conditions, can be made for targeted GPR surveying and sediments coring. After the sediment cores are collected, they are logged, sub-sampled, and measured for a series of physical and geochemical properties. The collected data are processed, analyzed, and correlated. Finally, a 1-D GPR trace forward model is established.

3.1 Lake Basin Analysis

Lake basin analysis is the first stage of our study. In order to relate the physical

properties of the lake sediments to the GPR signals, the main goal of the basin analysis is to identify suitable lakes and lake bottom areas for linked GPR profiling and sediment coring. The secondary goal in this stage is to map the lake basin bathymetry as well as the shape of the underlying bedrock, so the total sediment volume can be calculated for estimating the carbon budget.

An ideal lake for our project has to meet several criteria. First of all, the penetration depth of the geophysical signals should be deep enough to reach the lake bottom and sub-bottom. Secondly, the lake should contain an adequate thickness of undisturbed sediments, and the water depth should be in the range of our current available rod-driven piston coring equipment, that is, less than 5 m. GPR and sonar are both non-destructive geophysical methods that can be used for the water bottom profiling without altering the internal structures in the lake sediments. Traditionally, sonar is used for lake bottom surveying, but its signal may not reach into the sediments and may not pick up the inner structures within the sediments. For these reasons, we primarily used GPR to conduct the preliminary geophysical survey due to its adequate penetrating depth and resolution for bottom and sub-bottom profiling in freshwater systems. Particularly, it is easy to use GPR in the winter of Newfoundland when the lake surface is frozen, which provides a very stable platform. However, the lake water conductivity must be low enough for GPR signal penetration. Thus, the targeted lake should be an inland fresh water lake. Typically, the larger the size of the lake, the deeper the water. Consequently, our target should be a small to medium inland freshwater lake, and Grassy Pond in the Big Easy Prospect is a candidate that meets all the requirements.

In this project, we used GPR as the primary geophysical method for the

preliminary surveying on Grassy Pond. This was preceded by a boat-mounted summer sonar survey on Tippings Pond, the initially chosen target for the study.

3.1.1 Geophysical Data Acquisition

The GPR system used in this project was “pulse EKKO PRO” by Sensors and Software Inc with 50 MHz and 100 MHz antennae. The basic components of this GPR system are shown in Figure 3.2. Since the 50 and 100 MHz antennae are too large to shield for unwanted externally generated EM signals, fiber optic cables are used to connect the control module to the transmitter and receiver for noise reduction. The GPR system was attached to a Real Time Kinematics (RTK) differential GPR system TopCon’s “Hiper-V”, which provided precise location information for the GPR survey lines. The RTK system has two components: base and rover (Figure 3.3). During the survey, the base station was set up at a high ground near the field site, while the rover was connected to the GPR system. The accuracy of the RTK system can be as good as 15 mm after static correction by the base station (TopCon, 2015).

The GPR survey used the common offset reflection survey method, which was applied on a grid that consists of several equal-spaced X and Y survey lines for the 3-D lake sediments and bedrock bathymetry mapping. The antennae were kept at a fixed spacing and orientated either parallel or perpendicular to the survey lines. During the survey, the GPR antennae were moved along the designed survey lines on the frozen lake surface. Depending on the snow coverage, the antennae were either mounted on a “smart cart” pushed by hand or dragged by an ATV (icy surface), or housed by custom-built wood and fiberglass skis pulled a snowmobile. Two people are required during the

survey, one driver and one operator (Figure 3.3 B). The GPR survey was carried out by attaching a handheld GPS when the RTK was not available (Figure 3.3C). The Garmin GPS has a lower precision (~1-2 m) but it was adequate for the surveys.

Figure 3.2 Basic components of pulseEKKO PRO (100 MHz) GPR system.

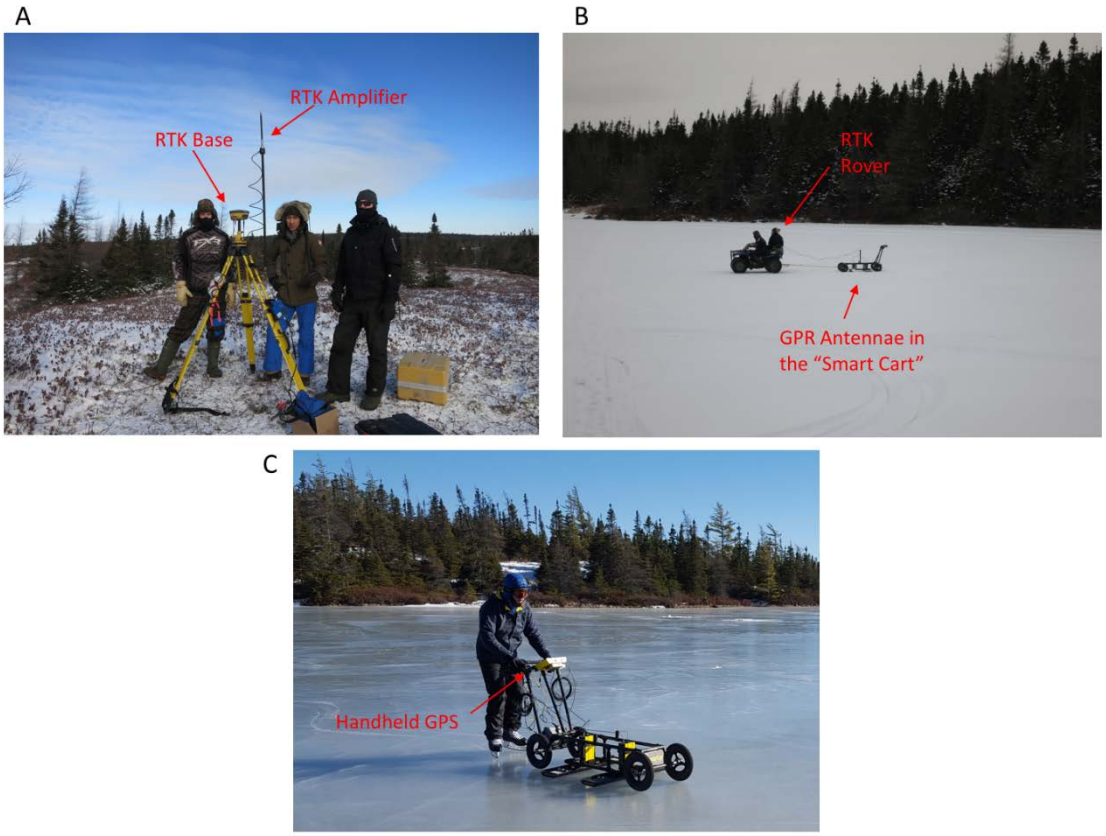

Figure 3.3 RTK and GPR system setup. A: RTK base station is placed at the nearby high ground; B: RTK rover is attached to the GPR system in a snowmobile driven setup during the survey; C: GPR SmartCart setup with a handheld GPS if RTK is not available.

We performed a sonar survey on Tippings Pond, near Corner Brook where the GPR signal was unable to penetrate the water more than 2-3 m due to the water's relatively high conductivity. The sonar device we used is a GPRMAP 527xs by GARMIN Inc. During the survey, the sonar device was attached on a customized wooden board that was mounted on the back of a boat (Figure 3.4). A handheld GPS was used for the location information. Although this sonar did not provide as much information as GPR for the lake sub-bottom, it was able to provide lake bathymetry in the case where GPR could not.

Figure 3.4 Sonar survey system setup on a boat.

3.1.2 GPR Data Processing

The geophysical data processing and visualization contains two stages of work: 1) basic and advanced GPR signal processing and interpretation; and 2) lake sediment and bedrock bathymetric visualization. The purpose of the data processing and visualization is also two-fold. The first goal is to identify suitable locations for the follow-up sediment coring, which requires basic GPR data processing and interpretation. The second one is to enhance the 2-D GPR cross-section profiles for correlating the reflections in the GPR sub-bottom profiles to the coring analysis data.

The work flow for the GPR data processing is guided by Annan (1999), and it is summarized in the highlighted zone in Figure 3.5, which lists the steps for GPR data processing flow and related common processing techniques that may apply to the GPR data set in this project. In the following sections, I will discuss the processing techniques

that are used in this project and how to approach the final products: enhanced 2-D GPR cross-section profiles and 3-D lake bathymetric maps.

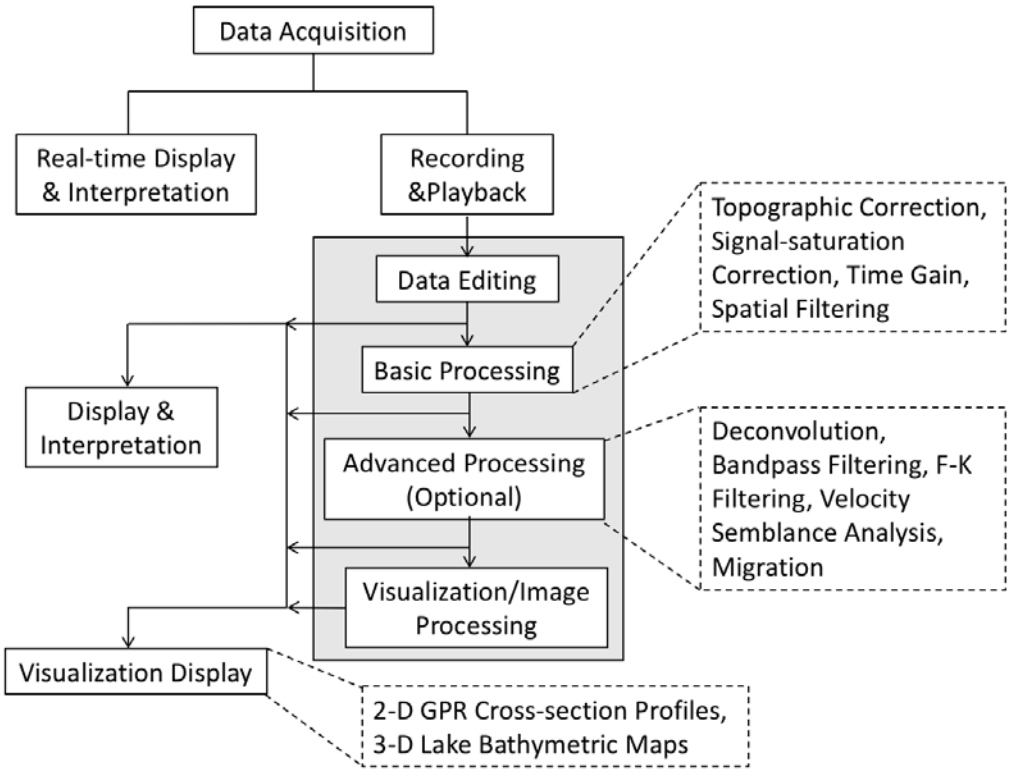

Figure 3.5 GPR data processing work flow.

The principle goal of processing GPR data (or any other types of geophysical data) is to overcome any limitations of the basic survey data and obtain realistic subsurface information for a confident interpretation (Neal, 2004). However, if the collected first-hand raw data is of poor quality (for example due to instrument noise, external electromagnetic interference, or insufficient sampling), post-acquisition processing – no matter how much – cannot rescue the data. Thus, the data acquisition is extremely important in the work flow. Fortunately, most modern GPR systems provide real-time data displays during the data acquisition stage, which allows users to adjust the

system parameters, such as the proper number of trace stacks for achieving an adequate signal-to-noise ratio or an appropriate time window for focusing on the most interested area in the subsurface. There are a lot of data processing techniques available, so it is easy to over-process the data set. The basic rules for data processing is to keep it simple and realistic. Thus, only necessary and limited processing steps for the interpretation will be applied to the data set in this project.

Compared to seismic data, GPR data usually requires much less processing to enable initial interpretations. The GPR device “pulse EKKO PRO” itself can perform some real-time basic processing, such as dewow, time gain and spatial filtering during the data acquisition, which enables in-site interpretation. The basic processing is usually enough for bathymetric and depth-to-bedrock mapping since these only require the TWT information for water-sediment and sediment-bedrock interfaces. However, in order to observe more details of the internal structure within the sediments, more advanced data processing techniques are often needed to enhance the GPR data quality further.

The first step of basic GPR data processing is usually temporal filtering to remove very low frequency components from the data, which is also referred as signal saturation correction (A. Annan, 1999). GPR signals often contain an inherent and nonlinear low frequency component due to the proximity of the transmitter and receiver and the electrical properties of the ground near the antennae (Brian James Moorman, 1990). The low frequency component of GPR signals does

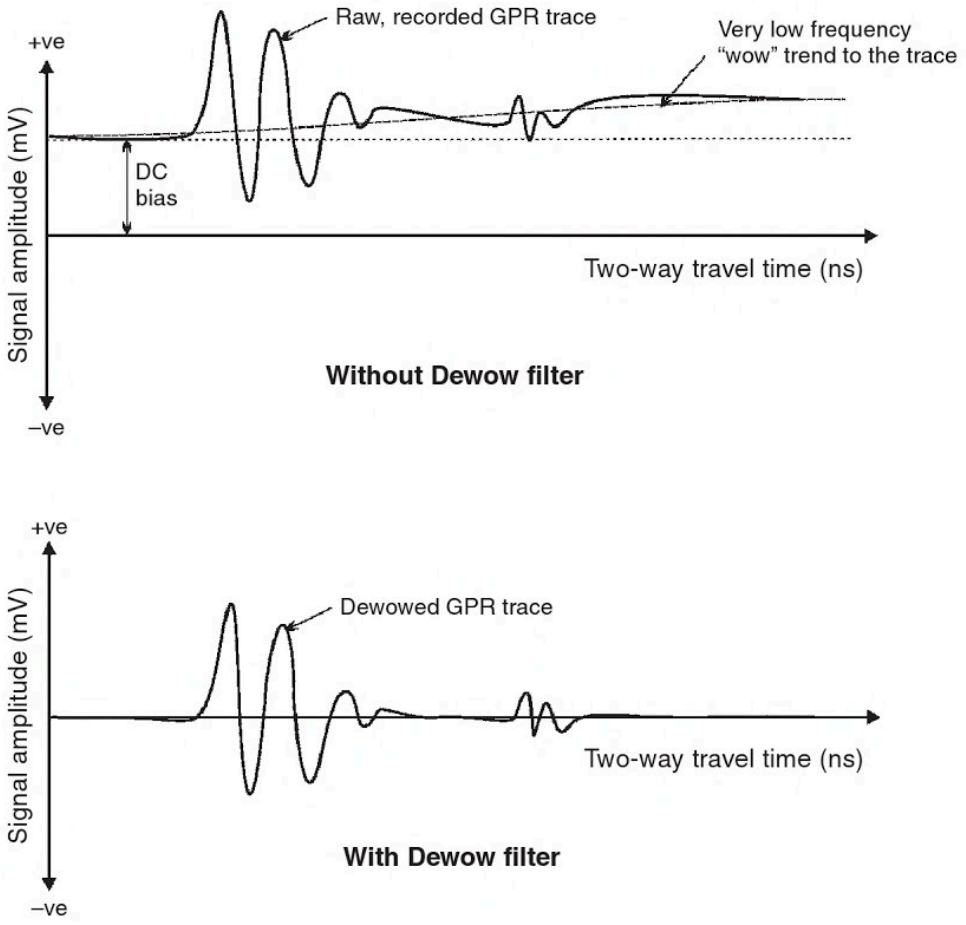

Figure 3.6 Dewow filter correction on a raw GPR trace (Cassidy & Jol, 2009)

not propagate but diffuses into the ground, which induces a slowly decaying "wow" (wave) on the high frequency components of the trace. Thus, the GPR receiver becomes signal saturated and unable to adjust fast enough to the large variations between vertical stacks (Fisher, Stewart, & Jol, 1996). The process to remove this unwanted low frequency component while preserving the high frequency component is is called "dewow". Dewow is a necessary step in the basic data processing because it resets the data to a mean zero level, so the positive-negative color filling can be used on the traces (Figure 3.6) (Cassidy & Jol, 2009). Signal saturation correction could be performed by a simple low-cut filter;

however, most modern GPR systems can automatically apply this correction to the traces with more optimized parameters and dewow also removes the possible DC bias.

The next step of basic data processing is to choose a time gain. A major issue with GPR data is that the attenuation of the radar signal in the ground can be highly variable, so it is essential to understand the need for time gain when processing GPR data (A. Annan, 1992). The amplitudes of later arrived signals of a trace are generally lower than the earlier arrived ones due to conductivity losses in the medium. Therefore, time gain is usually necessary in the basic data processing flow for increasing the visibility of the weak late-arrived signals in the data. Since time gain is a non-linear process, it can be applied before or after temporal and spatial filtering (Sensors&Software, 1999). According to Jol and Bristow (2003), there are two popular time gain functions: automatic gain control (AGC) and spherical and exponential gain compensation (SEC) that can be applied to the GPR data to deal with the rapid signal fall-off. The mechanism of AGC is to equalize the amplitudes all the way down each trace, while the SEC applies a linearly increasing time gain combined with an exponential increase. Since the spherical EM waves attenuate exponentially when spreading into ground, a SEC is usually better than an AGC for GPR data. Fisher et al. (1996) provided the formula for SEC gain:

$$b_i = i \times a_i \times e^{in\frac{dt}{10000}} \tag{3.1}$$

where a_i is the ith sample of the signal trace, b_i is the ith sample of the gain recovered trace, n is the gain constant and dt is the sample rate (s).

A possible next stage of GPR basic processing is spatial filtering. Spatial filters work across the traces in distance along the survey line instead of in time down a given

trace like temporal filters such as dewow (Cassidy & Jol, 2009). The most important goal of running spatial filter is to remove ringing (horizontal bands) in the data set, which result from high frequency random noises. In addition, spatial filters can also remove direct air waves and ground waves at the top of GPR profiles. There are many types of spatial filters, but the most frequently-used one is background average subtraction that subtract the average trace of the entire GPR line from every trace in the line. The average trace is calculated by adding all the traces in the line together and divided by the total number of traces (Sensors&Software, 2005). Figure 3.7 shows an example of the amplitude spectrum analysis of a data set collected by 100 MHz antennae before and after running background average subtraction.

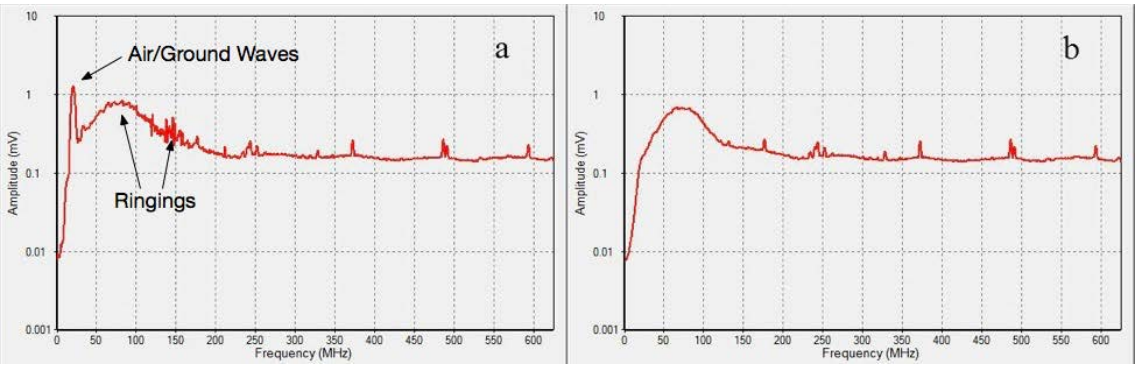

Figure 3.7 An example of the amplitude spectrum analysis of a 100 MHz GPR survey line from Grassy Pond. a: before background average subtraction; b: after background average subtraction.

Other basic processing techniques, such as time-zero correction and topographic correction, are occasionally applied to the data set depending on the nature of the GPR instrument and field site. Time-zero correction is used to correct the misalignment of the first break (air/ground wave) caused by thermal drift, electronic instability, cable length differences and variations, which could result in imprecise ground (time-zero) positions in

the GPR profile. Fortunately, most modern GPR software packages can perform automatic realignment by physically moving each individual trace up and down (Neal, 2004). Topographic correction could be essential if the elevation variation is noticeable along the survey line, which could cause significant distortion of the subsurface image (Fisher et al., 1996). It can be corrected by moving each trace up and down based on the GPS information and the depth profile of the uppermost part of GPR profile. For surveys on the lake ice surface, topographic correction is often unnecessary because the elevation variation is minimum.

The data sets should remain reasonably intact after basic data processing by applying simple and non-linear processing operators, so the subsurface information will not be distorted. In most cases, basic data processing is usually sufficient to enable GPR reflection data interpretation. Advanced data processing will only be considered if there is a need because the data may be significantly altered from the raw data set.

Most advanced data processing techniques, such as velocity semblance analysis, normal moveout correction, depth conversion, are more frequently used in CMP survey type data rather than reflection type data, which is the type of the data collected in this project. However, GPR reflection data can still benefit from applying some advanced data processing techniques, such as spiking deconvolution, to increase the resolution and reduce the reflection distortion. Since the subsurface acts as a filter during the reflection events, the original GPR data *S(t)* is a result of the convolution between the source wavelets and the reflection coefficient series, that is:

$$S(t) = W(t) * R(t) \tag{3.2}$$

where W(t) is the source wavelets and R(t) is the reflection coefficient series. Spiking

deconvolution provides a means to remove the source wavelet from the GPR data, so the reflection coefficient series can be reconstructed. However, spiking deconvolution can only be successful if the data is stationary and in minimum phase (Cassidy & Jol, 2009). Thus, additional spectral analysis has to be performed to determine if the data meets the requirement for spiking deconvolution. Spiking deconvolution can also introduce some high frequency artifacts, so bandpass filters are often combined with this operator. There is also a more advanced data processing technique, migration, which is occasionally applied to GPR data to solve certain problems with the data set. Migration is used to remove diffractions, distortions, dip displacements and out-of-line reflections that result from complex subsurface geometries (Neal, 2004). However, this technique requires very precise velocity profiles from CMP survey data, and it is generally very time-consuming to apply on all data sets.

In this project, “EKKO Project R3 V2” by Sensors & Software Inc. was used for the basic data processing. However, this software package does not have the functions to perform more advanced data processing. In order to perform advanced data processing, the basic processed GPR data have to be imported into a seismic data processing software package.

3.1.3 GPR Data Interpretation and Visualization

In order to create a bathymetric map and a depth-to-bedrock map of the lake basin, depth information for interfaces of water-sediment and sediment-bedrock must be known; these can usually be extracted from GPR reflection profiles. Since the vertical component of GPR profiles is measured in two-way-traveltime (TWT), the velocities of

the EM wave must be known to convert the time information to depth information. The EM wave velocities for common geological materials are shown in Table 3.1. However, these velocity values are only precise for simple materials like ice and water. Due to the complexity of the lake sediments, the velocity cannot simply be taken from the literature values but has to be evaluated in situ. The traditional way to obtain radar velocities is to use common midpoint (CMP) gathering (see Figure 2.2). However, this method is time consuming, and it is also very hard to track individual reflections underneath the water-sediment interface. Small boulders are often buried at the bottom of lake sediments. When this is the case, instead of using CMP gathering, the average radar velocity (V) above the bedrock can be estimated by tracing diffractions caused by these point reflectors located on the sediment-bedrock interface.

Table 3.1 EM wave properties of common geological materials. Modified from Moorman, 2002; Neal, 2004. Original source: Davis & Annan, 1989; Theimer et al., 1994; van Overmeeren, 1997; van Heteren et al., 1998

Material	**Relative dielectric permittivity**	**EM wave Velocity**	**DC Electrical conductivity**	**Attenuation**
	ε_r	v (m/ns)	σ_{DC} (mS/m)	α (dB/m)
air	1	0.3	0	0
distilled water	80	0.033	0.01	0.002
fresh water	80	0.033	0.5	0.1
sea water	80	0.01	30000	1000
pure ice	3 - 4	0.16	0.01	0.01
fresh water unsaturated sand	2.55 - 7.5	0.1 - 0.2	0.01	0.01 - 0.14

fresh water saturated sand	20 - 31.5	0.05 - 0.08	0.1 - 1.0	0.03 - 0.5
fresh water unsaturated silt	2.5 - 5	0.09 - 0.12	1 - 100	1 - 300
fresh water saturated silt	22 - 30	0.05 - 0.07	100	1 - 300
silts (various)	5 - 30	0.07	1 - 100	1 - 100
fresh water unsaturated clay	2.5 - 5	0.09 - 0.12	2 - 20	0.28 - 300
fresh water saturated clay	15 - 40	0.05 - 0.07	20 - 1000	0.28 - 300
clays (various)	5 - 40	0.06	2 - 1000	1 - 300
limestone	4 - 8	0.12	0.5 - 2	0.4 - 1
shales	5 - 15	0.09	1 - 100	1 - 100
granite	4 - 6	0.13	0.01 - 1	0.01 - 1

Figure 3.8 shows the basic mechanism of the GPR diffractions. Assuming the separation between the transmitter (R) and receiver (T) antennae is negligible, *x* is the horizontal displacement between the R-T location and the point reflector, *h* is the depth of the point reflector from the surface, then the length *l* of the diffraction ray path from T-R location to the point reflector is given by:

$$l^2 = x^2 + h^2 \tag{3.3}$$

Since the TWT for the diffraction is $t_x = 2l/V$, it can be expressed as:

$$t_x^2 = \frac{4h^2}{V^2} + \frac{4x^2}{V^2} = t_0^2 + \frac{4x^2}{V^2} \tag{3.4}$$

where t_0 is the normal incident TWT of the point reflector, and $t_0 = 2h/V$. Thus, the diffraction due to a small, buried object appears as a hyperbola on the GPR profile, and

the apex of the hyperbola occurs when the T-R location is directly over the object. By tracing the shape of the hyperbola, the average radar velocity above the point reflector can be estimated. In fact, most modern GPR processing software has a function to estimate the average radar velocity based on these hyperbolas.

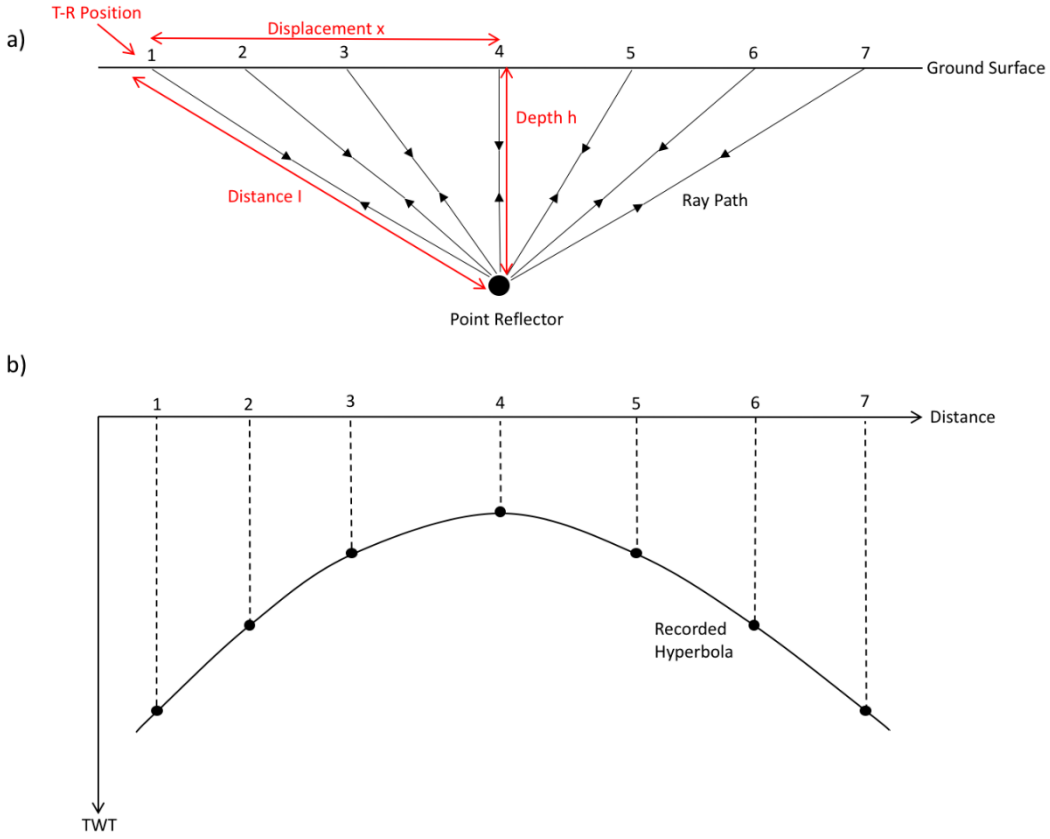

Figure 3.8 The basic mechanism of GPR diffractions. Modified from Kearey &Brooks, 1991 and Neal, 2004.

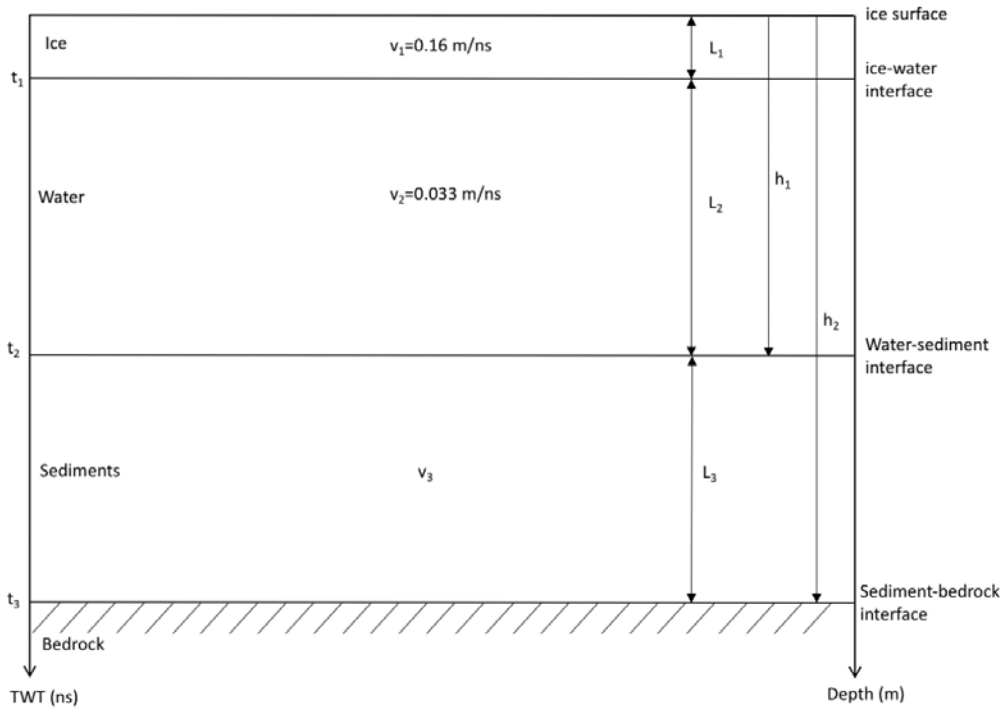

Figure 3.9 A synthetic three-layer conceptual model for calculating the sediment and bedrock depth for a typical freshwater lake during the winter.

A synthetic (and somewhat simplified) three-layer conceptual model is developed to calculate the sediment and bedrock depth for a typical freshwater lake during the winter (Figure 3.9). The whole system is assumed to be overlying the bedrock. From the top to the bottom, these layers are ice, water and sediments. Although the ice layer has little influence on the character of the GPR profile due to the very fast radar propagation speed in it, it is still non-negligible for the depth calculation. First of all, the depth to the top of the sediments (h_1) can be calculated by using following formula:

$$h_1 = L_1 + L_2 = L_1 + v_2 \cdot \left(\frac{t_2}{2} - \frac{L_1}{v_1}\right) \tag{3.5}$$

where L_1 and L_2 are the thickness of the ice and water layer, respectively; v_1 and v_2 are the

radar velocity in the ice and water layer, respectively; t_2 is the TWT for the water-sediment interface in the GPR profile. The ice thickness (L_1) was obtained from ice augering and is relatively constant in the model The radar velocities in the ice (v_1) and water (v_2) are fixed as 0.16 nm/s and 0.033 m/ns (see Table 2.1). The depth of bedrock (h_2) can be calculated by using the average radar velocity derived from the hyperbolas on the sediment-bedrock interface. The formula for h_2 is given by:

$$h_2 = v_{ave} \cdot \frac{t_3}{2} \tag{3.6}$$

where v_{ave} is the average radar velocity above the bedrock, and t_3 is the TWT at the sediment-bedrock interface in the GPR profile. Thus, the thickness of the sediment layer L_3 can be calculated by:

$$L_3 = h_2 - h_1 \tag{3.7}$$

and the average radar velocity in the sediments (v_3) can be calculated as:

$$v_3 = \frac{L_3}{0.5(t_3 - t_2)} \tag{3.8}$$

. In theory, the sediment and bedrock depth and even the average radar velocity in the sediments can be mathematically calculated in this conceptual model. However, the calculated results are only accurate directly above the diffraction hyperbolas caused by boulders sitting on the sediment-bedrock interface. In reality, there are only limited numbers of diffraction hyperbolas occurring in one GPR profile. Thus, it is required to analyze as many as possible diffraction hyperbolas from all the GPR profiles on the lake for estimating the average radar velocity above the bedrock to make this conceptual model representative for the real situation. Most importantly, the calculated results need

to be calibrated with the measured depths from the coring procedure and literature values of velocity to ensure reliability.

The basic software for creating maps of the sediment and bedrock depths and sediment thickness are GPR software package “EKKO Project R3 V2” by Sensors&Software Inc. and “MatLab” by MathWorks Inc. The procedure is summarized in the following steps:

1) In the GPR software package, mark the water-sediment and sediment-bedrock interfaces on the processed 2-D GPR profiles and export these marked points as TWTs;

2) Identify hyperbolas on the sediment-bedrock interface and carry out hyperbolic analysis, and time-depth conversion by using the conceptual model above;

3) Import the converted depth information of these two interfaces into “MatLab” and create 3-D bathymetric and depth-to-bedrock maps;

4) Create the sediment thickness distribution map in “MatLab” by calculating the depth information of the difference of the two interfaces.

The area of the pond and the volume of the water body and sediment body can also be calculated from the data in “MatLab”.

3.2 Lake Sediment Analysis

Lake sediment analysis is the second component of our project. The main goal of the lake sediments analysis is to characterize the stratigraphy that is observed in the GPR profiles by analyzing the physical properties in the actual sediment itself. The secondary goal is to collect and analyze the sediment geochemical data to see if there are any correlations to the physical property variations so that it could be link to any

paleoclimatic events. Work in this stage involves sediment core capturing, a series of data acquisition from the sediments in the cores, and data processing, analysis and correlation.

Lake sediment coring is the first and also one of the most important components in this study because the success of the subsequent, time-consuming analyses depends on the quality of the obtained sediment core samples. The aim of an effective sediment coring is to recovery undisturbed and continuous sediments samples. In this section, I will explain how the coring locations are chosen and the coring equipment and method we used.

The lake bathymetry information, including water depth, sediment thickness and distribution, is critical before making coring decisions because different water bodies require different coring equipment and methods. For example, drilling, instead of coring, equipment is requires for deep lakes (typically more than 30 or 50m) (Leroy & Colman, 2002) or long sediment core sections (usually longer than 15-20m) (Glew, Smol, & Last, 2002). A preliminary geophysical survey and subsequent lake basin analysis is required to determine these bathymetric factors (see last section). The sediment distribution map created in the basin analysis stage is used to locate the optimal coring area. The ideal coring site is where the sediments are thick and horizontally stratified, usually the central part of the lake basin. The edge of the sedimentary basin is often avoided for coring because slopes can produce complex stratigraphic conditions and potentially discontinuities. In this study, using data from GPR profiles, the coring locations were carefully chosen where thick sediments contain significant, flat laminations. In addition, areas where sediments were relatively thin (< 2m) were chosen in order to obtain full length of sediments from the water-sediment interface to the bedrock for average radar

velocity benchmarking. It was also of interest to compare sediment properties between deep and shallow accumulation areas.

3.2.1 Sediment Coring

Many types of coring equipment have been developed today, only some of which can be used for lake sediment coring. Lake sediments, especially near the water-sediment interface, usually contain more liquid (> 90% water content) than solid; hence, it is necessary to use an enclosed coring tube with a strong vacuum seal at the top. In addition, the coring system should not alter the inner structure of lake sediments. Core catcher devices sometimes attached to the bottom of marine coring systems can disrupt sediment at the perimeter of the corer, and for very soft sediments the disruption extends to the centre of the corer, so the low end of the coring tube must be open during the coring process. The rod-driven piston corer is the only one among three coring systems tested, which was successful in collecting the very water-rich, organic soft sediments in Grassy Pond.

The rod-driven piston coring system consists of a 10 foot (3.05 m) plastic coring tube, a few PVC pipes attached to the coring tube by duct tape, a rubber piston with a central screw that can be tightened or loosened to adjust its diameter, a few caps for sealing the tube ends, a tripod, and a rope that connects the piston to the tripod. Additional equipment used for assisting coring was a GPS for locating the coring location, an ice auger for drilling a hole on the frozen lake ice surface, a circular metal plate attached by a measuring tape for the water depth and ice thickness measurements, and a core cutter that was used to cut the long core into several pieces in the field for

transportation. Figure 3.10 shows the piston coring equipment that we used for collecting lake sediments samples.

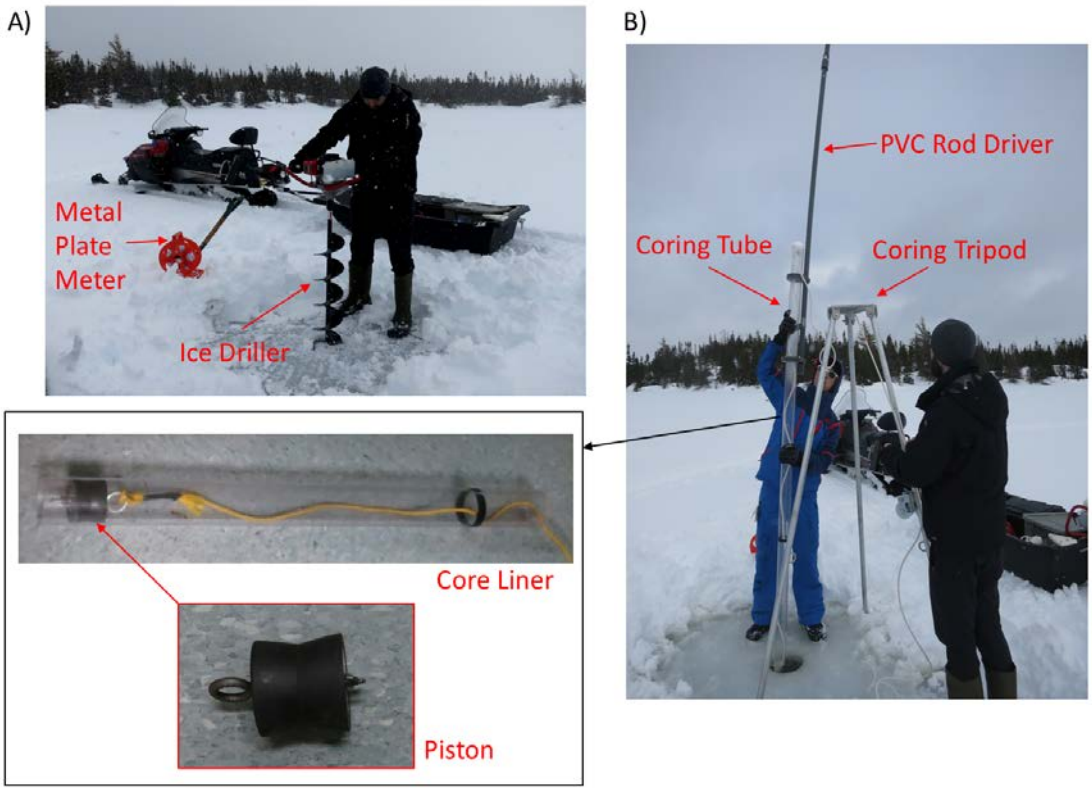

Figure 3.10 A rod-driven piston coring system. A: Ice auger and water depth measuring equipment; B: Coring equipment.

The basic principle for this rod-driven piston coring system is using the piston to create a vacuum that keeps the sediments in the tube during the coring process. Figure 3.11 illustrates the coring process. Before coring, the ice auger is used to open a hole on the ice surface, and then the metal plate attached to the bottom of a measuring tape is lowered through the hole until it comes to rest on the water-sediment interface. The water depth is read off the measuring tape. The water depth is marked on the coring device. The coring procedure is summarized in the following steps:

1) When starting coring, the piston is inserted at the low end of the coring tube and the screw on the piston is used to tighten it for a snug fit. In order to balance the pressure above and below the piston, some water may be poured into the coring tube to maintain the piston at the fixed position at the end of the coring tube while moving down.

2) When the low end of the coring tube reaches to within a few centimetres of the water-sediment interface (the marker reaches the ice surface), the rope attached to the piston is fixed onto the tripod.

3&4) The coring tube is pushed down until the corer reaches the sediment-bedrock interface – or its maximum depth – while the piston stays stationary at the water-sediment interface.

5&6) The rope is released, and the coring tube slowly pulled up while the piston stays at its last position near the top of the coring tube.

Because the coring tubes we used are 10 feet long, where the sediments are thicker than this length, additional coring is required. In this process, the second coring tube with the piston at its lower end, is pushed down into the sediment until it reaches the depth limit of the last core. Care must be taken to line up the corer with the path of the first corer, and the fit of the piston must be sufficiently tight that it is not pushed upward as the core is pushed into the mud. Once in position, steps 3) to 6) are followed. When the coring process is finished, the whole core was immediately cut into shorter pieces (about 1.5m) and sealed by custom cap holders wrapped by electrical tape. These core segments were placed vertically in a core holder and transported to the core storage room (4 ^{0}C) in the Earth Science Department of Memorial University waiting for the core logging.

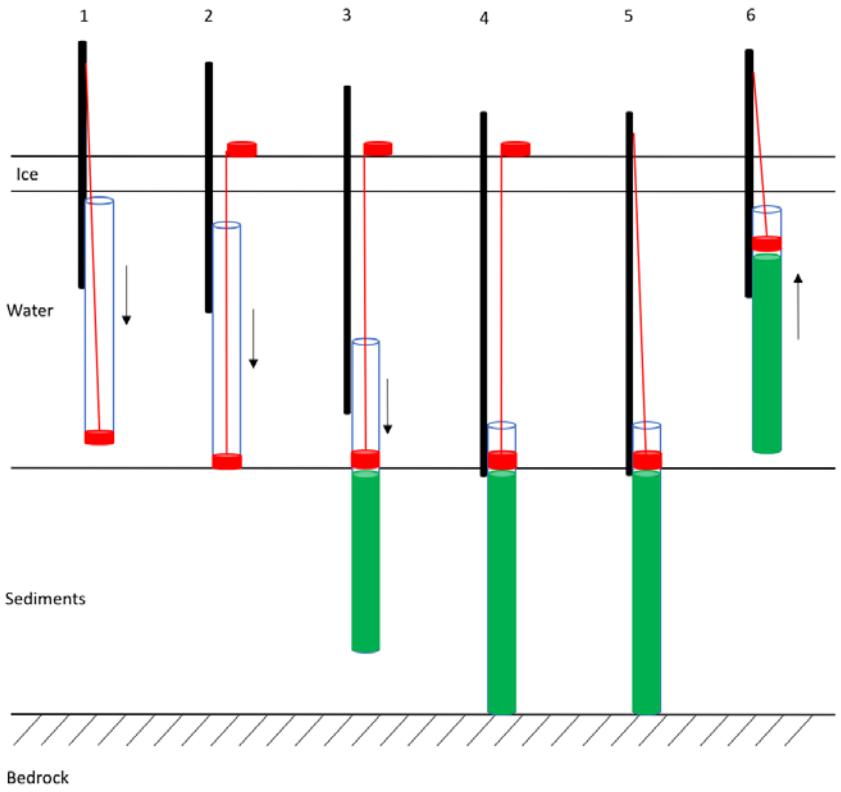

Figure 3.11 The rod-driven piston coring processes.

3.2.2 Sediment Core Logging

Lake sediment physical properties, such as water content, bulk density, grain size, magnetic susceptibility and acoustic properties, can significantly reflect down-core variability that may be associated with climatic variabilities or watershed-scale disturbances as well as anthropogenic influences (Zolitschka et al., 2002). The traditional way to measure these physical properties is to use a spatial subsampler on discrete core samples with a resolution of several millimeters. However, this destructive technique is time-consuming and is often restricted on only one property from each site. Recently, new core logging devices have been developed to meet the demand of rapid, non-destructive, continuous and high-resolution data acquisition. The multi-sensor core logger

(MSCL) is one of these core logging devices that was originally developed for marine sediment cores. In this project, we used a GeoTek MSCL system to scan the sediment cores we obtained in the field to determine density and P-wave velocity without opening the sediment cores. The MSCL system is located in the Earth Science Department of Memorial University.

The MSCL we used for sediment core logging is a computer-controlled and track motor driven automatic logging system (Figure 3.12). The logging system consists a series of stationary sensors that can scan the core in equal steps when it passes by. Users can define the spatial measuring rate (resolution) from 1mm to a larger number. Typically scans are taken at a resolution of 1 or 2 cm. The system can accept multiply core sections with a maximum length of 1.5m for each individual section, and log at a rate of 3 or 4 m/hr at the sampling interval of 1 cm. The sensors of our MSCL system can be used to measure gamma density, P-wave velocity, magnetic susceptibility, electrical resistivity, and core thickness. It is also possible (however, not available to us) to gather natural gamma data, XRF data, digital images, and color spectrophotometry by adding additional sensors to the system. The most important physical properties we expect from the MSCL are gamma density and P-wave velocity because these two properties are highly associated with water content, which can reflect the dielectric permittivity level. Even though electrical resistivity is also a critical electrical property that can be correlated to GPR profiles, the measurement for this property of lake sediments is not possible using this logging system because the MSCL was originally designed for marine sediments, whose electrical resistivity is much lower than lake sediments. Magnetic susceptibility is another useful proxy data that indicates the content of iron-bearing minerogenic

contribution to the sediments corresponding to weathering effect.

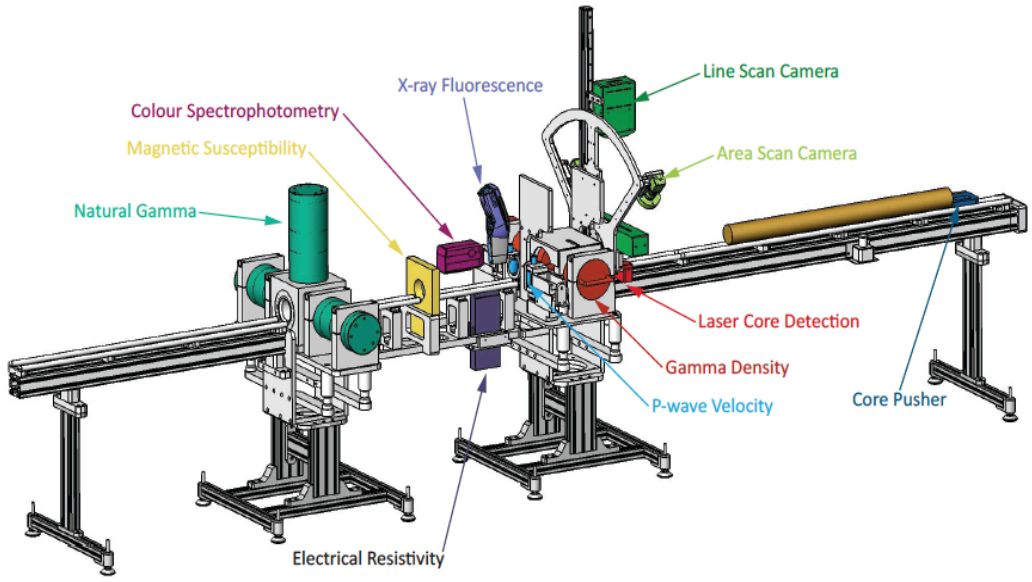

Figure 3.12 A 3D view of a standard Multi-Sensor Core Logger (MSCL) by GEOTEK Inc. The Memorial system lacks the Natural Gamma, X-ray Fluorescence and Area Scan Camera shown here.

Gamma density is one of the basic physical parameters that MSCL provides to measure the bulk density of wet sediment cores. The principle of this method is to determine the gamma ray attenuation when they pass through the sediment core. The gamma radiation source is ^{137}Cs stored in a 150 mm diameter lead-filled and 3 mm wall stainless steel container. The half-life of ^{137}Cs is 30.2 years, and the initial energy that the gamma rays emit is 0.662 MeV. The gamma ray attenuation at this energy level is caused by Compton scattering: the incident photons are scattered by the electrons in the core with a partial energy loss (Davidson, Biggar, & Nielsen, 1963). Thus, the number of electrons in the gamma ray beam path can be measured by counting the transmitted gamma photons that pass through the core, and the bulk density can be calculated if the core thickness is

known (GEOTEK, 2008). The MSCL measures the initial gamma ray intensity (I_0) and the final gamma ray intensity (I) after it pass through the sediment core, and the bulk density (g/cc) can be calculated by:

$$\rho_B = \frac{1}{-\mu d} ln\left(\frac{I}{I_0}\right) \tag{3.9}$$

where μ is the specific Compton mass attenuation coefficient (cm^2/g), and d is the thickness of the sediment core (cm). The core thickness (d) and gamma ray intensity (I_0) and (I) can be directed measured by MSCL, while the Compton attenuation coefficient is a material constant that equals to 0.0774 cm^2/g for most minerals in lake sediments (Ellis & Singer, 2007). Consequently, gamma density (wet bulk density) measurement is essential in core logging. Zolitschka et al. (2002) well summarized the importance of this parameter in the core logging applications: 1) as a guideline for core sampling; 2) to characterise the core lithology; 2) to derive a porosity/water content profile; 4) to correlate other sediment physical properties; 5) and as one parameter to calculate the accumulation rate.

P-wave velocity is another important physical parameter of sediments, and it is the second parameter that MSCL measures after gamma density. The variation of P-wave velocity is caused by the changes in elastic properties of the material through the profile. The measurement of P-wave velocities is important to understand the physical nature of seismic profiles with different reflectors. Even though the basic mechanism of GPR reflections is different from that of seismic reflections, the P-wave velocity can still be an important parameter for the correlation between these two methods. The P-wave velocity is measured by MSCL using a pair of compressional wave transducers (pulse generator

and receiver) in contact with and on opposite sides of the core, with a transmitted pulse frequency of 500 kHz and a repetition rate of 1 kHz. After calibration, the logging system can measure the P-wave travel time across the sediment-filled core tube, and the P-wave velocity (m/s) is calculated as:

$$V_p = \frac{d_R - 2d_L}{t_R - t_L} * 10^3 \tag{3.10}$$

where t_R is the recorded pulse travel time (μs), t_L is the pulse delay time (μs) related to the travel time through transducer heads and coring tube walls, d_R is the outer diameter of the coring tube (mm) and d_L is the coring tube thickness (mm). Temperature affects the P-wave velocity measurements, so the sediment cores have to be placed in the laboratory overnight before the measurement to achieve temperature equilibration (Weber et al., 1997), and the temperature is monitored during measurement.

An important applications of MSCL P-wave velocity measurements is to improve the understanding of seismic profiles. The acoustic impedance Z (10^3 x kg/m^{2}s) can be calculated by multiply p-wave velocity (m/s) and bulk density (g/cc):

$$Z = V_p \cdot \rho_B \tag{3.11}$$

The reflection coefficients R_i between two boundaries can be calculated by:

$$R_i = \frac{Z_i - Z_{i-1}}{Z_i + Z_{i-1}} \tag{3.12}$$

and TWT can be converted from core depth and P-wave velocity V by:

$$TWT = \sum_{j=1}^{i-1} 2 \cdot \frac{\Delta z_j}{V_j} \tag{3.13}$$

where Δz_j is the layer thickness. A synthetic seismogram can be produced by convolving

a selected acoustic wavelet and a series of reflection coefficients that are placed at time intervals corresponding to interface depths. The production of a synthetic seismogram is analogous to the synthetic radargram study we carried out (Section 3.3).

3.2.3 Core Subsampling and Properties Measuring

The next step of the sediment core processing after logging was to subsample the core in even intervals and prepare the core subsamples for geochemical analysis. Additional physical properties such as water content, DC resistivity and IP effect were tested during this process. This whole process is time-consuming depending on the numbers of cores and the sampling resolution. Thus, the sampling rate has to be carefully chosen to fit within the processing time budget while maintaining a reasonable resolution. The water content was measured during the subsampling, and this parameter correlated with the core logging data. Although the resistivity can be measured by MSCL, the measurement range is limited between 0.1 and 10 ohm.m because the MSCL is originally designed for marine cores that have a much lower resistivity than our freshwater sediments cores do. Thus, we used a sample core I.P. tester (SCIP) by Instrumentation GDD Inc. to measure the resistivity and chargeability of our core samples.

Based on the resolution of the 100 MHz GPR signals (see Table 2.2), the core sampling resolution is set to 10 cm for all our sediment cores. The core cutting system is the same one we used in the field, and we set it up in the laboratory. Additional equipment consisted of an analytic balance, a set of custom-designed core electrodes, the SCIP system, two ovens, and a mortar and pestle. Each electrode consists of a solid plastic (delrin) cylinders, with a circular copper plate on the inner flat surface. The

copper plates were connected to imbedded banana plug connectors, which were connected to the SCIP by wires. The cut core sample was placed between the electrodes. The top electrode has a handle and a diameter that allows it to fit snugly inside the core tube. Figure 3.13 shows the core sampling and testing process. The whole process is straightforward but required careful operation to avoid leaking of sediments from the bottom of the cut core tube since the sediments were very slippery.

First, the sediment core tube was marked at 10 cm intervals with the cutting positions. After each cut, a thin sheet of hard plastic was inserted into the cut to hold the sediments in place, the core section was placed on the bottom electrode, the plastic removed, the top electrode put in place, and resistivity and chargeability measurements are taken. When the SCIP measurements were completed, using the top electrode, the sediments were pushed out of the core tube section onto a plastic tray covered by plastic wrap. The sediment samples were weighted and transferred to glass containers. All the glass containers with sediments were labelled and put into an oven at 70 ^{0}C for drying. The dried samples were weighed again to calculate the water loss. All subsidiary material that was muddied, like plastic wrap, core tube sections etc, were weighed wet, dry and clean to account for any mud components not added to the glass containers. Finally, about half of the complete dried sediment samples were powdered using a mortar and pestle and put into smaller labelled plastic containers for subsequent geochemical, isotopic and dating analysis.

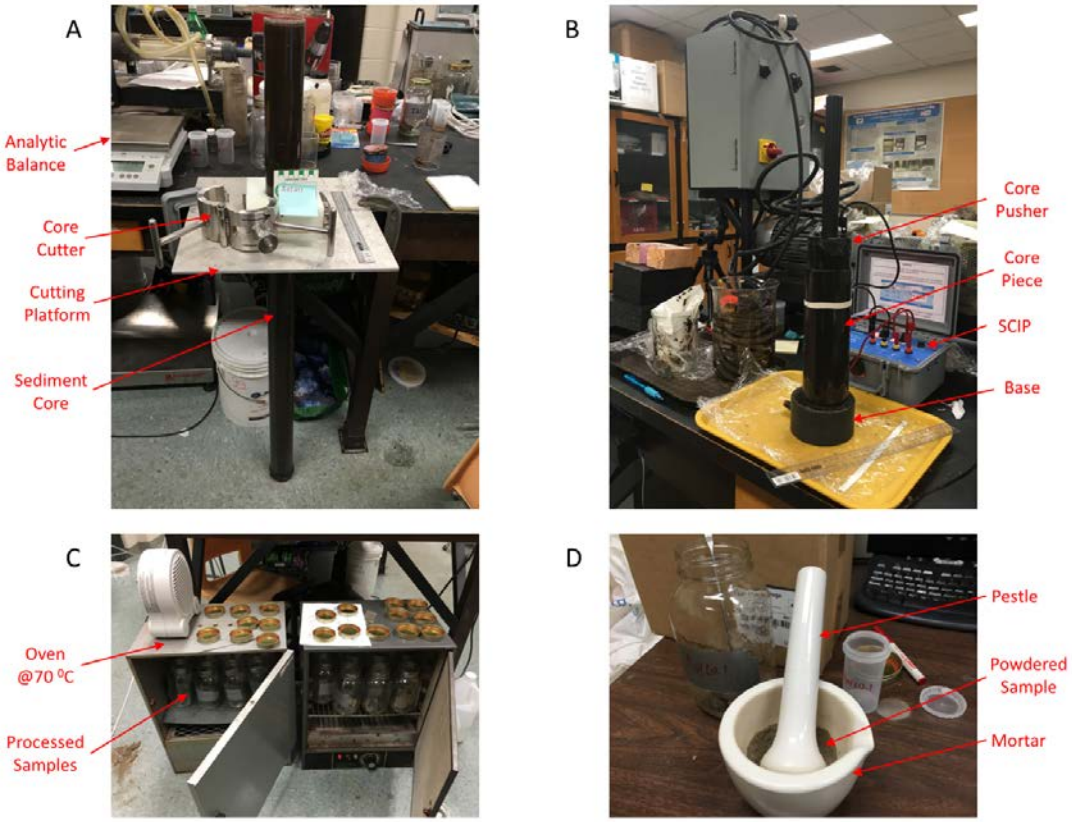

Figure 3.13 Core subsampling, processing and testing. A: Core cutting; B: SCIP testing; C: Sample drying; D: Sample Powdering

3.2.4 Geochemical Analysis

Geochemical analysis of sediments has played a significant role in palaeolimnology research. The geochemical analysis can be divided into inorganic geochemistry analysis and organic matter analysis. The results of both these two types of analysis can provide proxies for past climate changes. The most important application of inorganic geochemical analysis of sediments is to reconstruct paleoenvironmental changes. Even though this thesis project is mainly focussed on the geophysical properties of the sediments, the inorganic geochemical analysis can help correlate the physical properties variations within the sediments to paleoenvironmental events. It is also

possible to correlate geochemical to geophysical variations if there is a link between these two different types of data. Organic matter is another key component of lake sediments. The organic matter within lake sediments can indicate the past climate and surrounding environment conditions. The geochemical analysis methods involved in this thesis project consist of major and trace elements analysis by Inductively Coupled Plasma Optical Emission Spectroscopy (ICP-AES), organic matter analysis by Loss on Ignition (LOI), and C&N analysis by Isotope Ratio Mass Spectrometers (IRMS).

ICP-OES is one of the most versatile methods of inorganic analysis, and it has been widely used over the past few decades. This method provides a rapid, stable, highly sensitive analysis of a wide range of elements. ICP-OES analysis is available in the Department of Nature Resources (DNR) of Newfoundland. ICP-OES method is based on the measurement of atom emission rays. When plasma energy is applied to a sample, the component atoms are excited. When the excited atoms return to a lower energy state, emission rays characteristic of each element are released and measured. The type of element is determined by the ray wavelength and the elemental concentration is measured by the ray intensity. More detailed background and principle of ICP-OES can be found in numerous textbooks and articles, so this section will be focusing on the sample preparation and processing. LOI ("loss on ignition") is a traditional method that can be used to determine the organic matter content in most soil and sediment samples (Dean Jr, 1974).

Since ICP-OES only accepts solution samples, our sediment powders were digested by multiple acids before the measurement. First, 1 g of sediment was weighed in a 25 mL porcelain crucible and pre-ashed by placing it in a 550 ^{0}C muffle furnace for 4

hours. When the crucible cooled, the ash was transferred to a 125 ml Teflon beaker, and re-weighed for the calculation of LOI. Then, 5 mL of concentrated hydrochloric acid (HCL), 5 mL of concentrated nitric acid (HNO_3), 2.5 mL of concentrated perchloric acid ($HCLO_4$) and 15 mL of concentrated hydrofluoric acid (HF) were added to the beaker. The samples were placed on a hotplate at 200 ^{0}C and evaporated to dryness, and then the beakers were half filled with 10% HF and returned to the hot plate at 100 ^{0}C. When the residue was completely dissolved, the samples were removed, cooled and transferred to 20 mL storage tubes. Then, 1 mL of 50 g/L boric acid (H_3BO_3) was added to each sample to complex any residual HF. Finally, the samples were made to volume and analyzed for up to 31 elements by ICP-OES. Table 3.2 shows the detectable elements and their wavelengths and detection limits.

Table 3.2 The elements and their wavelength and detection limits by ICP-OES.

Element	Wavelength (nm)	Unit	Detection Limit
Al	257.510	%	0.01
As	189.042	ppm	2
Ba	455.403	ppm	1
Be	313.042	ppm	0.1
Ca	211.276	%	0.01
Cd	228.802	ppm	0.1
Ce	404.076	ppm	1
Co	230.786	ppm	1
Cr	267.716	ppm	1
Cu	324.754	ppm	1
Dy	353.170	ppm	0.1
Fe	296.690	%	0.01
K	766.490	%	0.01
La	333.749	ppm	1
Li	670.784	ppm	0.1
Mg	383.230	%	0.01
Mn	294.920	ppm	1

Mo	202.030	ppm	1
Na	589.592	%	0.01
Nb	316.340	ppm	1
Ni	231.604	ppm	1
P	178.284	ppm	1
Pb	220.353	ppm	1
Rb	780.023	ppm	1
Sc	361.384	ppm	0.1
Sr	407.771	ppm	1
Ti	374.164	ppm	1
V	310.230	ppm	1
Y	371.030	ppm	1
Zn	231.856	ppm	1
Zr	343.823	ppm	1

Since the ICP-OES analysis does not give results of the elemental content of carbon and nitrogen, additional C&N analysis was carried out using the Isotope-Ratio Mass Spectrometry (IRMS) method. The IRMS method can not only detect the C&N composition and C/N ratio but also their individual isotope ratios. The C&N analysis uses the Carlo Erba NA 1500 Series 2 Elemental Analyzer (EA), which is available in the Earth Resources Research and Analysis Facility (TERRA) of the Earth Science Department of Memorial University of Newfoundland. The sample preparation in this analysis only included weighing and packing of powdered samples. First of all, samples were weighed into tin capsules by using a microbalance and then introduced into the EA via an auto-sampler where the samples were flash combusted with oxygen in a 1020-1050 ^{o}C furnace. Then, Helium carrier gas moved the resultant gases through oxidation and reduction reactors and a water trap. The gases (CO_2 & N_2) were then separated on a GC column before entering the IRMS via a continuous-flow interface.

3.2.5 Radiocarbon Dating

Age determination is an important element in our core analysis because it helps not only in estimating the sedimentation rate but also in constructing an age-depth model. Although there are many dating techniques available for freshwater sediments, radiocarbon (^{14}C) dating, the earliest radiometric method available, is the most widely used (Björck & Wohlfarth, 2002). Since lake sediments usually contain a significant amount of organic carbon in the form of terrestrial, telmatic and limnic plant and animal debris, they are suitable for radiocarbon dating. The carbon sources from lake sediments can be either bulk sediments or macrofossils. Accelerator Mass Spectrometry (AMS) ^{14}C dating is a newly developed and frequently-used radiocarbon dating method that can be applied to an extremely small amount of carbon source for high-resolution dating. The AMS facility is available in the Advanced Research Complex (ARC) of University of Ottawa, currently the only AMS laboratory in Canada. I took samples to the AMS facility and analysed them myself while undergoing training. The background and principles of AMS ^{14}C dating can be found in numerous textbooks and articles. The description of the A.E. Lalonde AMS system and the analysis procedure and setup can be found in Kieser et al. (2015). Thus, I will focus on discussing the sample preparation methods in this section.

Sample preparation is a critical part of the whole AMS ^{14}C dating process because it greatly affects the data quality. The goal of sample preparation is to extract pure elemental carbon from samples for accelerator mass spectrometry and to reduce the sources of errors (e.g. carbonates) as much as possible. The standard sample preparation routine for AMS ^{14}C dating includes sample pre-treatment, combustion, CO_2 purification,

and graphitisation. The pre-treatment is different for different materials. The most common methods of pre-treatment for lake sediments are acid-alkali-acid (AAA) for macrofossils and acid (A) for bulk sediments. The pre-treatment guide can be found in Crann et al. (2016). Since our sediments lack macrofossils but contain a high content of organic matter, the acid method is applied on our samples. Figure 3.14 shows the

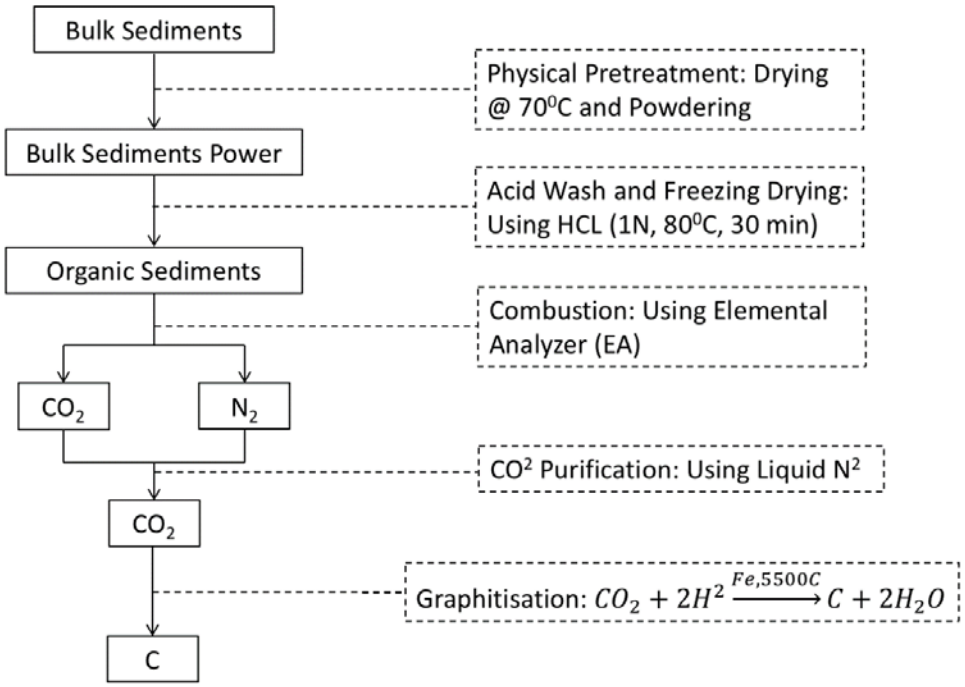

Figure 3.14 Simplified bulk sediments sample preparation steps for AMS dating.

steps of bulk sediments sample preparation for AMS dating. First of all, about 0.3 mg of each lake sediment sample was weighted and scooped into a glass tube, and then HCL (1N) was injected into these tubes to remove any inorganic carbon. The tubes were placed in an oven at 80 ^{0}C for half an hour to enhance the acid reaction with any dolomite. After the first acid wash, the sample was placed in a centrifuge (at 3000 rpm for 3 minutes) to

separate sediments and liquid. The acid was dumped and the tube refilled with pure water: this step was repeated 3 times to make sure no acid was left within the samples. Then, the samples were freeze-dried overnight. Since the target quantity of carbon for the AMS ^{14}C dating is 1 mg and the carbon percentage of our samples is about 20%, the pretreated, freeze-dried samples were placed into tin capsules in 5 mg aliquots. The samples were combusted using a Thermo Flash 1112 elemental analyzer (EA). Empty tin capsules were combusted between each sample to monitor the blank and ensure no memory effect. The output gases are CO_2 and N_2, and the mixed gases were cryogenically purified using liquid N_2 on a gas cleanup line. The purified CO_2 was eventually sealed in 6-mm pyrex breakseals. Finally, the pure CO_2 was converted to elemental carbon in the presence of iron and hydrogen using semi-automated graphitization lines (St-Jean, Kieser, Crann, & Murseli, 2016). The graphitized samples were then pressed into aluminum targets for AMS measurement.

3.3 Modelling of Lake Sediment Structures

Modelling of lake sediment structures is the final stage of our study. The main goal is to reconstruct the actual lake sediment structure that could be responsible for the stratification seen in the GPR profiles. However, before the lake sediment structure reconstruction, a synthetic GPR forward model algorithm has to be established by using the core log data to simulate the radar wave responses in the freshwater lake sediments. GPR forward modelling can be used: 1) to study the nature of the radar waves such as the source wavelet and the correlated physical properties that cause the radar wave reflection; 2) to enhance the GPR radargram interpretation; and 3) to predict the radar response of

complex lake sub-bottom layer systems.

The modelling work involved on this stage can be divided into two sub-stages: 1) in the first sub-stage, the aim is to develop a modelling algorithm that uses the available core log data to reproduce a 1-D synthetic radar trace that well correlates to the actual GPR trace. 2) In the next sub-stage, the radar responses of a series of scenarios for the sediment structures were simulated, and eventually the actual lake sediment structure reconstructed.

3.3.1 1-D GPR Trace Forward Modelling

GPR numerical modelling is a popular research topic in the near-surface geophysics community. There are currently a number of different GPR numerical modelling programs available ranging from simple ray-tracing and 1-D transmission-reflection (e.g. Goodman, 1994) to more complicated 3-D finite difference time domain (FDTD) solvers (e.g. Bourgeois & Smith, 1996). The choice for the modelling techniques depends on the 3-D geometry and structure of the subsurface target. The more complex the target is, the more sophisticated modelling technique should be used to get accurate results.

In this study, I used a simplified 1-D transmission-reflection method for the GPR forward modelling since our target structure consists of horizontal layers at the chosen coring sites (Figure 3.15). I wrote the necessary programs in Matlab. Referring to Eq. (3.2), the 1-D GPR forward modelling algorithm can be viewed as a result of the convolution of a GPR source wavelet *W(t)* and a series of 1-D reflection coefficients *R(t)*:

$$S(t) = W(t) * R(t) \tag{3.2}$$

where *S(t)* is the synthetic GPR trace. This method does not account for the energy loss after the EM waves travel through the media, so the model could be difficult to be evaluated where the actual GPR signal tapers out beyond certain depth. This simple model accepts only two inputs: the time domain source wavelet and a density log in depth. The GPR source wavelet can be either an idealized synthetic wavelet or the realistic wavelet extracted from a characteristic reflection. The reflection coefficients are usually calculated from impedance logs, which requires velocity information, but the only data that are available are the core density logs from MSCL. However, the velocity log can be calculated from the density log. Consequently, the GPR forward model in this study can be achieved by convolving a synthetic source wavelet and the reflection coefficient series from realistic core logging data.

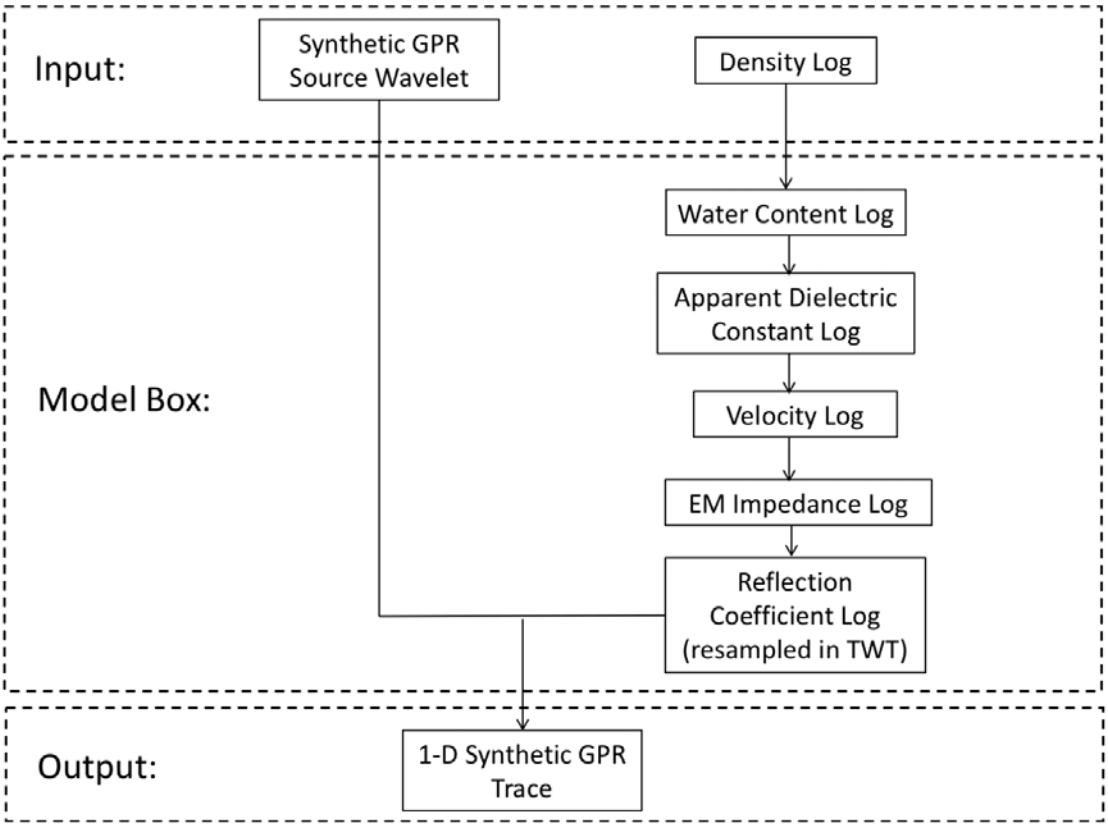

Figure 3.15 The flow chart of the simplified 1-D reflection-transmission modelling procedure.

The GPR source wavelet we used is the Berlage wavelet (Aldridge, 1990; Booth, Endres, & Murray, 2009), given by the equation:

$$W(t) = At^n e^{-\alpha t} \cos(2\pi f_0 t + \phi_0)\, H(t) \tag{3.14}$$

where A is the amplitude of the wavelet, n is the time exponent factor, α is the exponential decay factor, f_0 and ϕ_0 are the dominant frequency and initial phase angle, respectively, of the wavelet, and $H(t)$ is the Heaviside step function (i.e. $H(t) = 0$ when $t \leq 0$ and $H(t) = 1$ when $t > 0$). The Fourier transform of the Berlage wavelet is given by:

$$W(f) = \frac{A\Gamma(n+1)}{2(i2\pi)^{n+1}}\left[\frac{e^{+i\phi_0}}{(f-F_1)^{n+1}} - \frac{e^{-i\phi_0}}{(f-F_2)^{n+1}}\right] \tag{3.15a}$$

where

$$F_1 = +f_0 + i\left(\frac{\alpha}{2\pi}\right) \quad (3.15b)$$

and

$$F_2 = -f_0 + i\left(\frac{\alpha}{2\pi}\right) \quad (3.15c)$$

The GPR source wavelet with a dominant frequency of 100 MHz and its power spectrum are simulated by using Eq. (3.15a) and Eq. (3.15b), respectively (Figure 3.16). The frequency of the source wavelet is 100 MHz, which is the same frequency as in the GPR survey. The n and ϕ_0 are 2 and 0, respectively. The A and α are selected based on the time scale of the wavelet in Booth et al. (2009). The peak magnitudes of the simulated source wavelet and its power spectrum are both normalised. The power spectrum has a single peak located slightly lower than the dominant frequency 100 MHz, and the peak width is directly related to α. As this wavelet is an idealized GPR source wavelet, it has to be evaluated by comparing it to the actual wavelet in the GPR data during the modelling procedure.

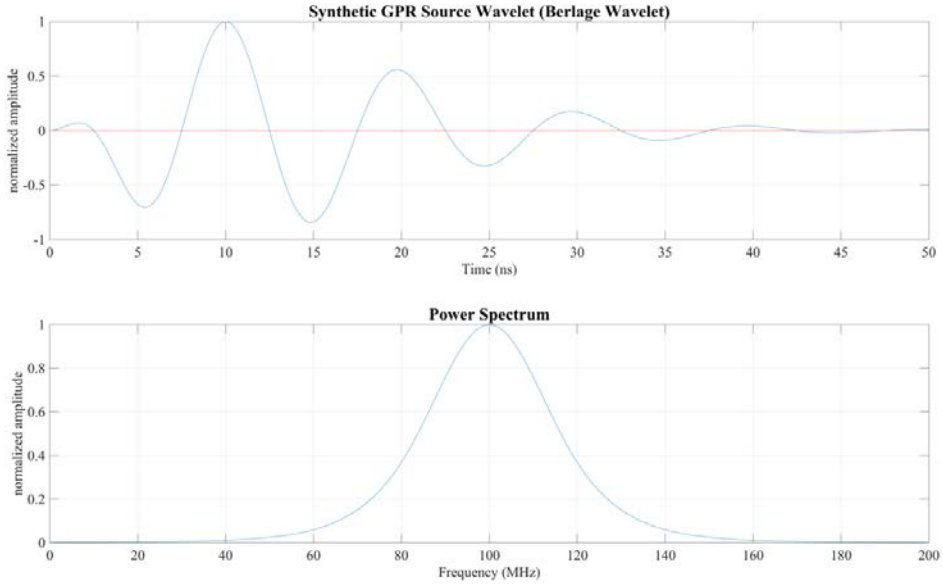

Figure 3.16 Simulated GPR source wavelet (100 MHz Berlage wavelet) and its power spectrum for the forward modelling.

The second input for the synthetic GPR forward model is the reflection coefficient series, which can be calculated from the impedance log. In order to obtain the impedance log, the velocity log must be known. Although the velocity information is not directly extracted from the MSCL data, it can be calculated from the MSCL gamma density log. First, the gamma density log has to be transferred to a volumetric water content log. Then, the velocity log can be calculated from the volumetric water content log. Weber et al. (1997) provide a means to estimate the volumetric water content (%) and gravitational water content (%) for the saturated sediment cores from the gamma density measurements if the grain density is known or well-estimated. The equations are given by:

$$Volumetric\ Water\ Content = \frac{\rho_g - \rho_B}{\rho_g - \rho_w} \tag{3.16a}$$

$$Gravitational\ Water\ Content\ W = \frac{\rho_w}{\rho_B} \cdot \frac{\rho_g - \rho_B}{\rho_g - \rho_w} \tag{3.16b}$$

$$Volumetric\ Water\ Content = \frac{\rho_B}{\rho_w} \cdot Gravitational\ Water\ Content \qquad (3.16c)$$

$$\rho_g = \rho_B \cdot \left[\frac{\rho_w(W-1)}{\rho_B W - \rho_w}\right] \qquad (3.16d)$$

where ρ_g is the grain density, ρ_B is the bulk density and ρ_w is the pore water density. The volumetric water content can be estimated by comparing the resultant gravitational water content to the lab measured water content. When the water content log is available, the dielectric constant log can be calculated. Topp, Davis, and Annan (1980) has established an empirical relationship between apparent relative permittivity, ε_r, for frequencies between 1 MHz and 1 GHz and volumetric water fraction, θ:

$$\varepsilon_r = 3.03 + 9.3\,\theta + 146.0\,\theta^2 - 76.7\,\theta^3 \qquad (3.17)$$

The relative permittivity, also known as the dielectric constant, is the electrical permittivity divided by the permittivity of free space: $\varepsilon_r = \varepsilon/\varepsilon_0$. This relationship was established for mineral soils having various textures, and water contents between 0.02 and 0.45, however equation (3.17) was constrained to pass through the point for pure water at 20ºC (1,81.5) and Figure 3.17 shows that a smooth curve with little curvature connects the data regions. Topp et al. (1980) found their results insensitive to soil density, texture, salt content and temperature. They did find that organic soils had lower dielectric constants, by about 2-5 units over their range of water content, however they followed the same trend with water content. Applying Eq. (3.17) to the organic, water-rich lake sediments, the impedance contrasts may be slightly underestimated because the slope of the line at high water contents may be too shallow.

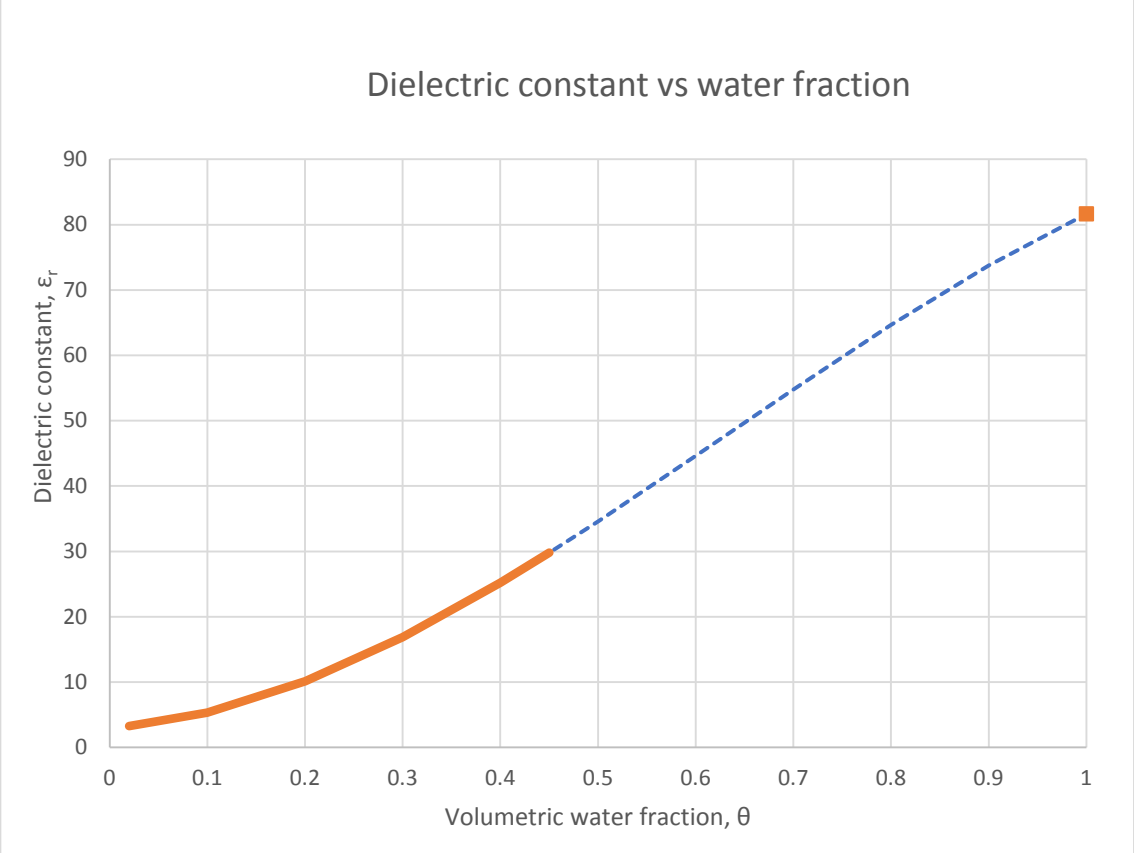

Figure 3.17 The relationship between dielectric constant and volumetric water fraction (Topp et al., 1980). The thick orange line and orange square are experimentally determined values. The dashed blue line is the fit to the data (Eq. 3.17).

Finally, in low-loss condition, the EM wave velocity can be calculated directly from apparent dielectric constants (Wyseure, Mojid, & Malik, 1997):

$$v = \frac{c}{\sqrt{\varepsilon_r}} \tag{3.18}$$

where c is the EM wave velocity in a vacuum. When the apparent dielectric constant is known, the EM impedance can be calculated by:

$$Z = \frac{Z_0}{\sqrt{\varepsilon_r}} = \frac{Z_0}{c} \cdot v \tag{3.19}$$

where Z_0 is EM impedance of free space, which is equal to 377 (A. Annan, 2009). Thus, the amplitude reflection coefficients R_i between two boundaries can be calculated by:

$$R_i = \frac{Z_i - Z_{i-1}}{Z_i + Z_{i-1}} = \frac{v_i - v_{i-1}}{v_i + v_{i-1}} = \frac{\sqrt{\varepsilon_r}_{i-1} - \sqrt{\varepsilon_r}_i}{\sqrt{\varepsilon_r}_i + \sqrt{\varepsilon_r}_{i-1}} \quad (3.20)$$

and TWT can be converted from core depth and P-wave velocity by:

$$TWT = \sum_{j=1}^{i-1} 2 \cdot \frac{\Delta z_j}{v_j} \quad (3.21)$$

where Δz_j is the layer thickness. The calculated reflection coefficients are resampled based on the new time axis calculated from the TWT before convolving with the source wavelet to create the synthetic radargram.

3.3.2 Synthetic Sediment Structures Modelling

In this section, a variety of conceptual models are constructed to simulate the radar responses in different lake sediment structures. The input parameters are the densities of multiple layers starting with an interval of 1 cm, which is the highest resolution used in the MSCL measurements.

The first model examines the effect of the sharpness of the reflection interface (Figure 3.18). The model includes two layers with a density of 1 g/cc increasing to 1.05 g/cc. The sampling interval of the synthetic density log is 1 cm. Three thicknesses of the interface from the top to the bottom are tested: 1cm, 10cm, and 18cm. The reflection coefficient log is calculated based on the density log, and the sampling interval is set to 0.8 ns. The synthetic GPR trace is created by convolving the resampled reflection coefficient log with a Berlage wavelet for a 100 MHz source, which has a total pulse length of about 45 ns (see figure 3.16). This corresponds to distance of 1.57 m at the assumed velocity of 0.035 m/s.

First, a perfectly sharp reflecting interface will generate a single wavelet that is

identical to the source wavelet (Berlage Wavelet in this case). As the model shows, the sharpness of the reflecting interface does affect the GPR wavelet. When the sampling interval is kept constant, the sharper the reflecting interface is, the stronger the reflection coefficient is, which results in a stronger GPR wavelet (in amplitude). As the sharpness of the interface decreases (the interface thickens to 10 cm), the GPR wavelet is reduced in amplitude and slightly delayed but retains the shape of the source wavelet until the sharpness decreases to a certain point. When the thickness of the interface increases to 18cm (about the half of the wavelength of the source wavelet), the reflected wavelet loses the source wavelength shape and most of its amplitude as parts of the wave reflected from different depths within the interface destructively interfere with each other. Thus, the thickness of the reflecting interface affects only the amplitude of the GPR reflections provided it is significantly less than a half wavelength of the source wavelet. For lake sediments, the interface between any two distinctive layers is usually within a few centimeters, so the effect of the reflecting interface thickness is not very important.

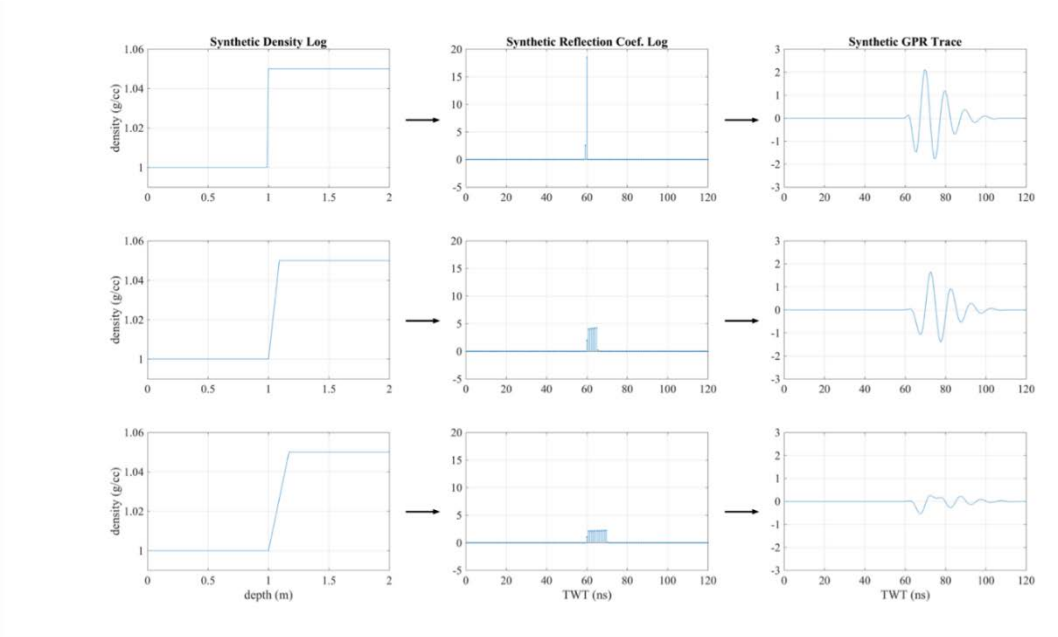

Figure 3.18 The effect of the sharpness of the reflecting interfaces. The model contains two layers with a density of 1 g/cc to 1.05 g/cc, and the thicknesses of the reflecting interfaces from the top to the bottom increase from 1 to 10 and 18 cm. The resolution of the density log is 1 cm, and the sampling interval of the resultant reflection coefficient log is 0.8 ns. The synthetic GPR trace is generated by convolving the synthetic reflection coefficient log and a 100 MHz GPR source wavelet (Berlage Wavelet).

The next model examines the effect of multiple layers within the sediments. This model mainly focuses on testing the GPR responses to the thickness of the intermediate layers. Model 2.1 (Figure 3.19A) contains 3 layers with densities of 1 g/cc, 1.05 g/cc, and 1.07 g/cc. Three thicknesses of the intermediate layer are modelled: 110 cm, 75 cm, and 53 cm. The 3-layer system produces 2 reflections, one from each of the interfaces between each layer. For the thickest intermediate layer, each reflection can be recognized as a whole source wavelet. As the distance between these 2 interfaces decreases, these two reflections approach to each other until the distance reaches a critical point where these two wavelets overlap. The minimum distance to distinguish two separate reflections depends on the length of the source wavelet. The model also indicates that the amplitude

of the reflection wavelet depends on the changing densities at the reflecting interface.

Model 2.2 (Figure 3.19B) is made to test the effect of the polarity of the reflected wavelet. All the parameters are the same as in model 2.1 except the density of third layer is set to 1.03 g/cc. This model shows the same result as the previous one but the polarity of the second wavelet is flipped relative to the original source wavelet due to the negative reflection coefficient, which is caused by the decreasing density across the second interface.

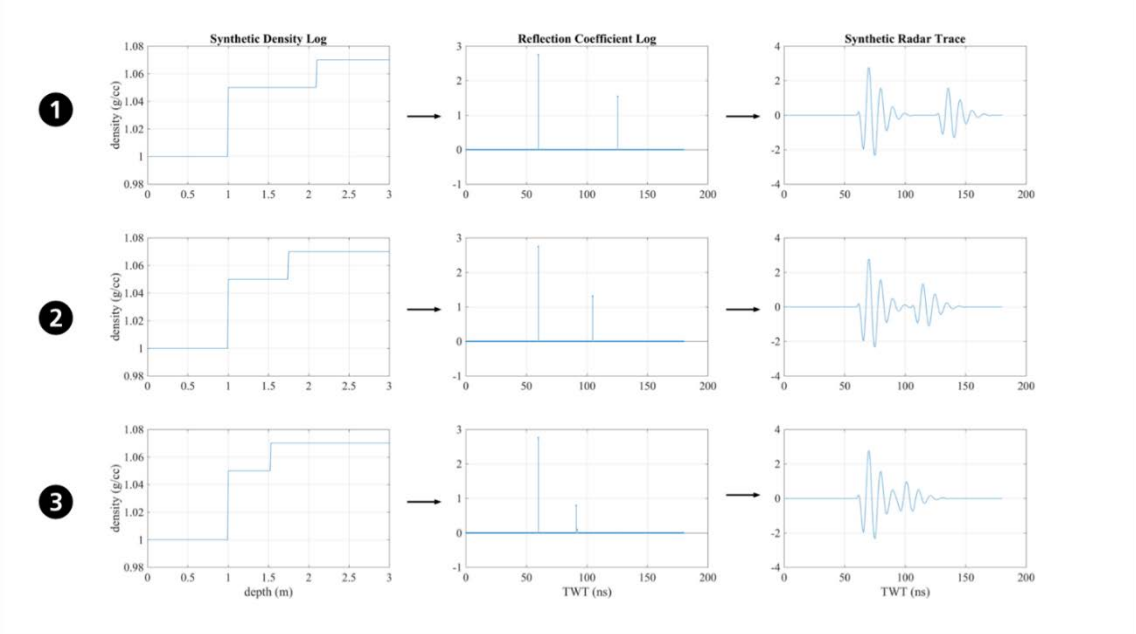

Figure 3.19 The effect of multiple layers in the sediments. The model contains 3 layers with a density of 1 g/cc, 1.05 g/cc, and 1.07 g/cc, respectively. The thickness of the intermediate layers from the top to the bottom decrease from 110 cm to 75 cm, and ends at 53 cm.

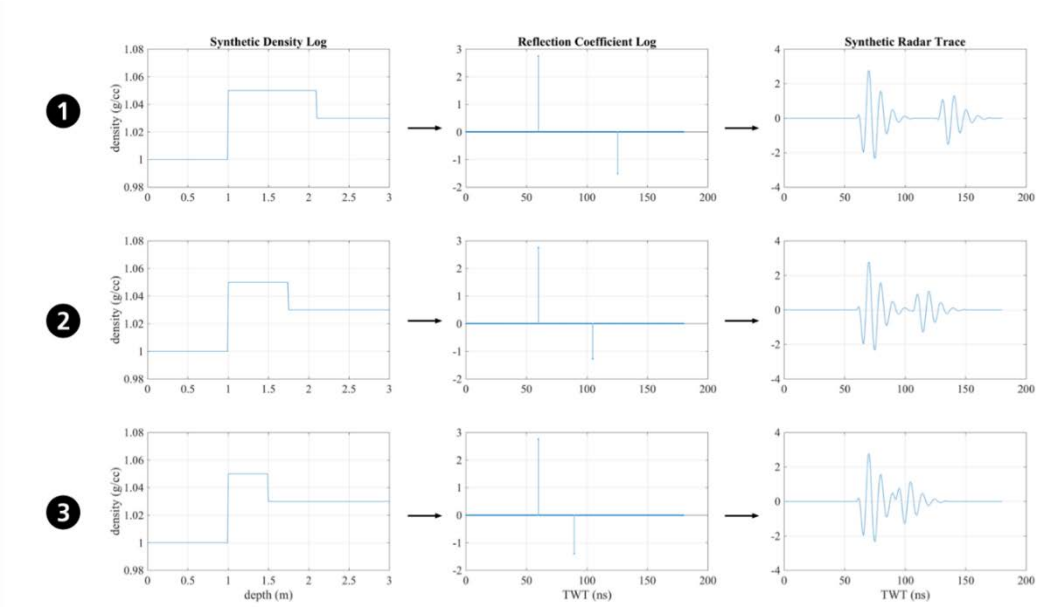

Figure 3.20 The effect of multiple layers in the sediments. The model contains 3 layers with a density of 1 g/cc, 1.05 g/cc, and 1.03 g/cc, respectively. The thickness of the intermediate layers from the top to the bottom decrease from 110 cm to 75 cm, and ends at 53 cm.

Water-rich layers exist in the lake sediments, and they can generate significant reflections in the GPR profiles. The next experiment is to test the effect of water-rich layers on the GPR waves. The model contains a single water-rich layer with a density of 1.03 g/cc occurring within sediments with a density of 1.05 g/cc. A series of scenarios are simulated for the water-rich layer with different thickness (Figure 3.20). Starting from scenario 1 to scenario 5 (top to bottom), the thicknesses of the water-rich layers are set to 3 cm, 8 cm, 16 cm, 33 cm, and 66 cm, respectively. Of particular note, the thicknesses of the water-rich layers in scenario 3 (8 cm) and scenario 4 (16 cm) are about a quarter and a half of the wavelengths of the 100 MHz GPR waves propagating in the sediments. The water-rich layer in scenario 6 (66 cm) has the thickness about the length of the 100 MHz source wavelet.

As the model shows, the water-rich layer generates a negative spike and then a

positive spike in the reflection coefficient in all the scenarios due to the firstly decreased and then increased densities.

In the first scenario, the reflections caused by the water-rich layer are very weak because of the two opposite reflection coefficients cancelling out each other. In reality, the reflection caused by such a thin water-rich layer should be weaker, but the model shows it because of the sampling interval artifact resulting the two unequal opposite reflection coefficient spikes. This artifact could be improved (or even removed) by using a much smaller sampling interval in the code.

As the water layer thickness increases, the reflected wavelet caused by the water-rich layer reaches its maximum amplitude in scenario 2, and it starts to be deformed in scenario 3 where the layer thickness is about a half of the wavelength. The amplitude of the reflected wavelet by the water-rich layer increases with the increasing layer thickness until it reaches a quarter of the wavelength. Then, the amplitude decreases when the layer thickness increases from a quarter of the wavelength to a half of the wavelength. In scenario 3-5, the reflected wavelet becomes an overlap of two separate wavelets (marked by a & b, and separated by the red dashed line) when the water-rich layer thickness is layer than a half of the wavelength. These two separated wavelets are caused by the positive and the negative spikes at the beginning and the end of the water-rich layer, and they can be entirely distinguished when the thickness of the water-rich layer is larger than the wavelength of the source wavelet.

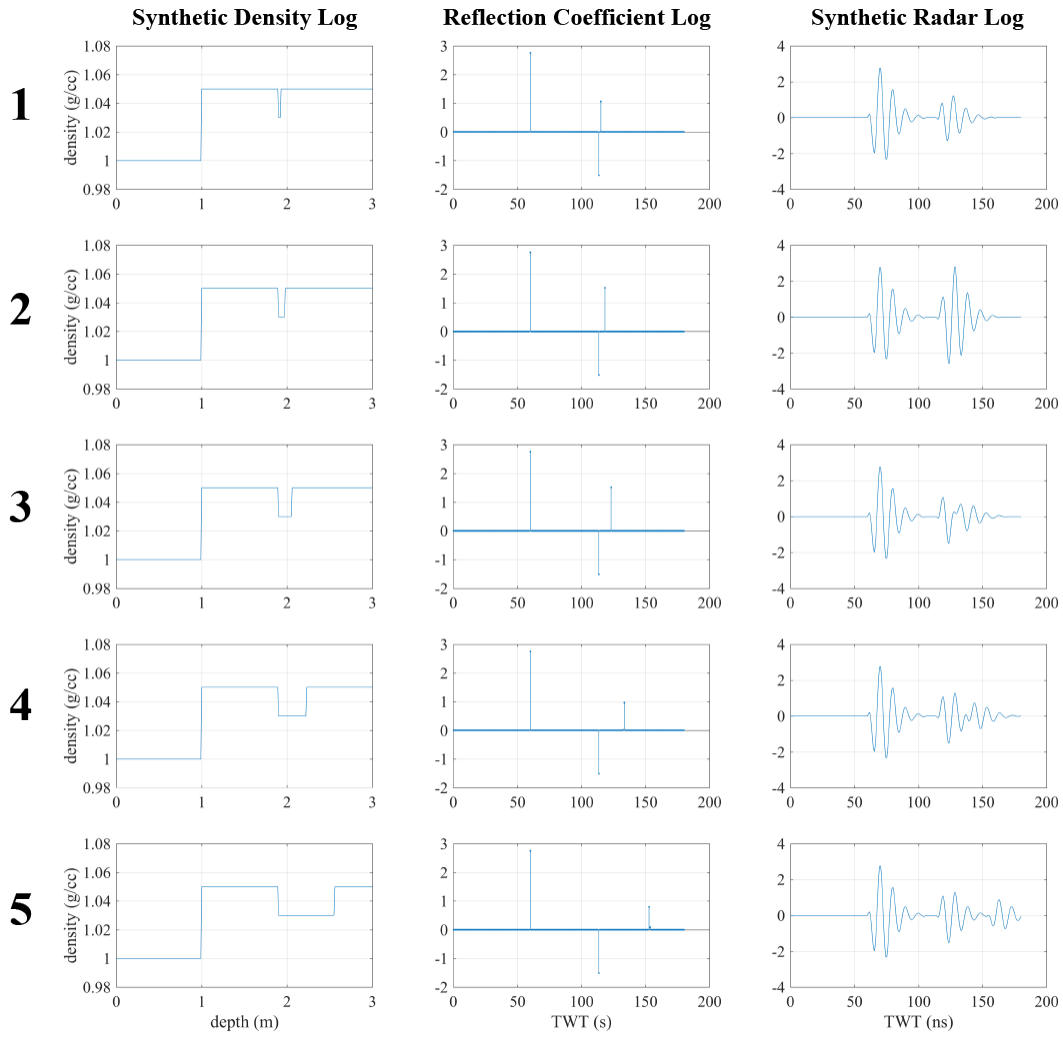

Figure 3.21 The effect of the water-rich layer on the GPR responses in the sediments. The model contains 1m water layer with a density of 1 g/cc at the top, and a base sediment layer with a density of 1.05 g/cc. The water-rich layer with a density of 1.03 g/cc starts at 90 cm of the sediment layer, and the thicknesses of the water-rich layer are 3, 8, 16, 33, and 66 cm from scenario 1 to 5, respectively. In scenario 1, the reflection caused by water-rich layer is very weak due to two reversed reflection coefficient spikes cancelling each other. In scenario 2, the reflection caused by the water-rich layer reaches its maximum amplitude and keeps the shape of one single wavelet, and it becomes an overlap of two separated wavelets (marked by a&b, where the red dashed line indicates the front of reflected wavelet b) in scenario 3-5.

Based on the results of these simple simulations, some observations can be made as following:

1) A GPR reflection interface is defined by two adjacent materials with different dielectric constants, and the GPR signal will produce a source wavelet shape like wavelet at each reflection interface. Since fresh water has a much higher dielectric constant than the other geological materials, a GPR reflection happens when there is a contrast between two materials with different water contents.
2) The sharpness of the reflection interface has a small effect on the reflected wavelet as long as the interface thickness is much less than the wavelength of the wavelet.
3) The strength of the reflected wavelet is proportional to the intensity of the changing dielectric constants of the materials.
4) The polarity of the reflected wavelet will be flipped if the reflected material has a higher dielectric constant (more water) than the previous pass-through material.
5) The type of layer and the layer thickness have a large impact on the GPR reflections. The type of layer decides the shape of reflection, and the thickness of a layer decides amplitude of the reflection and also the shape of the reflection.
6) If two or more reflection interfaces exist within the source wavelet length range, the shape of the reflected wavelet could be distorted as a result of wavelet overlapping. The layer has to be thicker than the length of the GPR source wavelet in the reflected material to distinguish these two reflection interfaces.

Chapter 4 Results and Discussion

4.1 Lake Basin Analysis

4.1.1 Exploratory geophysical surveying

The goal of the preliminary geophysical surveying is to identify suitable lakes as well as coring spots by gaining knowledge of the lake bottom bathymetry and sub-bottom sediment distribution. Sonar is the traditional surveying tool that is used for water body bathymetric mapping. Even though GPR is not often used for water body bathymetric surveying in the literature, it showed excellent performance in the freshwater body bottom and sub-bottom investigation in our study in eastern Newfoundland. In this project, we used both sonar and GPR in the preliminary geophysical surveying. GPR and sonar surveys were performed on Tippings Pond in the winter and summer of 2015, and GPR surveys took place on Grassy Pond during the winters of 2015 and 2016.

Figure 4.1 shows a comparison between GPR and sonar profiles, albeit on different lakes. The GPR profile (Figure 4.1A) was one of the GPR survey lines collected on Grassy Pond using 100 MHz antennas. The GPR profile shows not only the water-sediment interface but also the sediment-bedrock interface and continuous layers within the sediments, particularly where the sediments accumulated in lake sub-basins. (The depth scale on the GPR profile only represents the depth to bottom of the sediments because the radar velocity varies in different materials, such as water and sediments.) The sonar profile (Figure 4.1 B) is one of the sonar survey lines collected on Tippings Pond using a 200 kHz antenna. The sonar profile clearly shows the water-sediment interface, but the sediment-bedrock interface is not visible because the energy of the sonar wave is

attenuated after a few metres in the sediments. Moreover, the sonar does not capture any internal structures of the sediments.

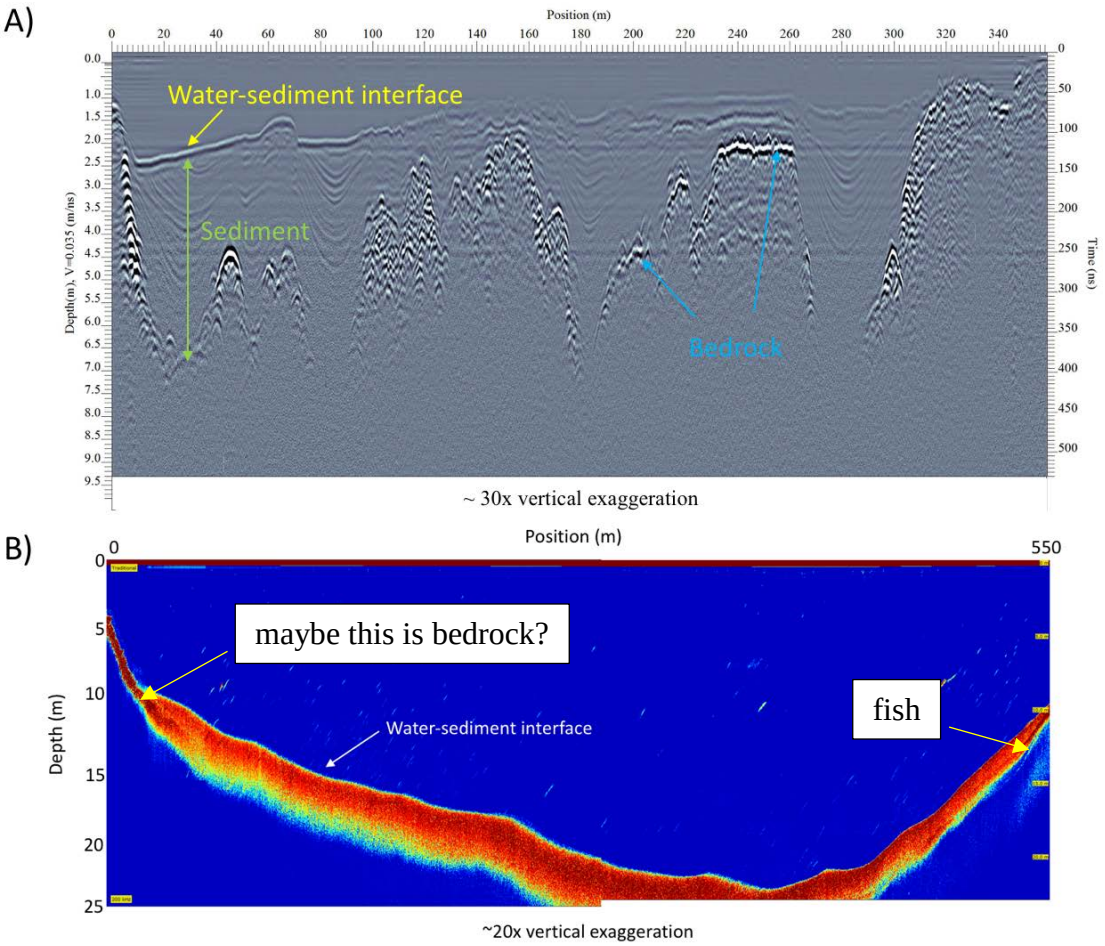

Figure 4.1 A comparison between GPR and sonar profiles for lake bottom profiling. A) the GPR profile using 100 MHz antennae on Grassy Pond. The GPR data is processed using dewow, spatial filtering, SEC gain, spiking deconvolution and bandpass filtering. B) the sonar profile using 200 KHz on Tippings Pond. There is no processing applied to the sonar data. The sediment-bedrock interface is not detected due to the signal loss.

The original plan for this thesis was to survey Tippings Pond using GPR. A preliminary GPR survey, where the GPR antennae were placed in custom-built skis, was accordingly performed on Tippings Pond during the winter of 2015. However, the GPR signal disappeared after penetrating the water a few meters (Figure 4.2). Since Tippings

Pond is near a community, road salt contamination may have been responsible for making the conductivity of this nominally fresh water pond too high for GPR signals to penetrate far. Although the sonar survey detects the bottom profile of Tippings Pond, the sonar bottom profiles do not show the detail revealed by the GPR profiles on Grassy Pond. In addition, the sonar profiles show that in the areas where the sediments accumulated the water is too deep for the current available coring equipment. Consequently, the study site was chosen as Grassy Pond.

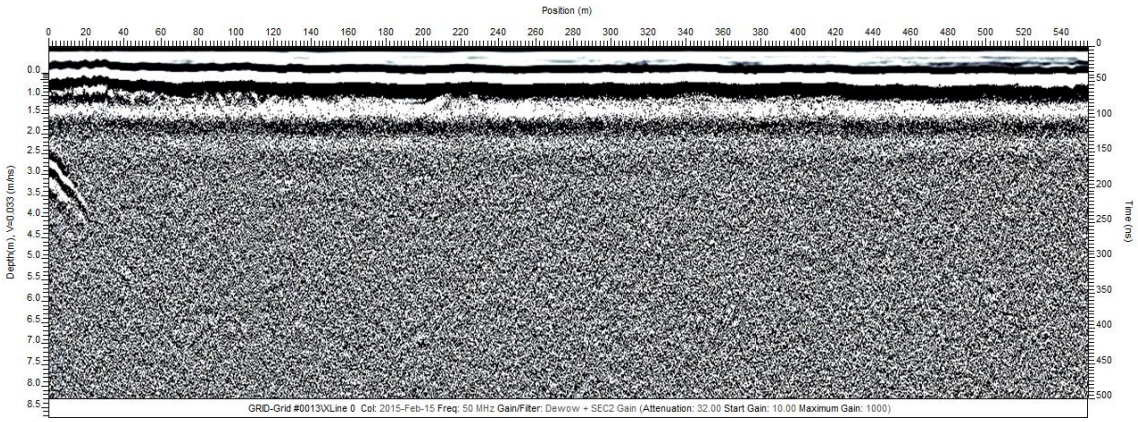

Figure 4.2 One of the 100 MHz GPR profiles on Tippings Pond. The GPR signal disappeared in the shallow water, due to the high conductivity of the pond water probably from human activities such as road salt contamination.

4.1.2 GPR data collection, processing and interpretation

After the exploratory geophysical survey, the study area and the survey tool were chosen as Grassy Pond and GPR. The reasons for this decision are summarized as follows. 1) GPR has a suitable penetrating depth in Grassy Pond since the water-sediment and sediment bedrock interfaces can be detected in the GPR profiles; while in Tippings Pond the GPR signal disappeared in the shallow water region due to the relatively high conductivity of the water. 2) Although the 200 kHz sonar detects the water-sediment interface, the sediment-bedrock interface in the sonar profile cannot be identified. 3) The

GPR profiles of Grassy Pond show the internal structures within the sediments as a sequence of continuous layers, while the sonar profile does not sense any sediment internal structure. 4) The water depth of Grassy Pond is suitable for the current available piston coring system, while the water depth of Tippings pond is much too deep.

The initial GPR data collection for Grassy Pond took place in the winter of 2015. A 100 MHz GPR grid with 50 m line spacing on the whole of Grassy Pond was made. A follow-up GPR survey took place in the winter of 2016. This survey obtained another 100 MHz GPR grid with a 50m line spacing offset from the original GPR survey in 2015, so the combined data resulted in a GPR grid with the line spacing of 25m (Figure 4.3A). In addition, several GPR survey lines with 50 MHz were also performed in the winter of 2016 to test the GPR response under a lower operating frequency (Figure 4.3B).

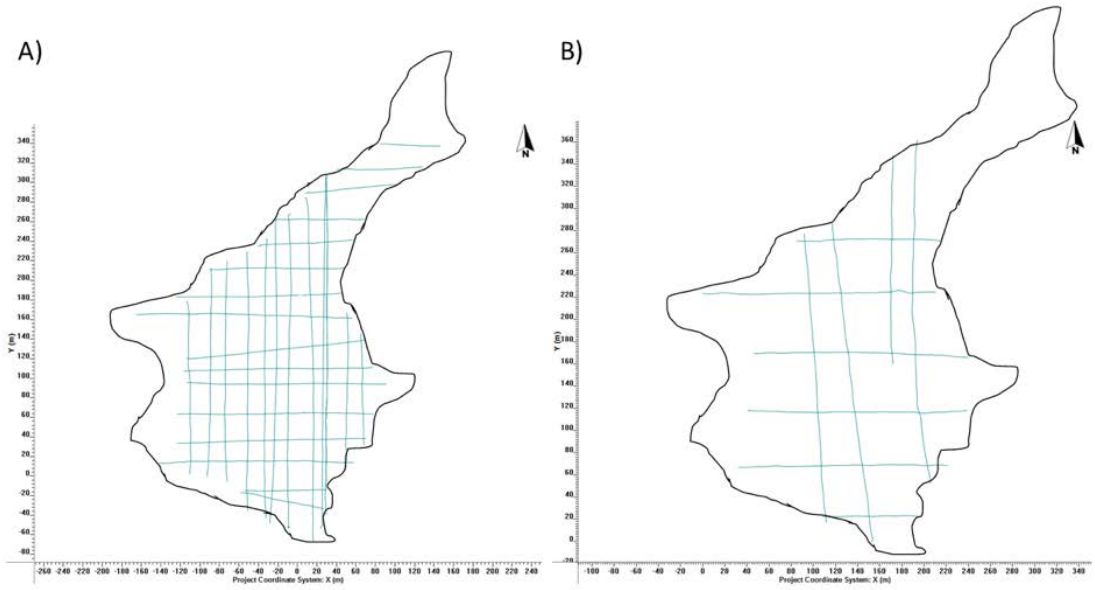

Figure 4.3 GPR grids on Grassy Pond. A) the 100 MHz GPR grid with 25m line spacing. B) the additional 50 MHz GPR Grid.

All the GPR data were collected using a Sensors and Software pulseEKKO Pro

system. Common offset profiles were obtained. The GPR system was mounted on a "Smart Cart" when surveying on the frozen pond ice surface, and the antennae spacing was fixed at 0.5 m for both frequencies. A GPS was attached to the GPR system, so the geographic information was attached to traces at regular time intervals. The acquisition mode was set as "free run", so the step size (the distance between traces) depends on the cart moving speed. The moving speeds were similar for each survey line, and the step sizes were mostly between 0.1 m and 0.15 m. For all the datasets, the total recorded two-way travel time (time window) was 470 ns with a temporal sampling interval of 800 ps, and the trace stacking was set at 8.

The processing for the GPR data followed the work flow described in Chapter 3. The GPR processing software used in this project is *EKKO_Project 3* by Sensors and Software, which was the default GPR processing software bundled with the pulseEKKO system. The processing flow for the profiles is summarized in Table 4.1. This work flow only contains basic processing steps. The first break alignment is about -29 ns for both antenna frequencies, and it is automatically applied to the GPR profiles by the system. The dewow filter is a routine GPR processing procedure. The time gain is chosen as exponential gain compensation (SEC). The spatial filter used is background subtraction. By carefully choosing the filter width, the air/ground wave at the top of the profiles and the horizontal noise bands can be removed but the original horizontal reflection can be kept. Topographic correction is not included in this work flow because the surveying platform in this project is a flat ice surface. The processing parameters in this flow work are set independently for each GPR profile. Advanced processing techniques, such as spiking deconvolution and migration, were not applied because they could introduce

artifacts to the dataset.

Table 4.1 Processing work flow and parameters for the GPR datasets. The parameters for the SEC2 gain and background subtraction varies for each individual profile.

Process	50 & 100 MHz Profiles
First break alignment	Static shift = -29
Dewow filter	DC removal: Window length = 1.33 ns
Time gain	SEC2 gain
Spatial filtering	Background subtraction

Figure 4.4A shows selected GPR profiles on Grassy Pond. These profiles include two 100 MHz GPR profiles surveyed in 2015 and 2016, and a 50 MHz GPR profile surveyed in 2016. All these profiles were taken from the N-S survey lines of similar locations, which are shown in the GPR grid on the right side. These survey line cover the most representative bathymetry of Grassy Pond, which includes several basins and ridges. Other GPR profiles in the 100 MHz and 50 MHz grids are included in the appendix. The GPR profiles cover about 300-meter survey lines. The depth axis is converted from the two-way travel time window by using an average radar velocity of 0.035 m/s, which was determined by analyzing hyperbolas related to boulders lying on the bedrock surface in all the profiles. This depth calibration was checked by comparing the predicted depth to bedrock with the measured depth at one of the coring locations.

The 2015 and 2016 100 MHz GPR profiles (Figure 4.4A a and b) are very similar as they used the same survey parameters on nearly the same survey lines. The 2016 50 MHz GPR profile (Figure 4.4A c) show a similar sub-bottom structure as the 100 MHz

profiles but with lower resolution. The agreement between these three GPR profiles indicates the reliability and repeatability of the dataset.

Processing of these GPR profiles included background subtraction, which removed unwanted signal from air waves and ground waves. However, where a strong horizontal reflection exists in the profile, such as that seen at about 3 m depth between positions 230 and 260 m in Figure 4.4Aa, background subtraction can introduce a corresponding artifact in the form of a dark horizontal band across the entire profile. Such artifacts must be recognized during interpretation.

Figure 4.4B shows the interpretation of these GPR profiles. The green line represents the water-sediment interface, and the blue line represents the sediment-bedrock interface. These two interfaces are characterized by the strongest reflections in the profile, especially from the bottom of the sediments due to the large electrical property contrast between sediments and bedrock. In some deep areas, the GPR reflection caused by the sediment-bedrock interface is not very clear (e.g. the area between position 80-90 m and 270-290 m in Figure 4.4Aa), due to natural signal attenuation.

Within the sediments, fine laminated continuous reflections, drawn by yellow dashed lines, can be seen, especially in the deep area of the lake sub-basins. These reflections are weaker than those from the top and bottom of the sediments, and are interpreted to be caused by changes in physical properties such as sediment composition or water content, as such changes could affect the electrical properties. The laminated reflections generally follow the shape of the underlying bedrock suggesting that they are related to sedimentary structures deposited over time. Of particular note, a strong horizontal reflection, indicated by dashed magenta lines, is observed in the shallow areas

between lake sub-basins in all these three profiles. Since this reflection has a different polarity than the reflections at the main interfaces (i.e. the polarity of this reflection is reversed), it is interpreted as a layer with slower radar velocity than in the surrounding materials, such as a water-rich layer within the sediments. This water-rich layer can be traced to the deep lake sub-basins indicating it is connected to the sediment laminations (see the right section of the magenta dashed lines appearing in all three GPR profiles).

Also shown in the profiles are a number of hyperbola on the sediment-bedrock interface (e.g. the hyperbolas on the blue line between position 230 to 260 m in Figure 4.4A), which could be caused by the diffractions from the boulders lying on the interface.

The 50 MHz profile (Figure 4.4C) show the sediment laminations in similar depth locations but with a wider separation (e.g. at the position between 20 and 30m), which is due to its lower resolution. As the electrical permittivity is a strong function of water content (Figure 3.17) an initial interpretation is that the reflections within the sediments are due to variations in water content; however, it has to be verified by analysis of the sediment cores.

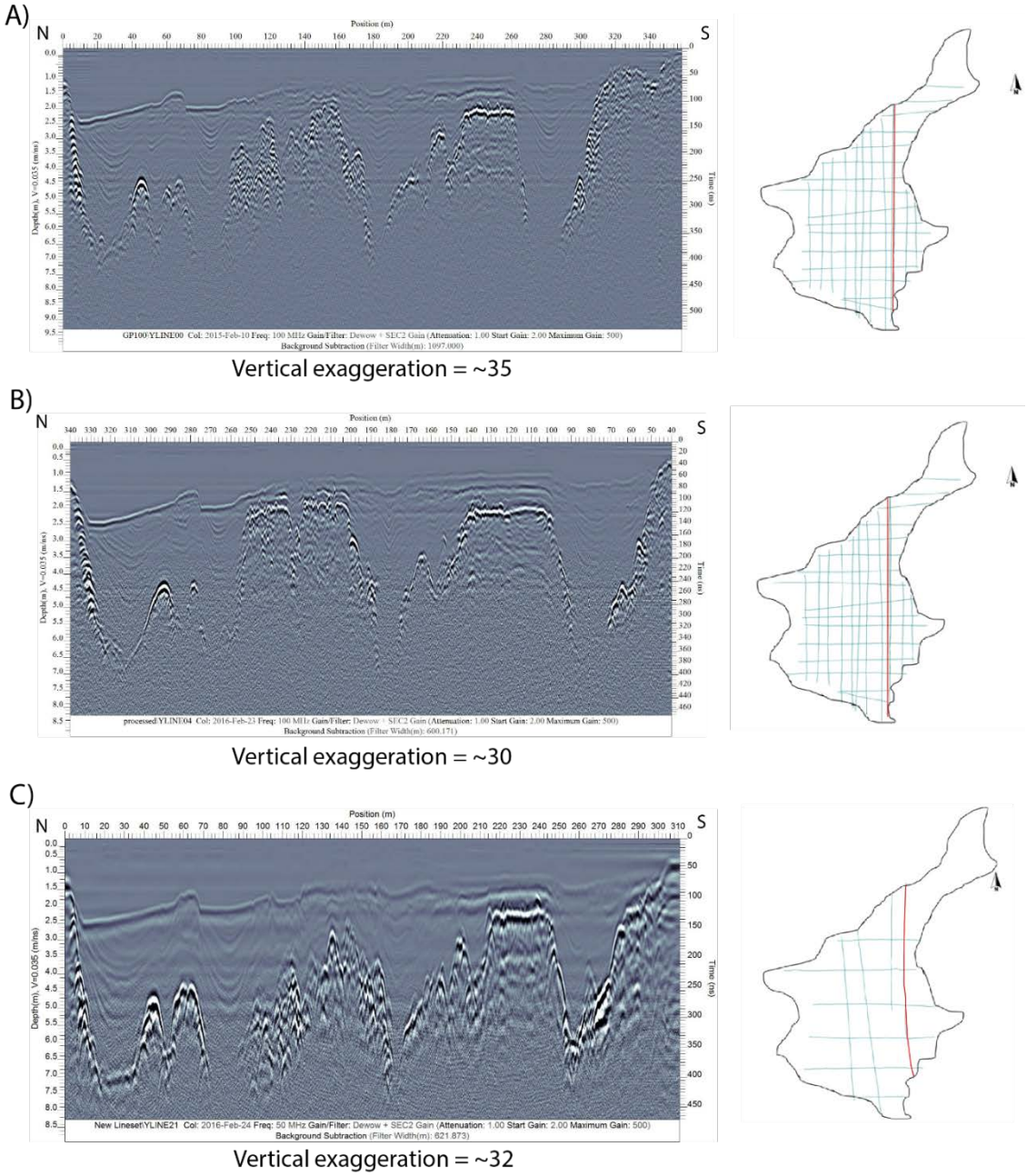

Figure 4.4 A An example of selected GPR profiles on Grassy Pond. A) the GPR profile with 100 MHz, recorded in 2015; B) the GPR profile with 100 MHz, recorded in 2016. C) the GPR profile with 50 MHz, recorded in 2016. These three GPR profiles are recorded in the survey lines with similar locations. The processing parameters are shown below each profile. The vertical exaggeration is about 30-35 for each profile.

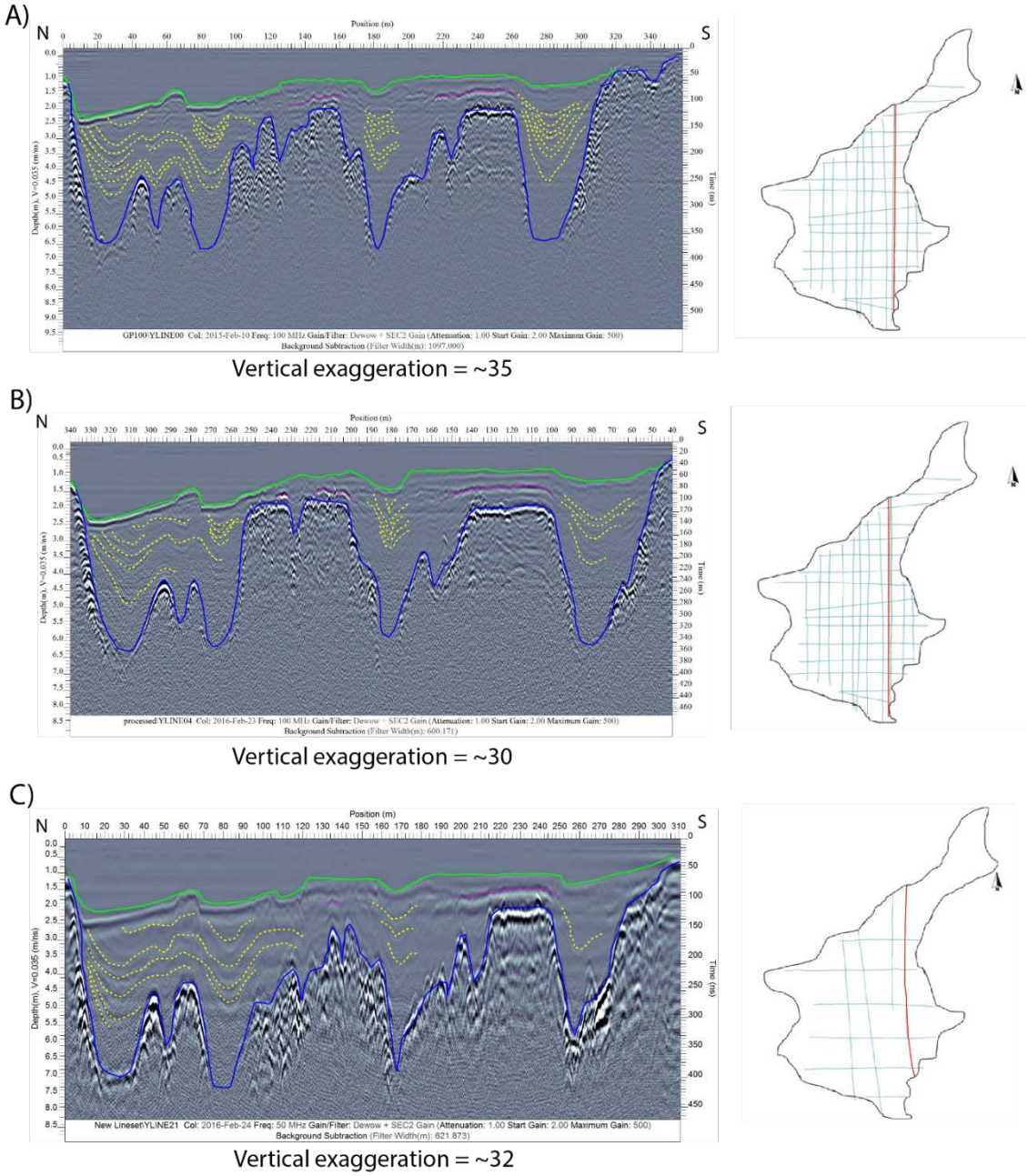

Figure 4.4B An example of selected GPR profiles on Grassy Pond with interpretation. A) the GPR profile with 100 MHz, recorded in 2015; B) the GPR profile with 100 MHz, recorded in 2016. C) the GPR profile with 50 MHz, recorded in 2016. These three GPR profiles are located in the survey lines with similar locations. The processing parameters are shown below each profile. The vertical exaggeration is about 30 for each profile. Interpretation: the green line and the blue solid line represent the top and bottom of the sediments, respectively; the yellow dashed lines represent

the laminations in the sediments at deep lake sub-basin area, and the magenta dashed line represents a water rich layer within the sediments at the shallow area between lake sub-basins.

4.1.3 Lake bottom and sub-bottom visualization

The lake bottom and sub-bottom maps of Grassy Pond require depth information for the interfaces of the water-sediment and sediment-bedrock interface. In the GPR profile, the system records the two-way travel time information instead of depth, so the velocity information must be known to estimate the depth. The depth information for these two interfaces is obtained by using the conceptual model (Figure 3.9), which is described in Chapter 3. The two-way travel time for the water-sediment interface (t_1) and sediment-bedrock interface (t_2) can be obtained by exporting the interpretation lines from *EKKO_Project 3*. The ice thickness (L_1) is measured in the field, and the radar velocities of ice (v_1) and water (v_2) are known (Table 3.1). Thus, the depth for the water-sediment interface (h_1) can be calculated by Eq. 3.5. The average radar velocity (v_{ave}) from the surface to the bedrock can be estimated by the hyperbola analysis, which is carried out by using the hyperbola analysis tool in the *EKKO_Project 3* on over 30 hyperbolas from the 50 & 100 MHz profiles. The average radar velocity from the surface to the bedrock is estimated as 0.035 m/ns. Thus, the depth to the bedrock (h_2) can be calculated by Eq. 3.6.

The visualization maps for both sediments and bedrock can be created by using the data points taken from the interpretation polylines from all the GPR profiles in *EKKO_Project 3* (e.g. the green and blue polylines shown in figure 4.4B), as well as the data points of the pond outline taken from the *Google Map* database. Since a GPS system was attached to the GPR during the survey, each point in the GPR profiles contains its geographic coordinates, such as UTM Easting and UTM Northing. The depth information

can be calculated from the two-way travel time by using E.q. 3.5 or E.q. 3.6. Thus, each data point contains its 3-D information (UTME, UTMN, and depth). Mathworks *Matlab* was used to create the 3-D maps for the water depth (bathymetry) and bedrock depth by interpolating these 3-D scattered points into a 3-D grid with a 4x4 m cell size and drawing the surface (Figure 4.5).

Figure 4.5a shows the Grassy Pond bathymetric visualization, and Figure 4.5b shows the Grassy Pond depth-to-bedrock visualization. The bathymetric map indicates the deepest water of about 2.8 m is located at the northeast of the pond, while the bedrock map shows the deepest point of the bedrock is about 8.3m from the water surface located at multiple locations in the northeast, middle, and southeast of the pond. The actual depth of the deepest point of the bedrock could be more than 8.3m because this depth map is based on the data points on the interpretation lines and these lines do not cover some of the bottom of the bedrock basins. The west of the pond is seen as a shallow area for both water and bedrock, while the east part of the pond is made of some deeper basins which contain most of the sediments. Generally, the bathymetry follows the bedrock depth, as seen in these two maps.

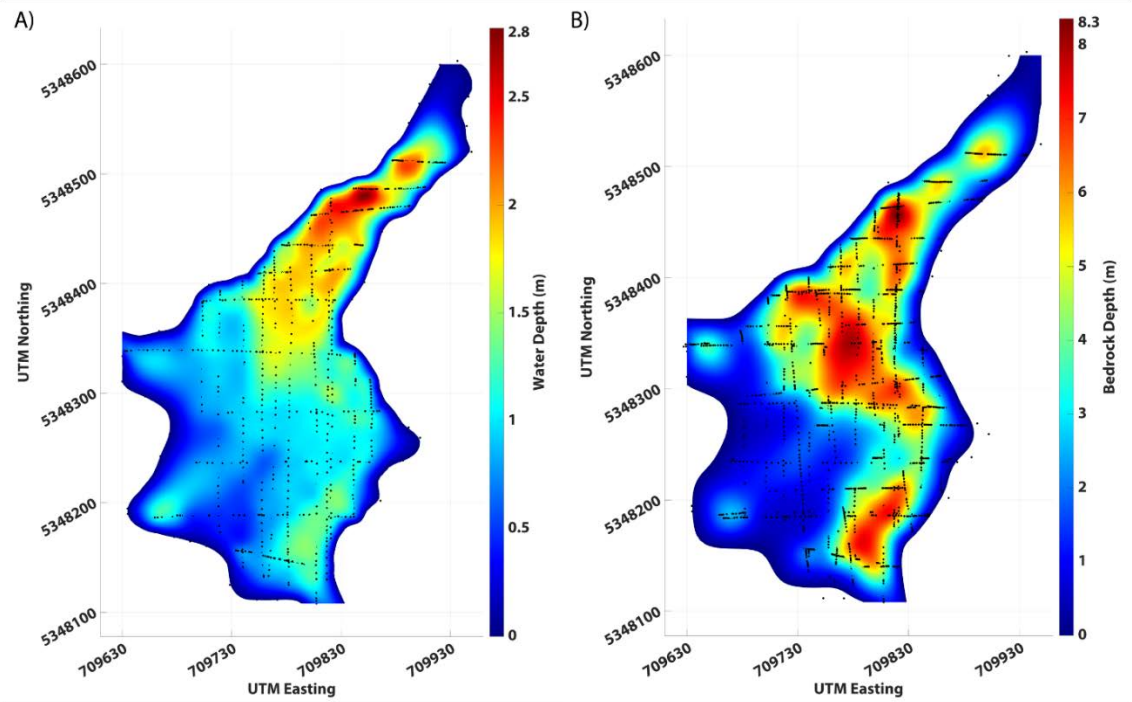

Figure 4.5 Visualization for the bottom and sub-bottom of Grassy Pond. a) the sediment bathymetric map of Grassy Pond; b) the depth-to-bedrock map for Grassy Pond. The black dots are the 3-D data points that are used to create these maps.

4.2 Lake Sediment Analysis

4.2.1 Sediments distribution, coring locations and their GPR profiles

A sediment thickness map can be created from the difference between the bathymetric map and depth-to-bedrock map. Figure 4.6 shows the sediment distribution map that is created by performing matrix subtraction of the interpolated cells between the sediment and bedrock 3-D points grid. The sediment distribution map is an effective guide for the sediment coring, and the coring locations are also indicated on this map. The sediments are most accumulated in the central area of the pond with a peak thickness of 6.3 m, and the sediment thickness is not consistently related to water depth.

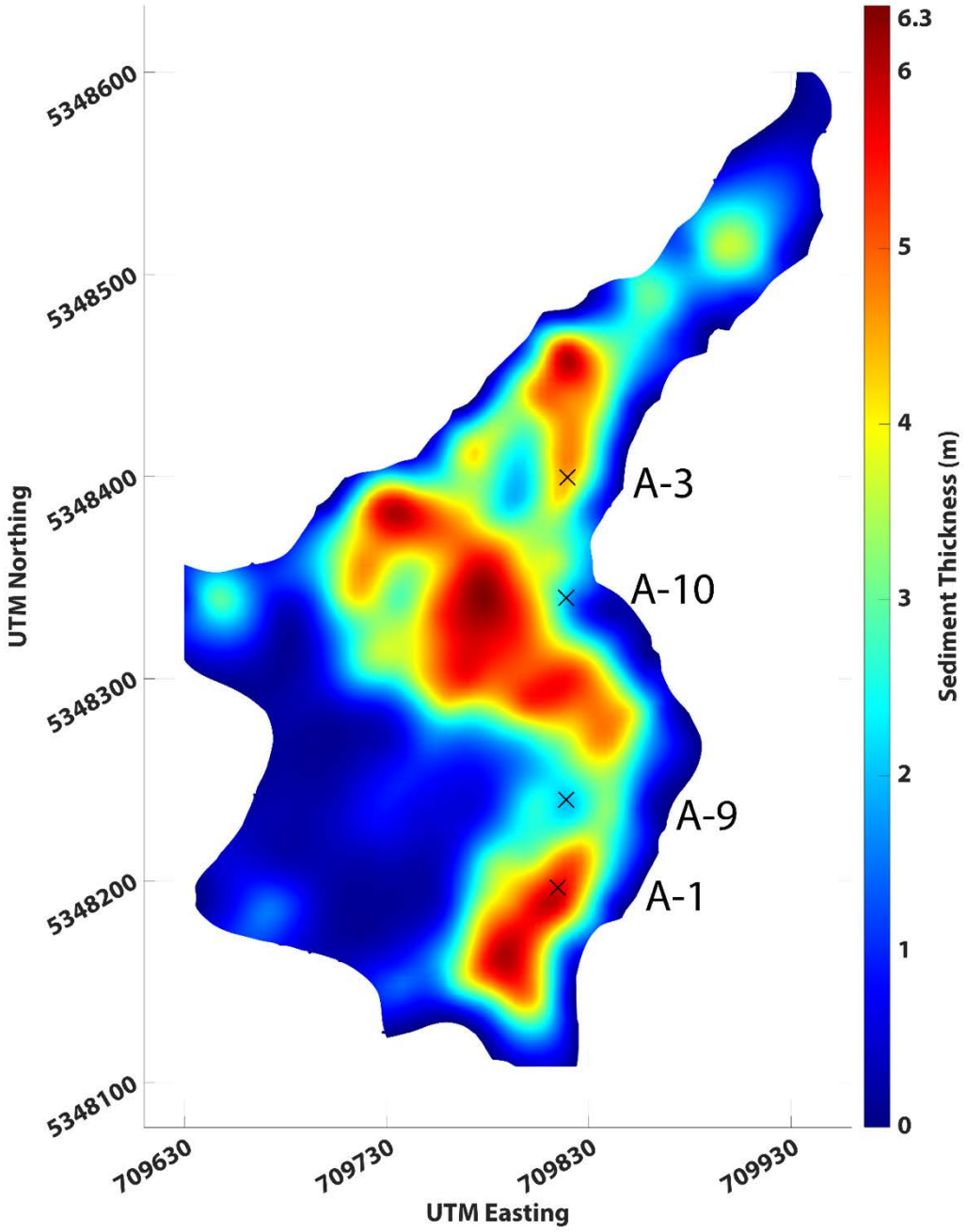

Figure 4.6 Sediment thickness map of Grassy Pond. The coring locations are also shown in this map.

Besides producing useful bathymetric and depth-to-bedrock maps, the 3-D

scattered data points can be used to estimate the pond water surface area and the total volume of the water and sediments.

The pond water surface area can be calculated by using the points on the outline of the pond. These points lie on the same plane (depth = 0 m), so the area can be calculated by using the "polyarea" function in *Matlab*.

The sediment and bedrock depth values are interpolated on the same rectangular mesh grids during the creation of the maps. Consequently, the volume above these interfaces – that is, the water volume and the volume of water plus sediments – can be estimated by directly summing the product of interpolated interface depths and the cell size. The sediment volume is then calculated by the subtraction of the water volume from the water plus sediment volume. The results of the calculations of pond water surface area and the volume of the water and sediments are shown in Table 4.2. These values are later used in the calculation of the carbon content of the pond.

Table 4.2 The estimated surface area, water volume and sediment volume of Grassy Pond.

Surface area	65,310 m^2
Water volume	62,040 m^3
Sediment volume	143,700 m^3

Using the sediment distribution map as a guide for the sediment coring, four cores at different locations in Grassy Pond were obtained during the winter of 2016. The coring equipment was a rod-driven piston corer. The core liner is a 3.05 m (10 feet) long transparent plastic tube with an inner diameter of 6.7 cm (2 5/8th inches) and an outer diameter of 7.3 cm (2 7/8th inches). The cores include two long cores (A-1 and A-3, >

2m) in the major sediment accumulated areas where the GPR profiles show continuous GPR reflections in the sediments, and two short cores (A-9 and A-10, < 2m) in the less sedimented areas. For the GPR records of each core, two perpendicular 50 m long GPR profiles centered on each individual core location were taken in the E-W and N-S directions after the coring process. Table 4.3 shows the information for each core, including its capture date, weight, length, geographic locations, and related GPR profiles. Figure 4.7 shows the general coring locations and positions in the 2D cross-pond GPR profile.

Table 4.3 Sediments coring information.

Core #	Weight (kg)	Length (cm)	UTME	UTMN	Ice Thickness (cm)	Sediment Depth (cm)	GPR E-W	GPR N-S
A-1	10.33	233	709814.7	5348196.51	27	130	X04	Y04
A-3	19.215	444	709819.47	5348399.57	25	192	X01	Y01
A-9	5.135	108	709818.84	5348240.07	28	88	X03	Y03
A-10	7.15	154	709818.84	5348339.93	25	100	X02	Y02

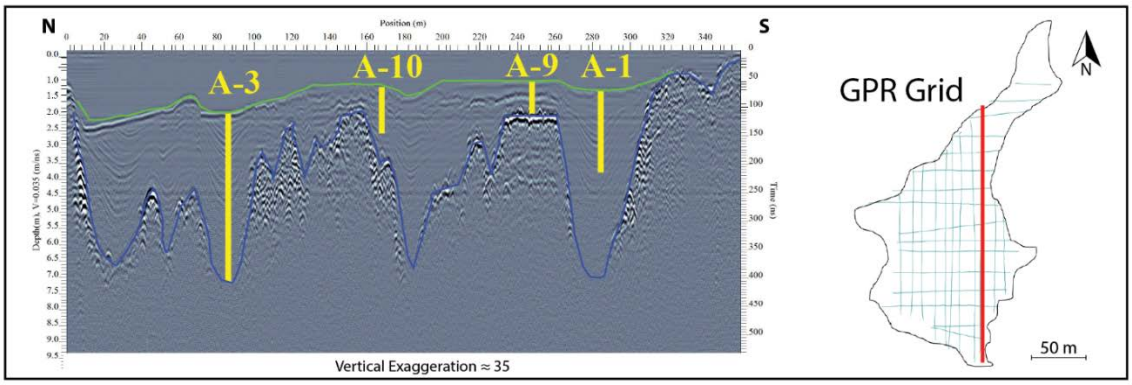

Figure 4.7 The approximate coring locations and positions show on the cross-pond GPR profile. The green and blue lines on the GPR profile indicate the top and bottom of the sediments, the yellow lines indicate the core locations, and the red line on the GPR grid indicates the location of the GPR profile.

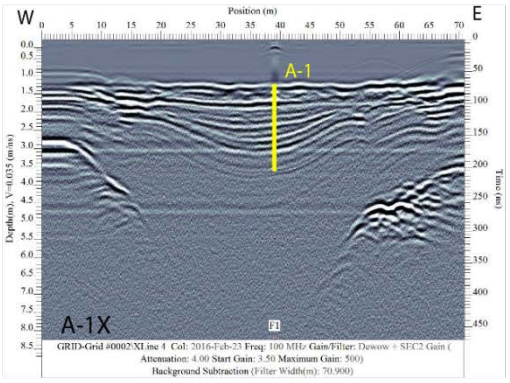
W
E
Position (m)
A-1
A-1X
Depth(m), V=0.035 (m/ns)
Time (ns)

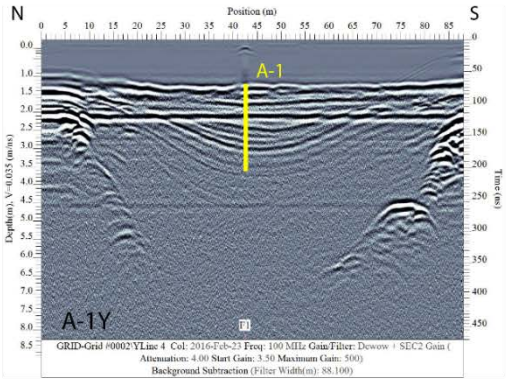
N
S
Position (m)
A-1
A-1Y
Depth(m), V=0.035 (m/ns)
Time (ns)

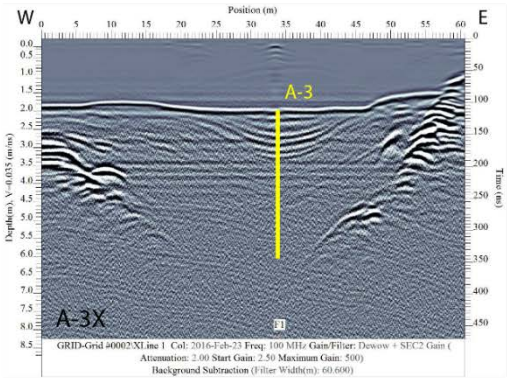
W
E
Position (m)
A-3
A-3X
Depth(m), V=0.035 (m/ns)
Time (ns)

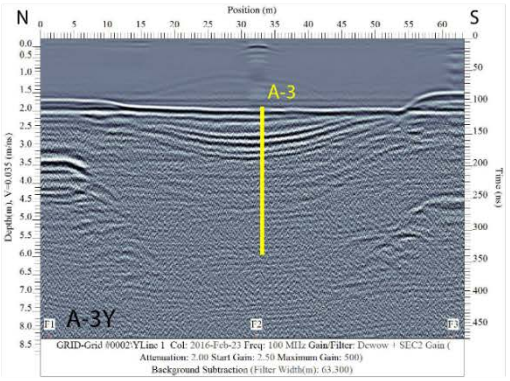
N
S
Position (m)
A-3
A-3Y
Depth(m), V=0.035 (m/ns)
Time (ns)

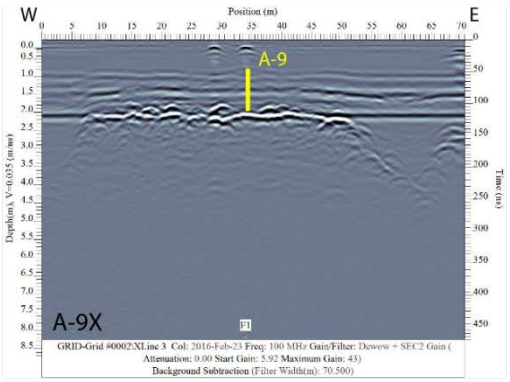
W
E
Position (m)
A-9
A-9X
Depth(m), V=0.035 (m/ns)
Time (ns)

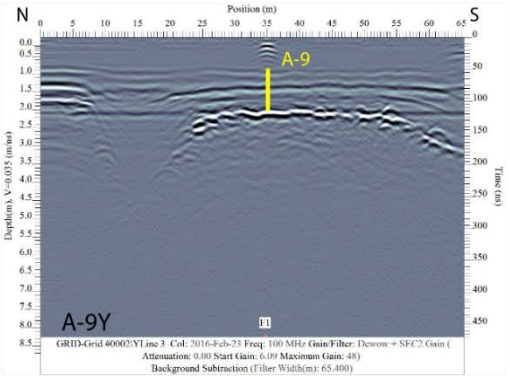
N
S
Position (m)
A-9
A-9Y
Depth(m), V=0.035 (m/ns)
Time (ns)

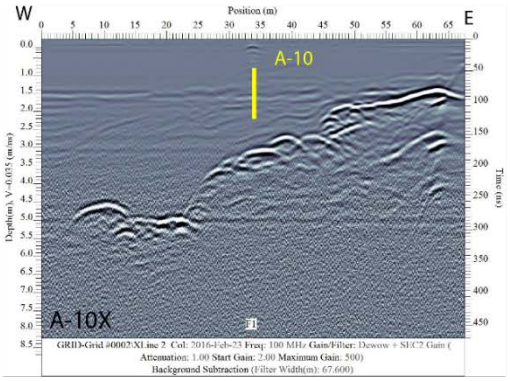
W
E
Position (m)
A-10
A-10X
Depth(m), V=0.035 (m/ns)
Time (ns)

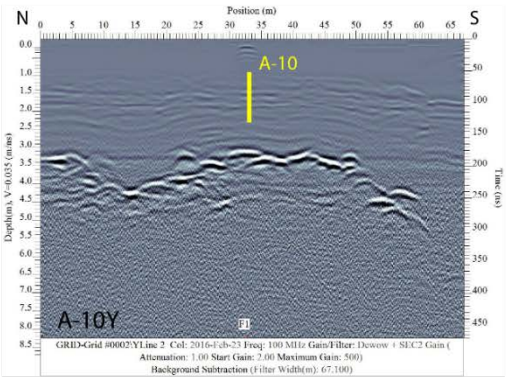
N
S
Position (m)
A-10
A-10Y
Depth(m), V=0.035 (m/ns)
Time (ns)

Figure 4.8 The 100 MHz 50 m long GPR profiles over each coring location with the core positions in the sediments. The GPR survey parameters are shown below each subplot. The radar velocity (0.035 m/ns) used for the depth axis in each profile is the average radar velocity from the surface to the bedrock based the hyperbola analysis.

The GPR profiles over each coring location are shown in Figure 4.8. These GPR profiles contain the approximate positions of the cored sediments above the fiducial points (F1 shown in the profiles) marked when the GPR system passed the coring spots. For convenience, all these profiles use the average radar velocity of 0.035 m/ns from the ice surface to the bedrock. Although all these GPR profiles were performed after the coring process, the GPR profiles indicate the reflections in the sediments are undisturbed by the coring procedure. The only signs of the coring in the profiles are the hyperbolas at short time related to the augered hole in the ice. The SEC gains for the profiles containing the long cores (A-1 and A-3) are set higher than the gains for the ones with the short cores (A-9 and A-10), so the continuous reflections in the deeper sediments are emphasized.

The GPR records in both directions shows the same reflection patterns at the core location, especially for the long cores (A-1 and A-3). In profiles A-3X and A-3Y, core A-3 covers most of the visible reflections in the sediments between 100 and 200 ns. After 200 ns, the reflected GPR signals are very weak, due to signal attenuation. In profile A-1X and A-1Y, core A-1 covers part of the visible layered reflections in the sediments. These reflections are still visible after 200 ns but their strengths are very weak compared to the reflections on the top. The GPR reflections covered by the two shallow water cores (A-9 and A-10) look more irregular than the ones covered by the long cores. Interestingly, there is a polarity reversed strong reflection that happens in the middle of core A-9 at about 90 ns in both profile A-9X and A-9Y. This flipped reflection could be caused by a

layer with slower radar velocity (e.g. a water-rich layer) within the sediments, and this particular reflection occurs at most of the shallow water area in Grassy Pond.

4.2.2 Physical properties

The direct observation of the sediment cores shows they are mostly uniform dark brown with no visible signs of layering. Thus, the first step in processing the sediment cores was to put them into a Multi-Sensor Core Logger (MSCL) by GEOTEK Inc. for the investigation of their physical properties, including Gamma density (wet bulk density), P-wave velocity, magnetic susceptibility, and electrical resistivity. The approximately 1.5 m long pieces of core were sealed in the field and transported to the core storage room before the MSCL scanning. Unfortunately, because the MSCL was non-operational at the time, there was an undesirable time lag of several weeks between the core collection and the logging, which led to water loss in some of the cores, especially at the top. After the automatic core logging, the cores were cut and sub-sampled about every 10 cm for further physical properties measurements. The gravitational water content were directly measured by weighing the core materials before and after drying. Additional DC resistivity and IP tests were also performed by using a SCIP system rented from GDD Inc.

The results of the physical properties for each core are shown in Figure 4.9. These results include the Gamma density and P-wave velocity measurements for each core from the MSCL, the direct gravitational water content measurements, and the DC resistivity and IP measurements from the SCIP tester. For all four cores, the resistivity and magnetic susceptibility are out of the detection range of the MSCL. There is water loss at the top of

each core section resulting in air gaps in the sediments, which is indicated by the drops of the gamma density and P-wave velocity between the core sections. The water loss is also confirmed by core inspections before the logging process.

The average measured gravitational water contents (water content by weight) for core A-1, A-3, A-9, and A-10 are 92.5%, 92.3%, 86.3%, and 87.4%, respectively. The water content of these shallow water sediments cores is significantly higher than the water content of most common marine sediment cores. Specifically, the water contents of the cores (A-1 and A-3) in the deep sediment accumulated areas are slightly higher than the ones (A-9 and A-10) in the shallow areas.

The wet bulk density (gamma density) and the water content are inversely correlated for all four cores. This observation makes sense because water is less dense than the grains in the sediments, so the density of the sediment will decrease if its water content increases. The wet bulk densities for all cores are all only slightly above the density of fresh water because the water content of these sediments is very high.

Theoretically, the P-wave velocity should be correlated to the wet bulk density because the P wave travels faster in denser materials. However, this relationship is not very consistent for all the cores, which could be caused by the MSCL P-wave velocity sensor that is not that sensitive in such light materials. The difference between P-wave velocities and densities could also be due to the anisotropy, if the sediments contain significant clay minerals, where the P-wave travels faster along clay minerals than perpendicular to them.

The relationship between the resistivity and chargeability and other physical properties is not very clear. However, the chargeability can be generally correlated to the

density in all four cores. The factors that affect the resistivity and chargeability could be related to the fresh water content and clay minerals in the sediments.

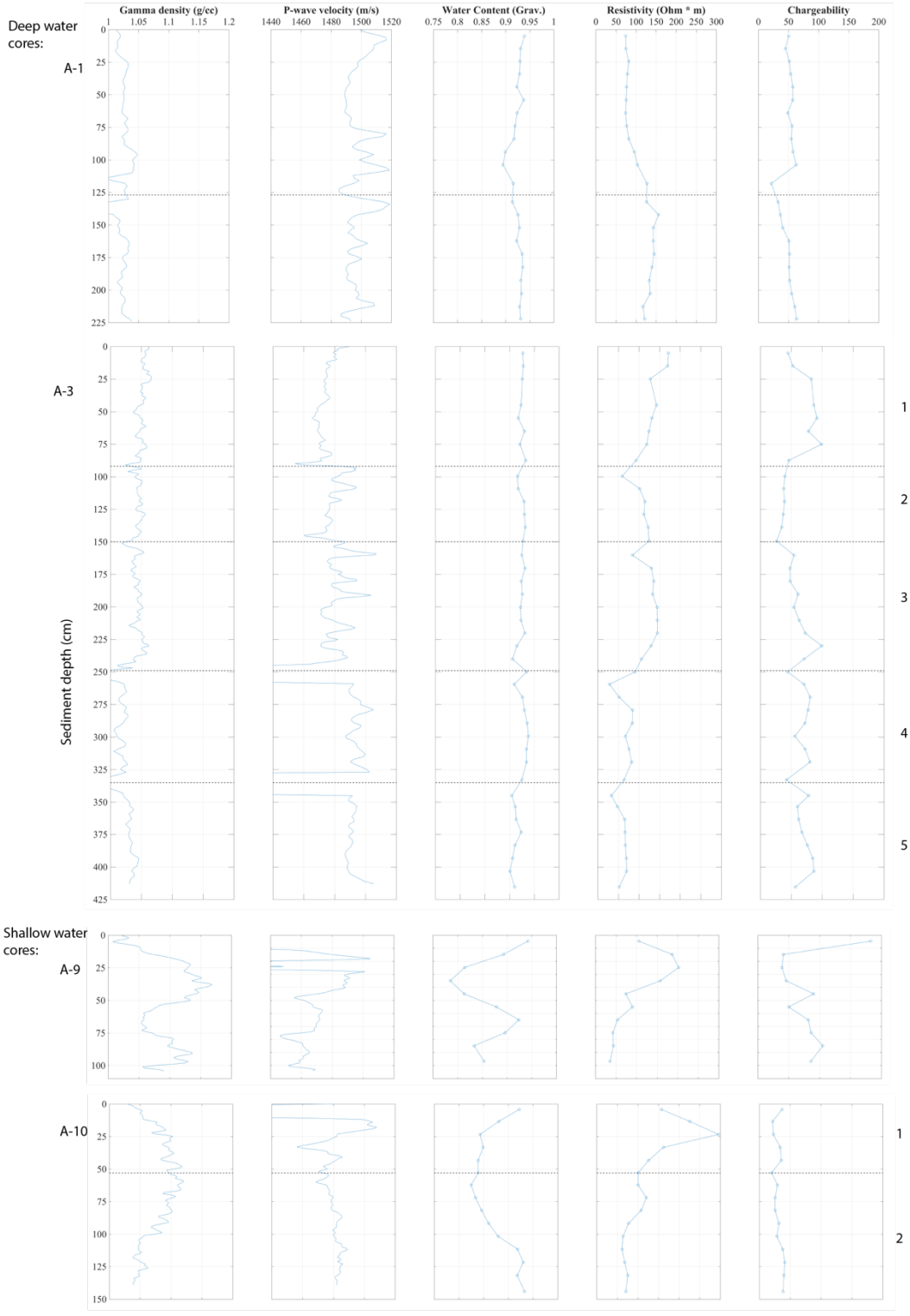
Gamma density (g/cc)
P-wave velocity (m/s)
Water Content (Grav.)
Resistivity (Ohm * m)
Chargeability
Deep water cores:
A-1
A-3
Sediment depth (cm)
1
2
3
4
5
Shallow water cores:
A-9
A-10
1
2

Figure 4.9 Physical properties of core A-1, A-3, A-9, and A-10., Grassy Pond, Eastern Newfoundland. The dashed lines are the boundaries between the core sections. The numbers on the right are the core section numbers. The gamma density and P-wave velocity are measured by MSCL scanning with a sampling interval of 2cm for the entire A-1 and the section 4 & 5 of A-3, which the sampling interval for the rest of cores is 1 cm. With the same sampling interval of about 10 cm, the water content is measured by weighting the sediments before and after drying out, and the resistivity and chargeability are measured by the SCIP tester. All the graphs show the original data. The gamma density and P-wave velocity near the section boundaries of A-1 and A-3 are beyond the axis due to the air gap/bubbles caused by water loss.

4.2.3 Radiocarbon Dating & Carbon Analysis

Age determination was performed to establish the proper chronology. Accelerator Mass Spectrometry (AMS) radiocarbon (C^{14}) dating is the down-core age-depth determination method used for the cores captured in Grassy Pond. It is a widely used and accurate radiometric dating method for organic-rich bulk sediments. The bulk sediment samples used for the radiocarbon dating include 6 samples from core A-3, 3 samples from core A-1 and 1 sample from A-10 (Table 4.3) (Figure 4.10). As the radiocarbon age is not the age in the calendar years, the calibration software OxCal v4.2.4 (Ramsey, 2009) is used to convert the radiocarbon years to calendar years. In Table 4.4, the 1 sigma represents the calibrated range (with a median number). Bulk carbon analysis was also performed for the radiocarbon dated samples by using an Elemental Analyzer (EA), which can enable estimation of the total carbon budget of the pond.

Table 4.4 Radiocarbon dates,carbon content and isotopic ratios obtained from the cores captured in Grassy Pond. The radiocarbon calibration was performed using OxCal v4.2.4 (Ramsey, 2009). BP = AD 1950.

Lab#	Core#	Material	Depth (cm)	%C	ð^{13}C	^{14}C yr BP	Calibrated Age	
							Median (BP)	1 sigma (BP)
UOC-2857	A-10	Bulk Sediments	151	16.079	-24.82	6325±28	7257	7313-7173
UOC-2858	A-1	Bulk Sediments	15	14.454	-25.39	1554±22	1469	1524-1393
UOC-2859	A-1	Bulk Sediments	126	16.265	-25.79	2801±23	2903	2960-2849

UOC-2860	A-1	Bulk Sediments	220	19.317	-26.56	4374±29	4929	4980-4858
UOC-2861	A-3	Bulk Sediments	15	16.086	-26.69	1223±22	1147	1187-1067
UOC-2862	A-3	Bulk Sediments	93	17.219	-26.49	3155±23	3381	3446-3344
UOC-2863	A-3	Bulk Sediments	152	19.433	-26.69	4027±24	4479	4532-4424
UOC-2864	A-3	Bulk Sediments	251	20.436	-25.41	5483±29	6288	6319-6263
UOC-2865	A-3	Bulk Sediments	337	17.172	-25.92	6489±30	7394	7459-7324
UOC-2866	A-3	Bulk Sediments	417	17.523	-24.01	8602±44	9557	9677-9516

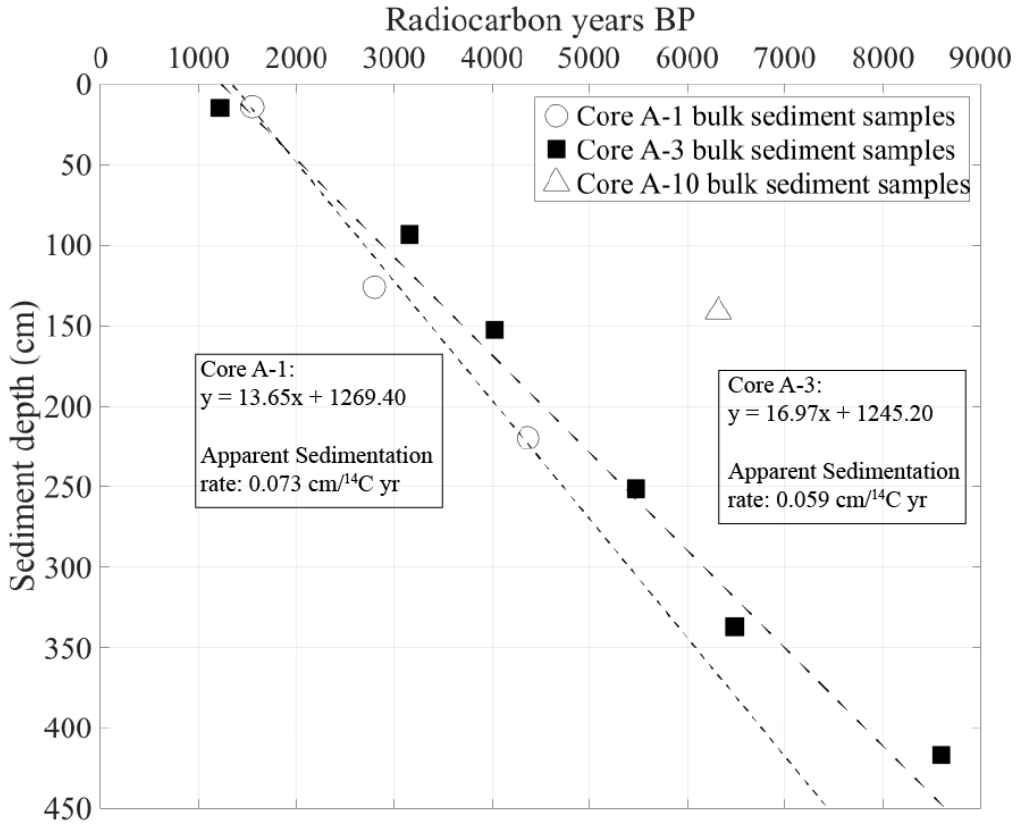

Figure 4.10 Radiocarbon dates of 10 bulk sediment samples from 4 cores collected in Grassy Pond.

The radiocarbon dates of the near-surface sediment samples (UOC-2858 and UOC-2861) for both cores are older than expected ages, which indicates the younger shallow sediments of the recent hundreds of years could be disturbed from a number of

external factors, such as anthropogenic activities in this area. It is possible that logging activities in the area resulted in old organic material from surrounding bogs being washed into the lake. Based on these radiocarbon dates and assuming a constant rate of supply, the calculated apparent sedimentation rate is approximately 0.073 cm/^{14}C Yr for core A-1 and 0.059 cm/^{14}C yr for core A-3.

The radiocarbon date of the basal sediment of Core-A-3 (UOC-2866) marks the age of the first post-glacial sediment of this lake basin generated about 8600 C^{14} Yr BP (9557 cal. Yr BP). Based on the radiometric dates from localities along the northeastern coast of Newfoundland, Scott, Mudie, Vilks, and Younger (1984) suggested that the ice on the northeastern Newfoundland had retreated into larger bays and to the present coastline by about 13000 years ago. However, the study of other sediment cores from the head of Trinity Bay and in ponds on the Bonavista headland suggest that the glaciation on land existed for another several thousand years (Wadleigh et al., 2002). Our radiocarbon date of the basal sediment of Grassy Pond (UOC-2866) at 8600 C^{14} Yr BP (9557 cal. Yr BP) is very close to the radiometric date of 8560 years ago at the basal sediment core (H-9) collected in Trinity Bay near the community of Clarenville in Wadleigh et al. (2002)'s study. Consequently, our radiocarbon date of the basal sediment in Core A-3 provides new evidence to the longer lasted deglaciation in the Trinity Bay area than elsewhere on the island.

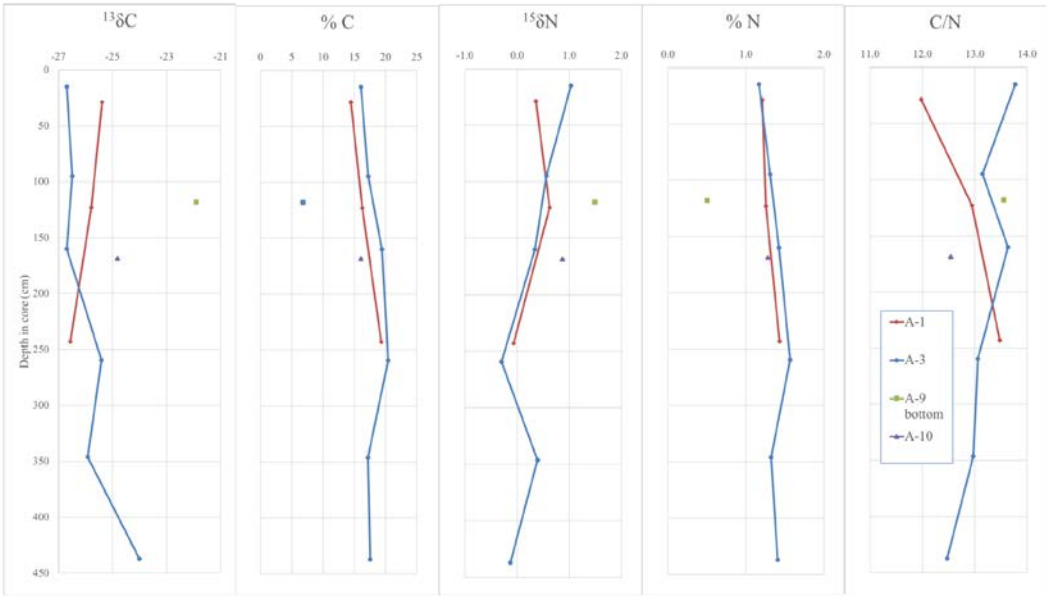

Figure 4.11 Carbon and Nitrogen abundances and isotopes in sediment core samples.

Figure 4.11 shows the isotopic analysis of selected samples from all four cores. The carbon concentrations of 15-20% by weight are very high for lake sediments in general, indicating an organic rich lake. The C/N ratios of 12-14, on the other hand, are low. Typical soil values are ~50 (S. Zeigler, pers. comm.) These low C/N ratios may indicate an algal source.

Not counting A-9 bottom, $\delta^{13}C$ is -24 to -26.5, in the range of land-based vegetation, in particular "C_3" plants (see Figure 4.12). The categories C_3, C_4 and CAM refer to the pathways for photosynthetic uptake of carbon. Vegetation, including algae, in temperate and high latitude regions is 'almost exclusively' C_3 while C_4 plants are more common in tropical regions and CAM plants in deserts (Clark & Fritz, 1997). Freshwater carbonates have higher $\delta^{13}C$ (Figure 4.12). The measured $\delta^{13}C$ values are consistent with the result from acid washing stage in the carbon dating, that there is no measureable

carbonate in the muds. This is reasonable also from the setting of the lake, since there are no carbonate rocks in the vicinity.

The $\delta^{15}N$ values in the deeper sediments are close to zero, indicating that the nitrogen was fixed from the atmosphere and that other sources of nitrogen were sparse.

There is a small but measurable change in the longest core, A-3, with $\delta^{13}C$ decreasing, $\delta^{15}N$ increasing and C/N increasing. These changes are consistent with a change in source with time, as macroscopic vegetation such as pond grass or watershed input from the land become more important relative to algae.

In the profiles, the sample at 255 cm depth often does not follow the general trend. This may be related to the fact that it is located at a significant change in the geochemistry of the sediments at ~5500 C^{14} Yr BP (6288 cal. Yr BP).

The outlier in the analyses is the sample from the bottom of core A-9, at the transition between glacial till and organic material. The bottom of A-9 is grey, clay-rich and layered, very different from other samples which are a softer, highly organic brown mud. Sample A-9(10) appears to contain a significant fraction of clay probably deposited as the glaciers retreated. The higher $\delta^{13}C$ may indicate a carbonate component or degradation of organic material (oxidation by microbes) in oxic conditions during transportation by glaciers (S. Zeigler, pers. comm.)

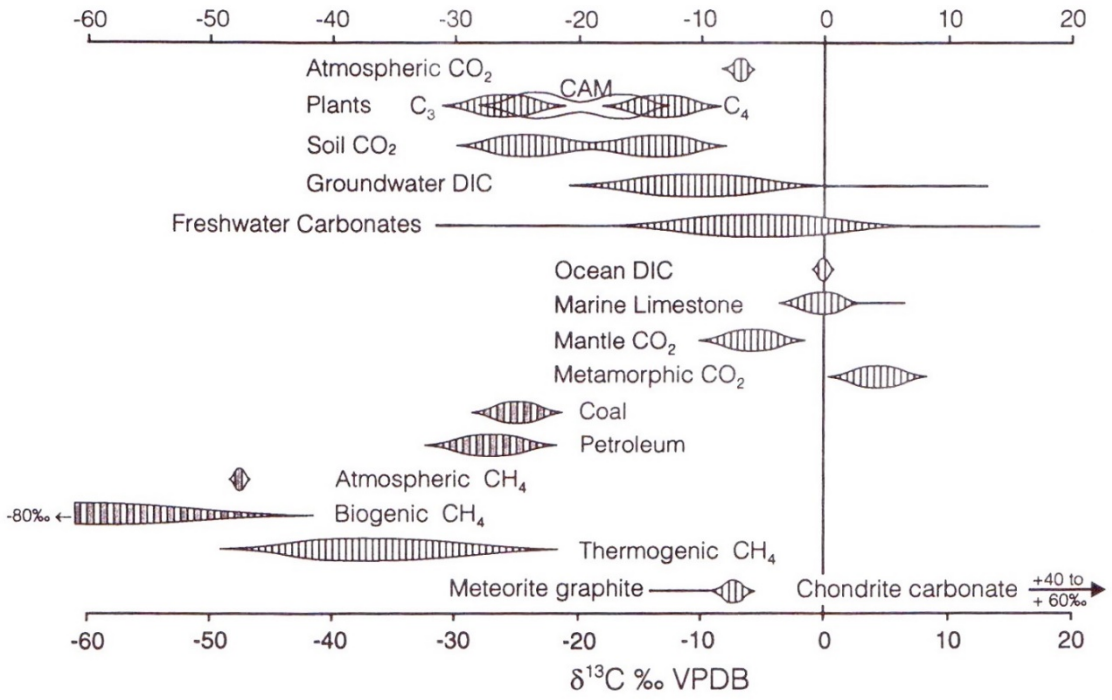

Figure 4.12 Ranges for $\delta^{13}C$ values in selected natural compounds (Clark & Fritz, 1997).

The carbon budget of Grassy Pond can be calculated using the sediment volume estimation from the basin analysis (Table 4.2). Based on the bulk carbon percentage analysis of selected samples in Core A-1 and Core A-3, an average carbon weight per cubic meter is calculated (Table 4.5). From the total sediment volume and the surface area of the pond, the total carbon budget and the carbon budget per square metre of Grassy Pond can be estimated (Table 4.6). The result shows that this fresh water lake in eastern Newfoundland with a surface area of 65,300 square metre contains about 1,886 tons of carbon. Compared to a well-drained upland forest with a 6-10 kg/ m^2 of carbon in the soil (Ziegler et al., 2017) and a boggy forest with more than twice that much (S. Ziegler, pers. Comm.), the about 29 carbon budget per square metre of Grassy Pond is significantly high.

Table 4.5 The calculation of the average carbon weight per cubic meters of the sediments in Grassy Pond.

Core #	diameter (m)	length (m)	volume (m^3)	Tot. dry weight (kg)	Ave. %C.	Tot. C. weight (kg)	C. weight per m^3 (kg)
A-1	0.0665	2.33	0.00809	0.615	17	0.104	12.9
A-3	0.0665	4.44	0.0154	1.133	18	0.204	13.2
						Average:	13.1

Table 4.6 The estimated carbon budget of Grassy Pond.

Surface area (m^2)	Sediment volume (m^3)	Carbon budget (kg)	Carbon budget per square metre (kg/m^2)
65,300	144,000	1,886,400	28.89

4.2.4 Inorganic bulk geochemistry

The main purpose of inorganic geochemical analysis is to test if any of major lithic elemental changes can be related to the down-core physical changes, such as in water content and density, in the hope that such correlations could contribute to the understanding of the sediment structures causing the GPR signal reflections.

In addition, we want to characterize the lake by its organic and lithic content, and to investigate the geochemical variation in the lake to see 1) if there are significant variations with depths and locations since random lake sediment samples are taken to identify mineral prospects; 2) if we could correlate stratification in different lake sub-basins to see whether they had a common history of sediment deposits; and 3) coupled with radiocarbon dating, whether they tell us anything about past climate variations.

The sub-sampled sediments were dried out and powdered after the water content,

DC resistivity and IP measurements were taken. These processed samples were sent to the Department of Natural Resources (DNR) of Newfoundland for bulk inorganic geochemistry analysis at the geochemistry laboratory operated by Christopher Finch. The geochemical analysis used inductively coupled plasma optical emission spectroscopy (ICP-OES) method for the dried samples taken over the same depth intervals as the physical properties (approximately 10 cm) for all four cores. The concentrations, given as the weight fraction of the dried samples, were measured for 28 elements (see Section 3.2.4). The silicon analysis is not available because all the silica in the dried sediment samples is removed by the four-acid digestion process for the ICP-OES method. The Loss on Ignition (LOI) analysis at 550 ºC was also performed on the dried sediment samples before the ICP-OPS analysis, and LOI is an indicator of the organic content in the sediments.

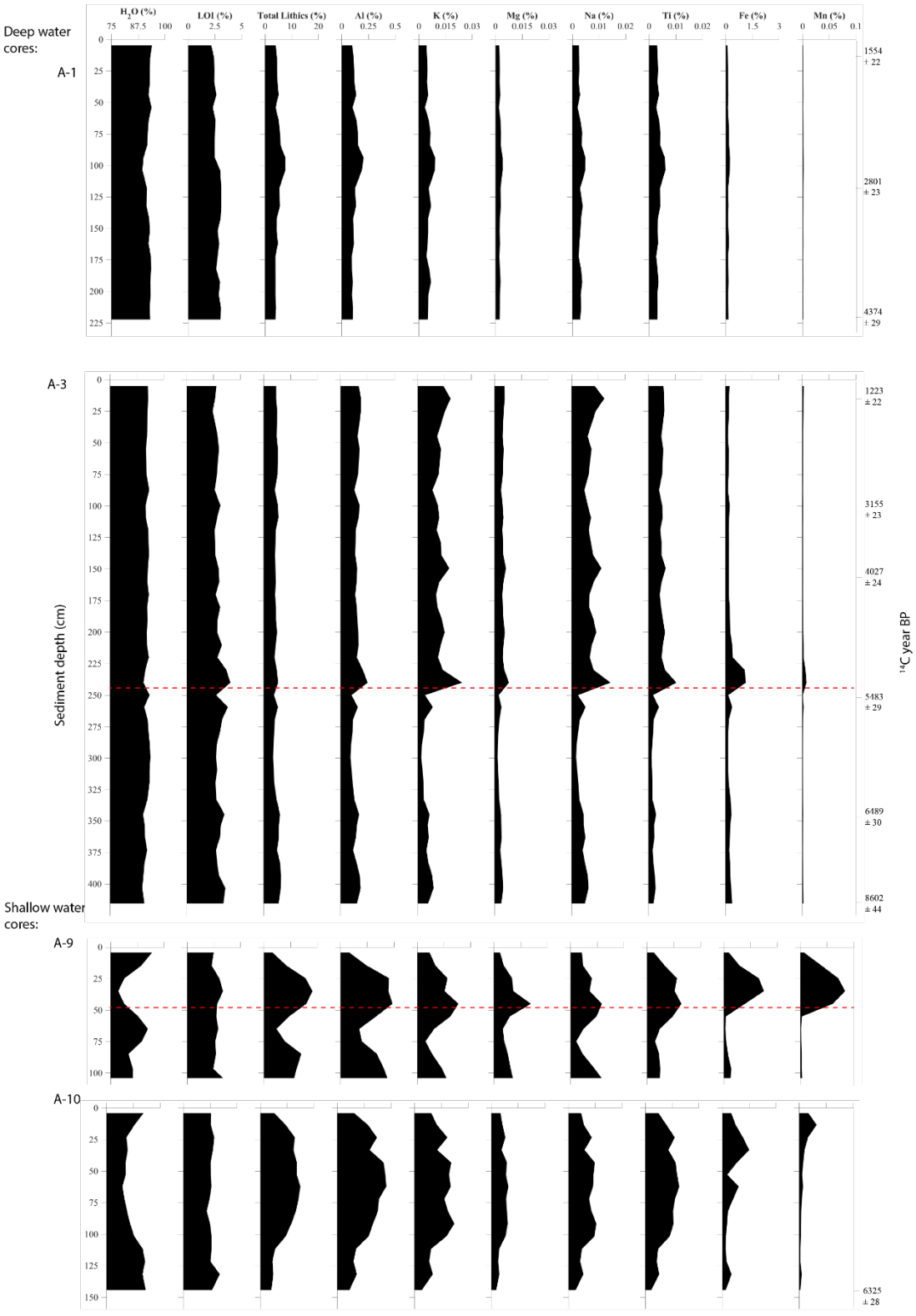
Deep water cores:
A-1
A-3
Shallow water cores:
A-9
A-10
Sediment depth (cm)
^{14}C year BP
H_2O (%)
LOI (%)
Total Lithics (%)
Al (%)
K (%)
Mg (%)
Na (%)
Ti (%)
Fe (%)
Mn (%)
1554 ± 22
2801 ± 23
4374 ± 29
1223 ± 22
3155 ± 23
4027 ± 24
5483 ± 29
6489 ± 30
8602 ± 44
6325 ± 28

Figure 4.13 Core geochemistry for all four cores collected in Grassy Pond, which includes water content, LOI, total lithic content, major detrital-related element (Al, K, Mg, Na, and Ti) concentration, and redox indicator elements (Fe and Mn) concentrations. The red dashed lines in core A-3 and A-9 show an anoxic-oxic interface, which is indicated by the sharp increase amount of Fe and Mn.

Figure 4.13 shows the water content, LOI, major detrital-related element (Al, K, Mg, Na, Ti) concentration as well as the redox indicator elements (Fe & Mn) variations as a function of depth. All these measurements are shown in the percentage of the original sediment samples, that is, of the wet mud.

For all cores, water dominates the material composition, comprising over 90% in the long cores and over 75% in the short cores. The water content varies significantly more in the short cores. LOI, the organic material indicator, takes about 2-4% of the whole sediments in all cores, and it does not vary significantly with depth. The "total lithics" are the rest of the materials in the sediments excluding water and organic, and they take about 4-8% in the deep cores and 3-16% in the deep cores. The major detrital-related elements only take a very small portion of the sample, and they show significant variations with depth in each core. The redox indicator (Fe & Mn) take a much smaller percentage in the deep cores than in the short cores.

The water content and lithic content, including each individual rock-forming element, show the greatest anti-correlation over all four cores. This is logical, since there is relatively little variation in the organic weight fraction in the sediment. LOI as a fraction of the dried sediment is generally correlated with the water content, which indicates that where there is more water, there are more organics relative to lithics.

Fe and Mn also generally follow the pattern of the detrital-related elements in the long cores; however, Fe and Mn do not follow the pattern of the detrital-related elements

in the short cores. Interestingly, two major concentration peaks of Fe and Mn in A-3 and A-9 can be associated with the lithic concentration peaks.

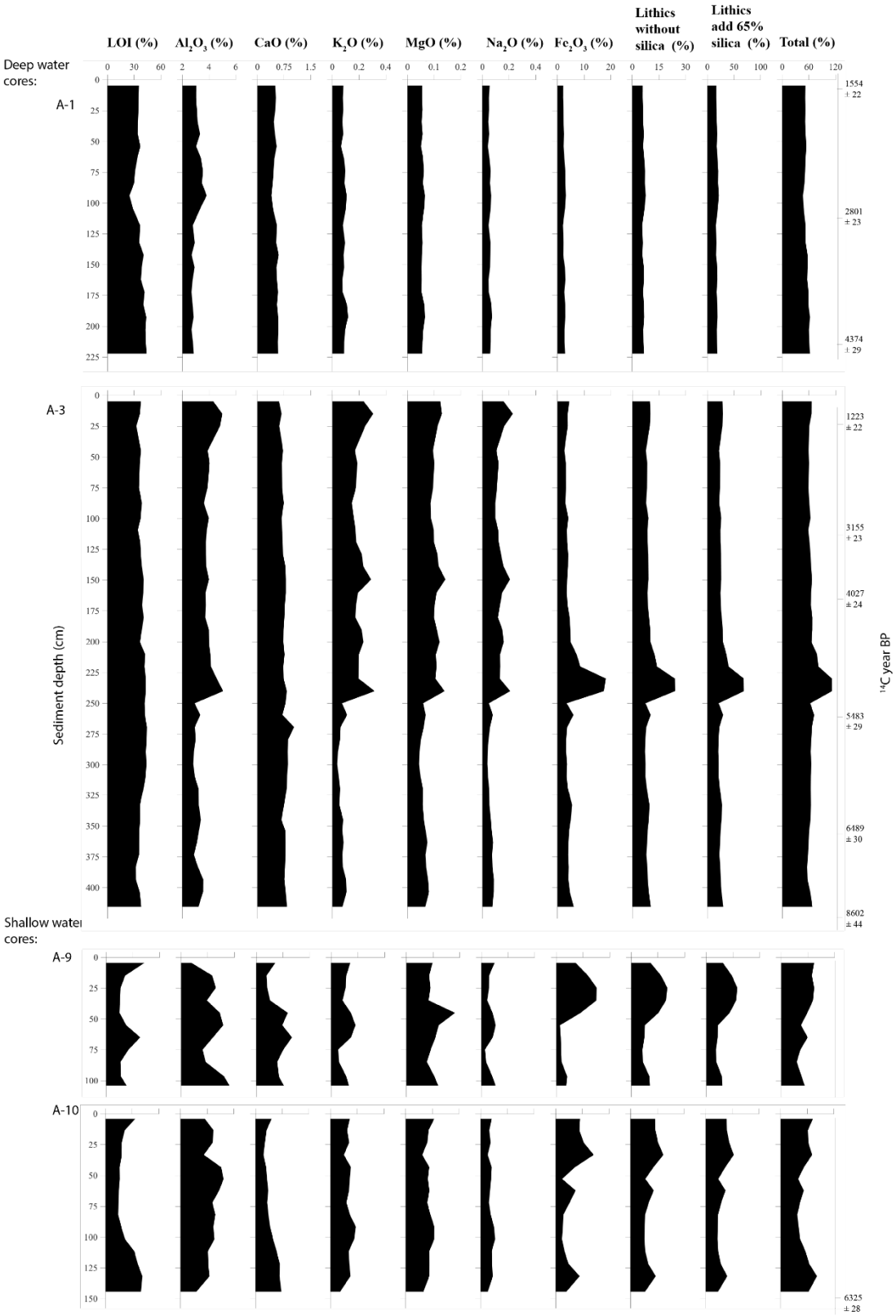
LOI (%)
Al2O3 (%)
CaO (%)
K2O (%)
MgO (%)
Na2O (%)
Fe2O3 (%)
Lithics without silica (%)
Lithics add 65% silica (%)
Total (%)
Deep water cores:
A-1
A-3
Sediment depth (cm)
Shallow water cores:
A-9
A-10
14C year BP
1554 ± 22
2801 ± 23
4374 ± 29
1223 ± 22
3155 ± 23
4027 ± 24
5483 ± 29
6489 ± 30
8602 ± 44
6325 ± 28

Figure 4.14 The composition analysis of the dried sediments over all four cores collected in Grassy Pond. The percentage of the rock-forming oxides are calculated based on their elemental concentrations. Since all the silica in the samples are eliminated from the acid digestion in the ICP-OES analysis, an estimated 65% silica (common silica content of sedimentary rocks) is added to the total lithic content. The "Total" is the summation of the organic content and the estimated lithic content.

We also analyzed the composition of the dried sediment samples by calculating the content of the oxides of major rock-forming elements (Al, Ca, K, Mg, Na, and Fe) (Figure 4.14). All of these concentrations are based on the dried sediment samples. Since silica in the dried samples is totally removed in the acid digestion, we also added 65% silica into the total lithic content. The "total" value is the summation of the organic content (LOI) and the lithic content (with silica added). Some interesting points can be made as follows.

The dried sediments are highly organic with the LOI between 20 and 40% by weight. Given that the density of organic material (about that of water) is much less than that of lithic material, the volume fraction of organic material is significantly higher (~40-60%). As seen in Figure 4.14, the LOI variations in the short sediment cores are more intense than in the deep sediment cores. The LOI in the dried sediment samples also shows a general anti-correlation to the detrital-related oxides, which is the opposite in the wet sediment samples (see Figure 4.13). The detrital-related elements (and oxides) in the dried sediments show the same pattern as they do in the wet sediments. Their variations with depth in the short cores are also more intense than in the deep cores. Generally, the "total" (organic + lithics) percentage, if we include silica associated with lithic elements at 65%, is in the range of 40 – 80%. It is assumed that the remainder is excess silica, since all silica is removed before the ICP OES analyses. This excess silica could be in the form

of diatoms. There is no excess of silica in the concentration peak at the 225-250 cm interval of core A-3, but the microscopic examination (Figure 4.15) shows there are plenty of diatoms, which suggests that, at least in this interval, the lithic elements are not all in the form of silicate minerals.

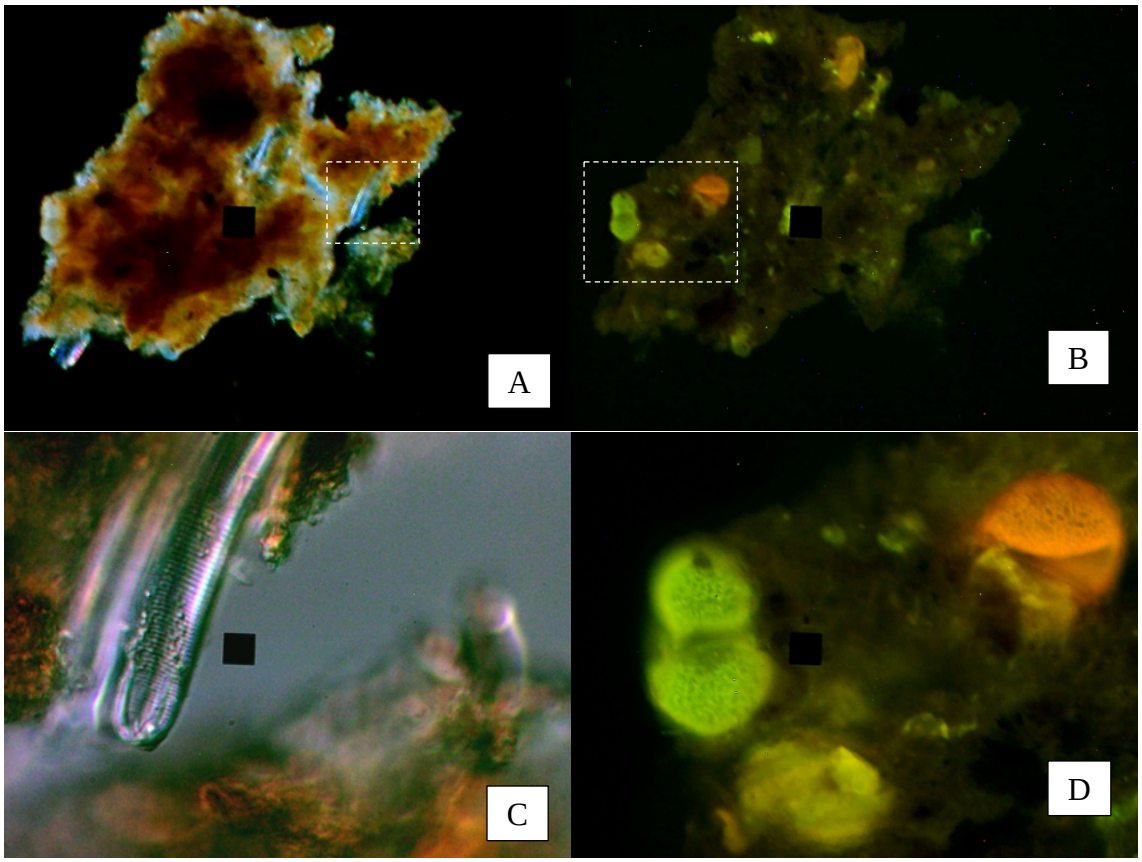

Figure 4.15 Microscopic analysis shows a particle of a dried sediment sample at the depth of 240 cm in core A-3. The high fraction of silica diatom shells relative to organic algae components in the sediments indicates that it is a low nutrient lake. A) In plain light under the microscope, the sediment is seen to be composed of brown organic material (e.g. dead algae, pollen grains) and clear cylindrical silica diatom exoskeletons. B) Under ultraviolet light, the organic material is shown to contain a large fraction of pollen grains, which fluoresce at these wavelengths. The black square in the centre of the images is 40 µm on the side. C) At higher magnification, the fine structure of one of the diatoms is revealed. Black square in the centre of the images is 5 µm on the side. D) The big bisaccate pollen grains are from Abies balsamea (Balsam Fir). Black square is 10 µm on the side.

Since the down-core variation of the detrital-related elements indicates the amount of the run-off from the weathering/erosion of surrounding rock source, it can reflect the dry/wet condition in history. For example, an increasing amount of the lithic elements at a certain depth of the core indicates a drier period at that time because drier conditions cause less vegetation in the surrounding area allowing more rock sources to be exposed, weathered and eroded. Fe and Mn are good indicators of redox conditions. For example, an increasing amount of Fe and Mn in the sediments indicates the transition from anoxic to oxic in the lake environment, which usually reflects the wet to dry period that lowers the lake water level. As the redox conditions of the lake environment are often related to the climate condition, the down-core trends of Fe and Mn can generally follow the pattern of the detrital-related elements; however, the redox condition in the thin sediment area (short cores) is more complex because it is more easily disturbed by multiple external factors than the redox condition in the deeper lake sub-basin areas.

Another very interesting feature in the core geochemical analysis is that the data of A-3 show a significant concentration peak for most major and minor elements between the down-core depth of 225 and 250 cm. In addition, the DC resistivity data also shows that the resistivity significantly decreases near this depth, which could be a result of the relative decrease in water content. Since many of the metal elements also have a concentration peak between this 225-250 cm interval, it is interesting to see if these metal elements come from other sources than the surrounding rocks.

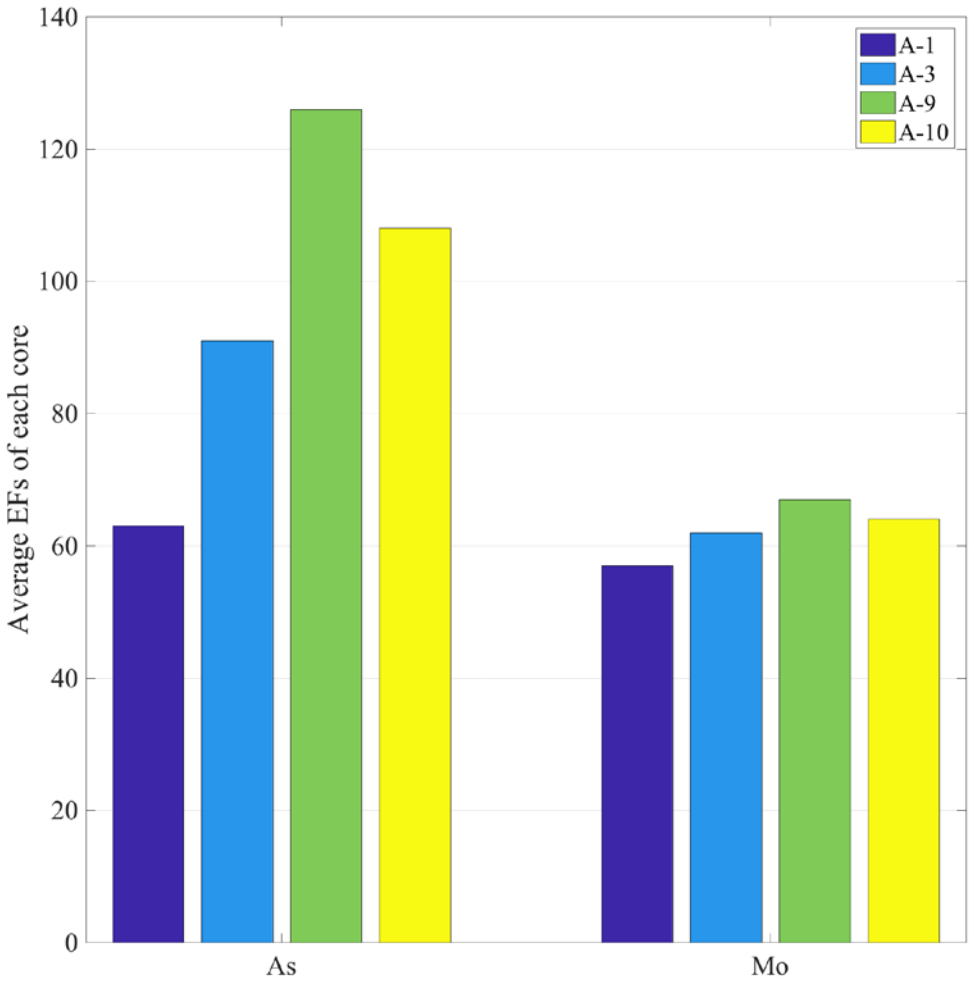

Figure 4.16 Average Enrichment Factors (EFs) of As and Mo for all four cores collected in Grassy Pond. The reference sediment is the alluvial sediments over the Post-Archean Australian shale (Kamber, Greig, & Collerson, 2005), that represents an average upper crustal value.

Enrichment factors (EFs) are commonly used as a means to identify and quantify human interference with global element cycles (Karageorgis, Katsanevakis, & Kaberi, 2009). In our case, EFs are used to assess: 1) how much these metal elements are enriched comparing to an average upper crustal value; 2) and how much these metal elements are enriched comparing to intra-core trends. The enrichment factors are calculated from:

$$EF = (element/Al)_{sample}/(element/Al)_{ref.sed.}$$

where the reference sediment is the alluvial sediments over the Post-Archean Australian shale (Kamber et al., 2005), because these sediments have not undergone diagenesis and lithification. Since Al is one of the most immobile element of typical detrital minerals, it is used to eliminate the geochemical enrichment factors from local rock sources. The average EFs of all the four cores show As and Mo are particularly enriched in our sediment samples comparing to the reference sediments (Figure 4.16), while the EFs of other metal elements are very close to the normal upper crustal values. Even though arsenic has the highest enrichment variation across all core, the EFs variations for As and Mo have the same trends in all four cores. The EFs of As and Mo in the short cores (A-9 & A-10) is higher than in the long cores (A-1 & A-3).

The EFs can also be normalized to their minimum values within the core to emphasize the intra-core trends. Figure 4.17 shows the normalized EFs for Fe, Mn, As, and Mo in core A-3. Mineralization indicators As & Mo show very similar patterns, while the patterns for the oxidation indicators vary somewhat from them and from each other. All these elements show a common concentration peak at the 225-250 cm interval. Fe and Mn are very redox-sensitive and they can be an indicator of the redox condition at the certain depth of the core. Diagenetic processes such as oxidation of organic matter, dissolution of Fe and Mn oxides under reducing conditions and reprecipitation when oxic conditions are reestablished can affect the geochemical behaviour of many redox-sensitive elements (Calvert & Pedersen, 1993; Karageorgis et al., 2009; Mahler, Van Metre, & Callender, 2006). Since As and Mo are both redox-sensitive elements, their

down-core EFs can be significantly affected by Fe and Mn.

Grassy Pond lies within the Big Easy Prospect that is surrounded by late Neoproterozoic arc related volcanic and volcanoclastic rocks, some of which underwent low-sulphidation epithermal alteration leading to gold mineralization (Wall, 2017). Thus, the enrichment of As and Mo can be related to the erosion of iron oxide minerals in the surrounding alteration zone of this epithermal style gold-silver system.

All these elements show a common concentration peak near 5k radiocarbon years ago (6.3k calendar years ago) when the regional climate started to become drier (Wadleigh et al., 2002), and more prone to fires. The pond may have been shallower and erosion rates of the surrounding mineralized zone increased at that time.

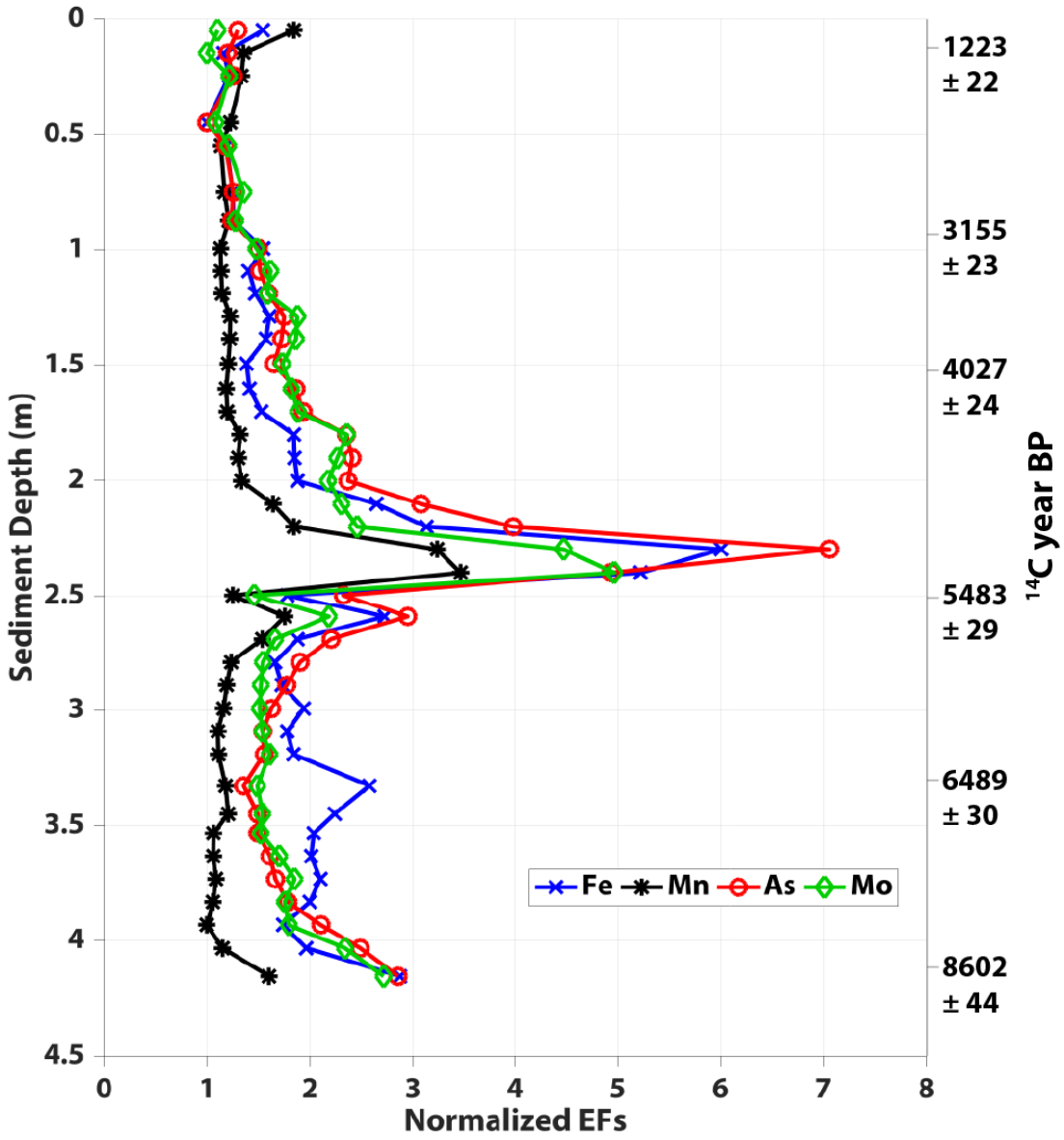

Figure 4.17 Core-A-3: Depth profile of enrichment factors for redox-sensitive elements: Fe, Mn, As, and Mo showing a common concentration peak in the interval of 225-250 cm (about 5k radiocarbon years ago). Normalization is with respect to the lowest concentration in the core, therefore the minimum value for all the profiles is 1.

4.3 Lake Sediment Structure Modelling

Lake sediment structure modelling is the final component in this project. The

purpose of the modelling is two-fold: 1) to examine the hypothesis that the water content variations cause the layered structures within the lake sediments in the GPR profiles; and 2) to build some simple synthetic lake sediment structures and simulate the GPR signal responses to gain a deeper understanding of the nature of GPR signals in the freshwater lake environment.

In order to achieve these goals, we first developed an algorithm (Eq. 3.2) to produce synthetic 1-D GPR traces by convolving the GPR source wavelet with the reflection coefficients (see Section 3.3.1 and Figure 3.15). The synthetic 1-D GPR traces are evaluated by comparing with the actual traces from the GPR profiles collected in Grassy Pond. Then, we use the same algorithm to model the GPR responses under different sediment structures by inputting different physical properties of lake sediments.

Since the modelling algorithm is simply the convolution of a source wavelet and a series of reflection coefficients, it is essential to establish the correct physical properties for calculating the reflection coefficients. The GPR source wavelet used is the Berlage wavelet, which is introduced by Aldridge (1990) and since then has been successfully applied to GPR modelling applications as an idealised GPR source wavelet. However, the reflection coefficients cannot be directly obtained from the data, and they have to be inferred from other properties such as EM impedance. Thus, one of the most important steps of the forward modelling is to determine the appropriate physical properties of the core in order to find the reflection coefficients.

Since the reflection coefficient series can be derived from the contrast in EM impedance (Eq. 3.20) and the EM impedance can be calculated from the apparent dielectric constant (Eq. 3.19) (A. Annan, 2009), the determination of the apparent

dielectric constant is critical for the modelling process. Topp et al. (1980) established an empirical relationship between the apparent dielectric constant and volumetric water content (Eq. 3.17), and Weber et al. (1997) have provided a means of calculating both volumetric and gravitational water contents from the bulk wet density if the grain density is estimated (E.q. 3.16 a&b). Thus, the initial work in the forward modelling is to estimate the grain density ρ_g of the sediment core and verify the relationship between the wet bulk density ρ_B measured by the MSCL and water content.

Although the grain density ρ_g of the sediment is not directly measured, an estimated value of 2.65 g/cc is used to calculate the gravitational water content in Eq. 3.16b. Figure 4.18 shows the comparison between the gravitational water content calculated from the MSCL data and the water content measured in the lab from the cut up sections for all four cores. The resolution for the calculated water content data is the sampling interval of MSCL for the gamma density logging as 1 or 2 cm, and the resolution for the calculated water content data is about 10 cm. The dashed lines are the boundaries of each section of cores. The data shows the calculated water content and the measured water content agree with each other for core A-9, A-10, and the first three sections of A-3. However, the calculated water content for core A-1 and the last two sections of A-3 shows a significant difference from the measured water content. The recorded gamma densities were about 0.02 g/cc lower than expected. These core sections were scanned on the same day, earlier than the other core sections, and the discrepancy is attributed to an error in the instrument calibration. Although there is an offset between the calculated and measured water contents for core A-1 and the last two sections of core A-3, the down-core trends of these two datasets show agreement. Apart from these

sections, the calculated water content from density logs match the measured water content.

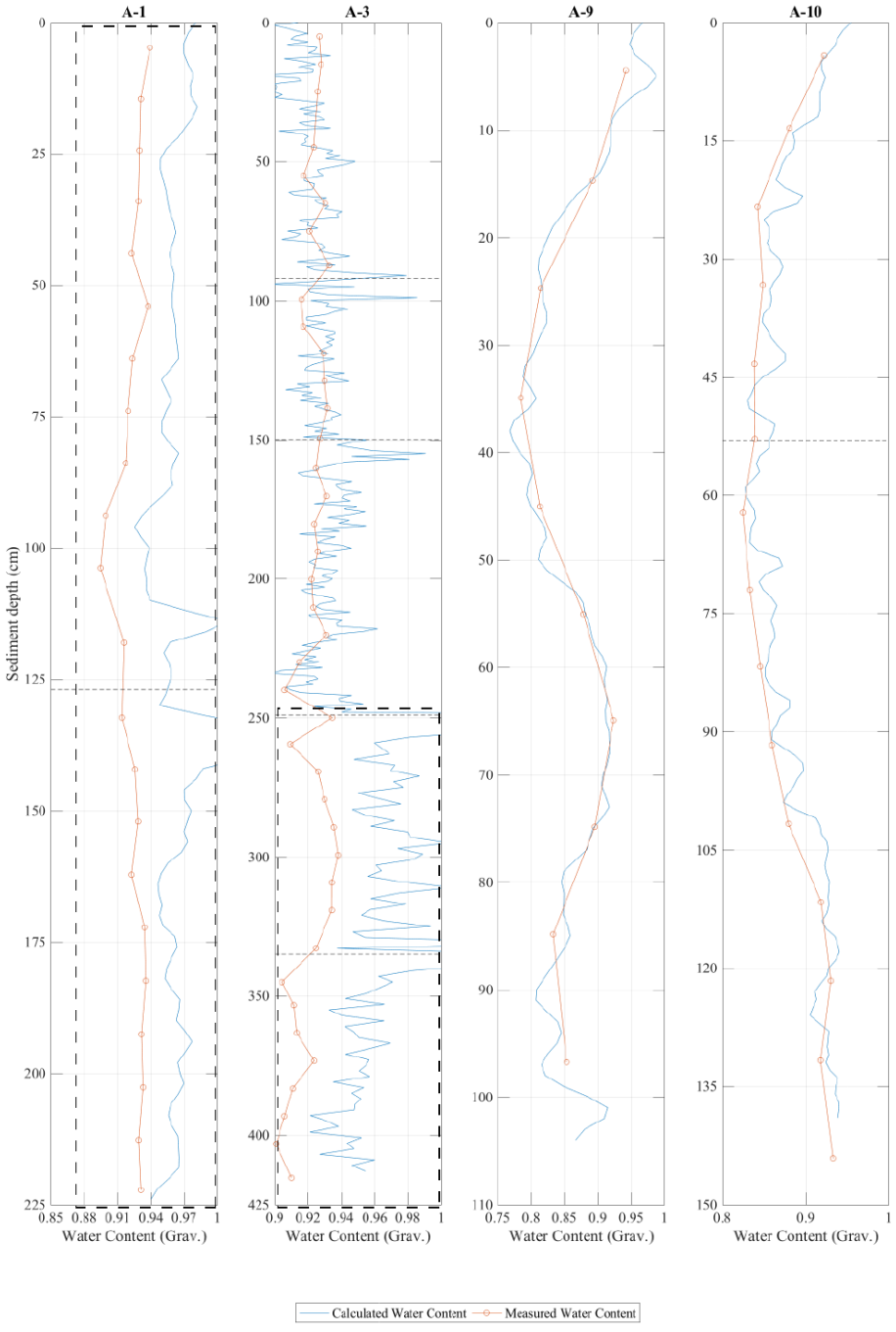

Figure 4.18 The evaluation of the calculated water content by comparing with the measured water content for all 4 cores. The calculated water content is based on the density log of MSCL with a resolution of 1 or 2 cm, and the measured water content has a resolution of about 10 cm.

The dashed line is the boundary of the sub-sections of certain cores. There might be some anomalies near the section boundaries due to the water loss or accumulation. The calculated water content in the dashed rectangles in A-1 and the last two sections of A-3 doesn't match the measured water content due to the calibration issues when they were logged by the MSCL.

Since the GPR profiles (Figure 4.8) show significant reflections at over the length of core A-1 and the top half of A-3, the density logs for these two cores can be used for modelling the GPR responses and comparing them to the actual GPR traces. However, the density logs for core A-1 are considered to be unreliable (figure 4.18). Therefore, only the density logs of the first three sections of A-3 (0-2.5m) are used for the forward modelling. In order to simulate the GPR response at the water-sediment boundary, the model includes 1 m fresh water layer with a density of 1 g/cc overlying the density log of the core.

Figure 4.19 shows the calculated physical properties starting from the gamma density log and finishing with the reflection coefficient log. The lengths of these physical properties are 3.5 meter, including a 1 m water layer and a 2.5 m sediment layer. The resolution of these datasets is 1 cm.

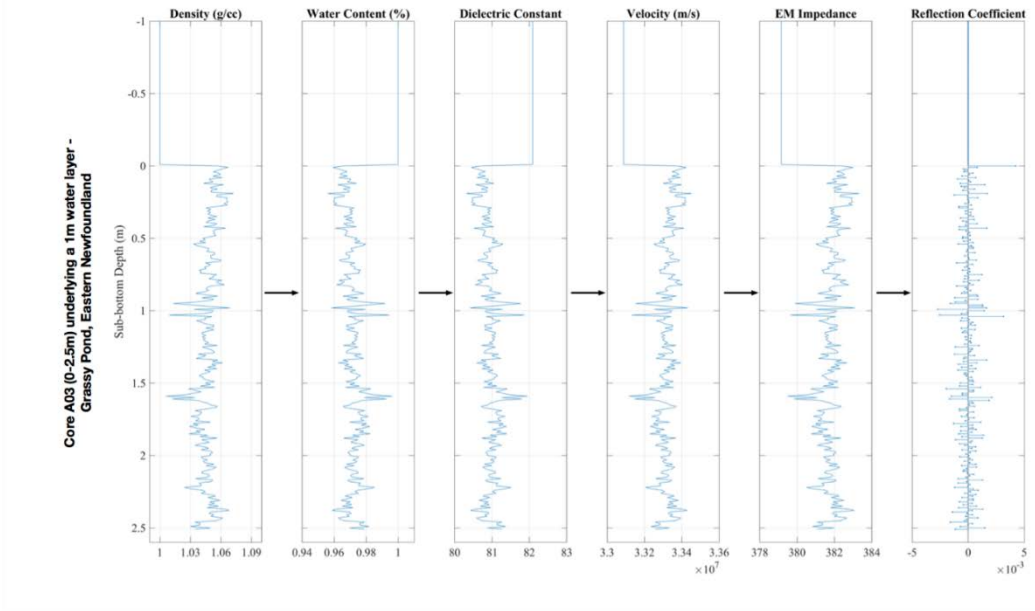

Figure 4.19 The calculated physical properties, including water content, dielectric constant, EM velocity, EM impedance, and reflection coefficient, based on the MSCL density log for the first 2.5m of core A-3. In order to simulate the water-sediment boundary, the first 1m of the density log is set to 1 g/cc since the MSCL density log only contains the density data of the sediments.

Since the calculated reflection coefficient series is found as a function of depth, it must be resampled as a function of two-way travel time before convolving with the source wavelet. The time log is created by dividing the depth log by the velocity log (Eq. 3.21), and the sampling interval is set as 0.8 ns, which is the same as the actual sampling interval of the GPR device creating the profiles. Then, the reflection coefficient series is resampled in time using the interpolation method. Finally, the resampled reflection coefficient series is convolved with the source wavelet to generate the synthetic GPR trace. Figure 4.20 shows the resampled reflection coefficient series and the generated synthetic GPR trace comparing with the actual traces taken from GPR profiles A-3X and A-3Y. The amplitudes for all these 4 profiles are normalized. The reflection starts at the water-sediment boundary that is located at 60 ns. The actual GPR traces in Figure 4.19

are taken from the average 10 traces centered on the core location of A-3 in the GPR profiles A-3X and A-3Y. The amplitude of the actual traces of A-3X and A-3Y starts to attenuate at time 150 ns. However, for simplicity the attenuation factor is not added to the model. The result show very good agreement between the reflection patterns of the synthetic trace and two actual traces between 60 and 150 ns. Although the actual trace amplitude is attenuated after 150 ns, there is a strong reflection at 170 ns existing in all three trace profiles. Consequently, the synthetic GPR trace well matches the actual GPR traces taken from the profiles, and it indicates the modelling method is successful.

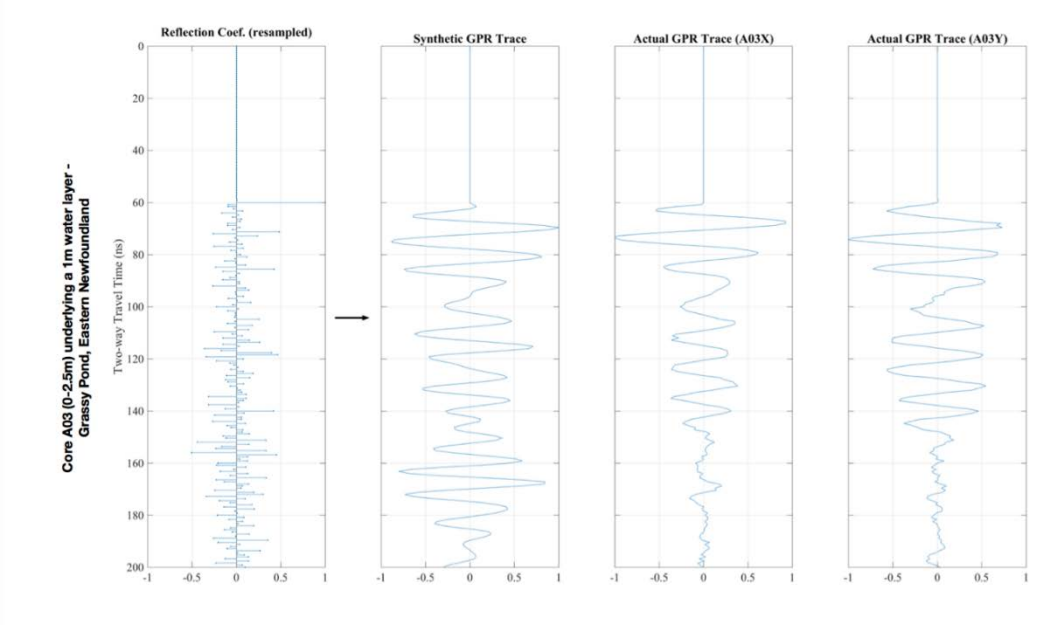

Figure 4.20 The comparison between the simulated 1-D GPR trace based on the resampled reflection coefficient and the actual GPR traces taken from the average of 10 traces centered on the coring locations of GPR profiles A-3X and A-3Y. Both the synthetic trace and the actual traces include the 1m water layer as the first 0-60 ns. The actual traces show attenuations starting from 150 ns, but the synthetic trace does not take account of the attenuation factor.

Chapter 5 Summary

The main objective of this project is to correlate reflections seen within lake sediments in GPR sub-bottom profiles with the physical properties of the sediments obtained from coring. Secondary objectives are: to estimate the carbon content of a typical small inland water body to help assess how such bodies contribute to the carbon budget; and to study the nature of geochemical variability within the lake, given that single spot sediment samples, which may not be representative, are used to assess the mineral prospective of an area.

In the early stage of this project, we used two different geophysical surveying methods, GPR and sonar, to approach lake basin analysis for two small freshwater ponds: Tippings Pond located near the community of Corner Brook in Western Newfoundland, and Grassy Pond near Thorburn Lake about 25 km from the community of Clarenville in Eastern Newfoundland. For the purpose of lake bottom bathymetric data acquisition, both methods performed well in their individual cases. However, each of these methods has critical restrictions depending on the field conditions. For example, the GPR signal is very sensitive to the conductivity of the pond water, because conductivity in a water body can result in significant signal attenuation. Our results show that the GPR signal is not able to penetrate deeper than a few meters below the water surface on Tippings Pond, even though it is considered to be a freshwater pond, while salinity is not an issue for sonar and penetration depths even in fresh water are generally significantly higher (compare Figures 4.1b and 4.2).

Another important consideration in choosing the survey method is the weather

conditions during the survey time. In Newfoundland, lakes are usually frozen during the winter, and GPR can provide a very convenient way to perform lake bottom profiling operating on the lake ice surface whereas sonar surveys require open water. On the other hand, for a summer survey, it is easier to operate sonar than GPR from a boat.

In this study, the great advantage of GPR in the very fresh water and water-rich sediments of Grassy Pond, was that it was able to detect previously unreported structures within the sediments (e.g., Figure 4.1a). The sonar data from Tippings Pond showed no such structure (Figure 4.1b).

Processing of the GPR dataset was carried out using the software "EKKO_Project 3" by Sensors and Software. Only basic processing techniques, such as "Dewow" filtering, a proper time gain, and a case-dependent spatial filtering were applied as advanced data processing was unnecessary.

Reflections from the top and bottom of the soft sediments are obvious in our GPR profiles except where the signal is attenuated in the deepest areas of this pond. Some profiles contain hyperbolas at the bottom interface. These hyperbolas are a result of EM wave diffraction caused by point reflectors, which are probably drop stones or till cobbles from the glacial activity lying on top of bedrock. We used these hyperbolas to calculate an average radar velocity of 0.035 m/ns from the top of the ice surface to the bedrock interface. Two of four acquired sediment cores reached the bottom of the sediments, providing known depths and allowing verification of the calculated average radar velocity.

The mapping of the bathymetry and depth-to-bedrock of Grassy Pond provided a useful guide for sediment coring locations. I developed programs for mapping the 3-D (UTME, UTMN, and depth) geographic information for the water-sediment and sediment-bedrock interfaces in "Matlab" by Mathworks (see codes in the Appendix) (see Figure 4.5). The maps show small depositional centres within an otherwise shallow pond. A sediment thickness map was created by differencing the bathymetric map and depth-to-bedrock map (see Figure 4.6). Generally, the bathymetry follows bedrock depths, but sediment thickness is not consistently related to water depth.

The most interesting feature from our GPR profiles is the laminated reflections

within the sediments. These laminations observed in the sediments follow the underlying bedrock shapes in the GPR profiles, so they are considered as records of natural sedimentation as times goes by. However, the mechanism that caused these internal sediment structures is still unknown upon this time. One of the most important goals of this study is to determine what change in physical properties produced these layered GPR reflections in the lake sediments. Sediment coring is the most direct way to approach this subject. Using the 3-D bathymetric and sediment distribution maps as guides, we collected 2 long cores in the centre of the lake sub-basin areas and 2 shorter cores in the areas between the sub-basins.

Visual inspection of the cores showed them to be mostly featureless, dark brown, highly organic sediment material without any visible laminations. Thus, there was a need for further investigation to link the physical properties of these cores to the laminations seen in the GPR data. We used a multi-sensor core logger (MSCL) to scan the cores without breaking them and obtained density and P-wave velocity along the cores with a resolution of 1 cm. We also sub-sampled these cores at an interval of about 10 cm and measured the water content, resistivity and chargeability. The data show that the density of the sediments is close to that of water, and water content measurements confirm that the water content is more than 90% by weight in the long cores and mostly more than 80% in the short cores. For the more water-rich long cores from the sub-basins the P-waves seem to be affected by bubbles and possibly anisotropy and the correlation with the density log is poor. In general, more analytical issues were encountered for the water-rich cores.

We performed some geochemical analysis, including LOI and ICP-OES, on all of

our dried sediment samples. Coupled with the physical properties, the geochemical analysis helped with the interpretation of the layer variations in the sediments. The LOI analysis indicates the lake sediments are highly organic. As a weight fraction, the organic content of the muds is 2-4%. Since the density of the organic content is not much greater than water (about 1.2 g/cc, E. Burden, pers. comm.), the elemental concentrations of typical detrital-related elements (e.g. Al, K, Mg, Na, and Ti) show a general anti-correlation to the water content. Since the concentration of the lithic elements are indicators of the erosion rate of surrounding bedrocks, it can reflect past climate conditions. For example, the increase of the lithic elemental concentrations in the lake sediments suggests a drier climate at that time because a drier climate would be associated with less vegetation, more fires and hence greater erosion of the surrounding land. The water level in the lake may also have been lower.

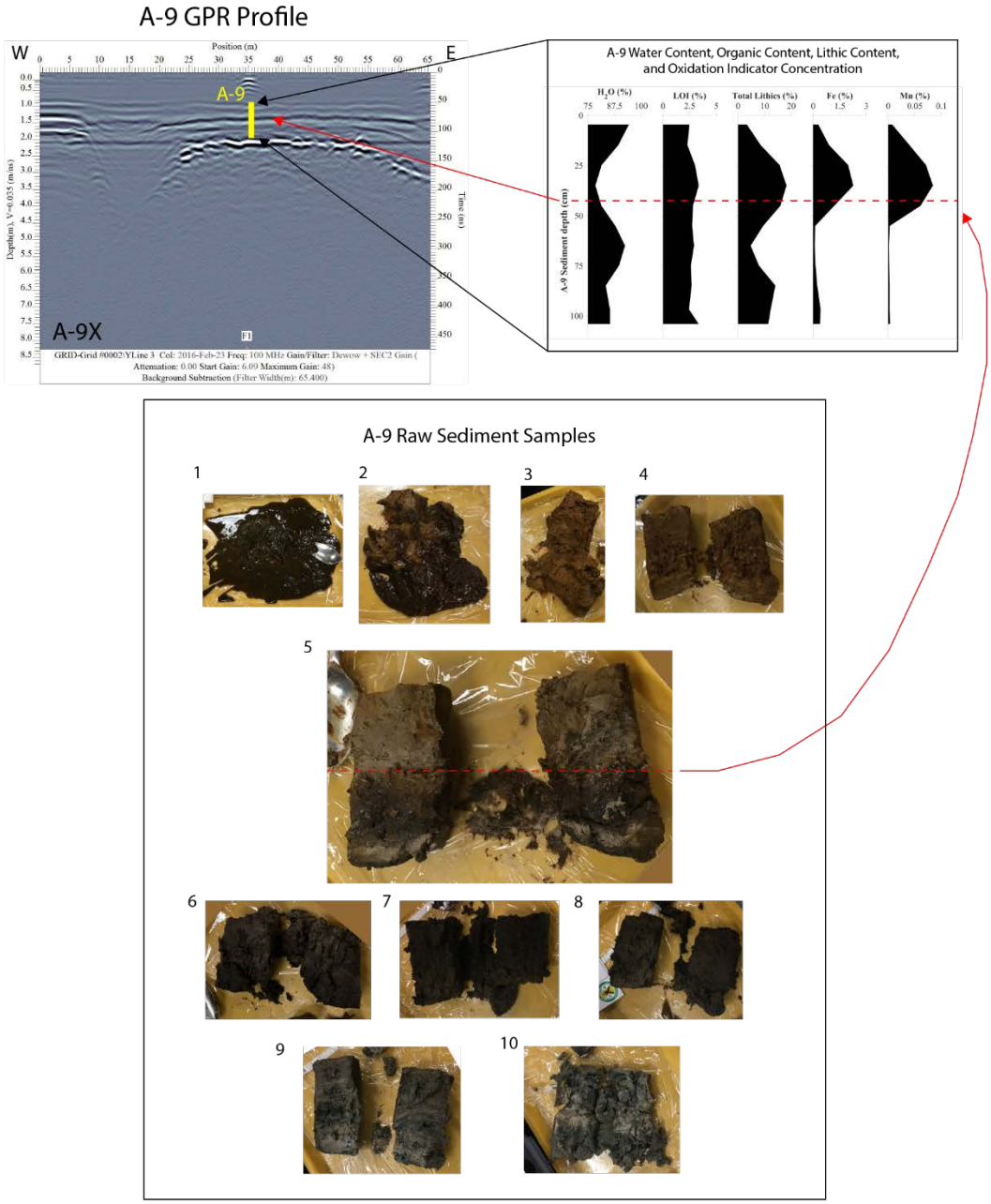

Figure 5.1 Core A-9: the correlation between the GPR reflections and the physical & geochemical properties. The raw sediment samples are subsampled about every 10 cm from the sediment core. The strong polarity-reversed GPR reflection in the middle of core A-9 is caused by the sharp downwards water content increase (water-rich layer), and this reflection can be also correlated to the anoxic-oxic interface indicated by the downwards intense decrease of Fe&Mn concentration as well as the color change in the actual sediment samples.

Among all the four cores collected in Grassy Pond, Core A-9 shows the most intense variations not only in the physical properties but also in the elemental concentrations. Core A-9 in the GPR profile is also characterized by a strong polarity-reversed reflection in the middle of the core. Figure 5.1 shows a summary of the core A-9's GPR profile, some physical and geochemical properties, as well as photographs of the sediment samples. The cause of this strong GPR reflection in the middle of core A-9 is a sharp increase of the water content in the sediment (that is, a water-rich layer) starting from 35 cm in depth. This reflection can also be correlated with the oxic-anoxic interface, indicated by the sharp downwards decrease concentration of Fe & Mn as well as the color change in the sediment.

The core age determination is also a very important aspect of core analysis. We performed radiocarbon dating on selected sediment samples from our longest two cores. The radiocarbon dates combined with the geochemical analysis of Core A-3 agree well with Wadleigh et al. (2002)'s studies on the lacustrine and marine sediment cores in the same area suggesting that the time interval between about 5000 to 3000 ^{14}C years ago was a dry period. The radiocarbon date of the basal sediment of Core A-3 also adds new evidence that the deglaciation on the land of the Bonavista and Trinity Bay round area took longer than elsewhere on the island.

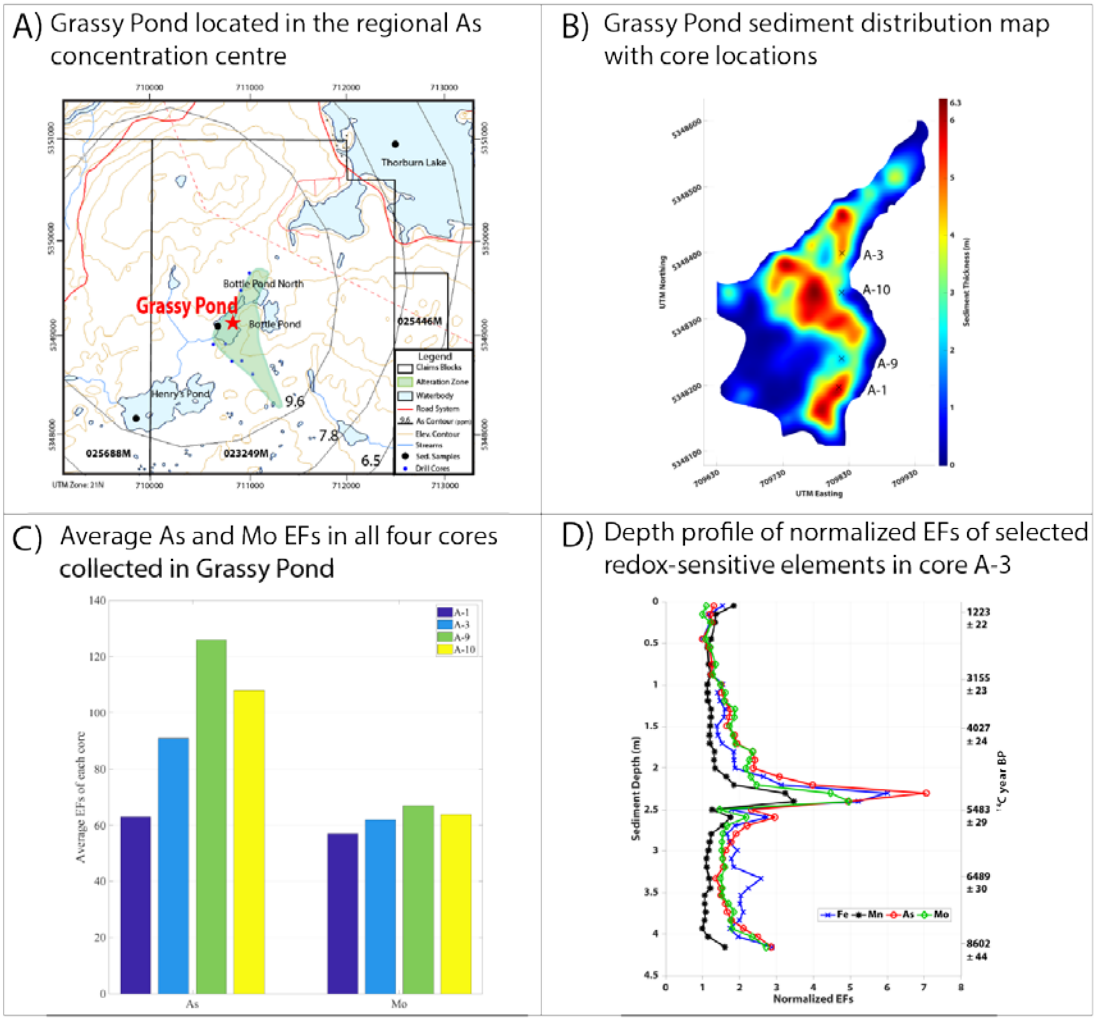

Figure 5.2 The arsenic (As) and molybdenum (Mo) are very enriched in the lake sediments of Grassy Pond, and their concentrations also vary with locations and depths in the lake. A) Grassy Pond located in the regional As concentration centre; B) Grassy Pond sediment distribution map with core locations; C) Average As and Mo enrichment factors (EFs) in all four cores collected in Grassy Pond; and D) Depth profile of normalized EFs of selected redox-sensitive elements in core A-3.

Another interesting finding from our sediment core geochemical analysis is that the arsenic (As) and molybdenum (Mo) are highly enriched in all four cores we collected in Grassy Pond comparing to the average crustal value (Figure 5.2). According to the lake sediment elemental concentration data from the Geological Survey of Newfoundland and

Labrador, Grassy Pond is located in a regional As concentration high (Department of Natural Resouces, 2018) (Figure 5.2A). Recent study also suggests that Grassy Pond overlies the alteration zone of a low-sulphidation epithermal style gold-silver system (Wall, 2017) (Figure 5.2A). Thus, the highly enriched As and Mo in the lake sediments of Grassy Pond are likely associated with the erosion of iron oxide minerals in the surrounding alteration zone of this epithermal style gold-silver system.

Although As and Mo are enriched everywhere, our study shows that the enrichment varies both in the location and with depth in the pond. Figure 5.3C shows that the enrichment factors (EFs) of As and Mo are higher in the short cores than in the longer cores located in the centre of the lake sub-basins (Figure 5.3B). Figure 5.3D shows that As & Mo have similar patterns as oxidation indicators Fe & Mn, and all these elements show a common concentration peak near 5k radiocarbon years ago when the regional climate started to become drier (Wadleigh et al., 2002), and more prone to fires. The pond may have been shallower and erosion rates of the surrounding mineralized zone increased at that time. Another possible reason for the spike in lithic input around that time could be related to failures of the beaver dam in Grassy Pond.

The reflection of GPR signals is very sensitive to dielectric constant changes. Since water has the highest dielectric constant among common geological materials, the GPR reflections could be controlled by the water content changes in the subsurface of a freshwater environment. Based on this hypothesis, we converted MSCL core density logs to water content logs by using the empirical relationship developed by Weber et al. (1997) assuming the grain density of 2.65 g/cc. We also measured the water contents by cutting the core into 10 cm intervals and weighing the wet and dry muds, and these

measurements agree well with the converted water content log. The water content logs were converted to EM impedance logs and re-sampled as reflection coefficient series for forward modelling for the purpose of simulating the GPR responses in order to match the radar trace records in the actual GPR profiles. In the forward modelling 1-D GPR traces were simulated by convolving the reflection coefficients and an idealized GPR source wavelet without considering attenuation factors.

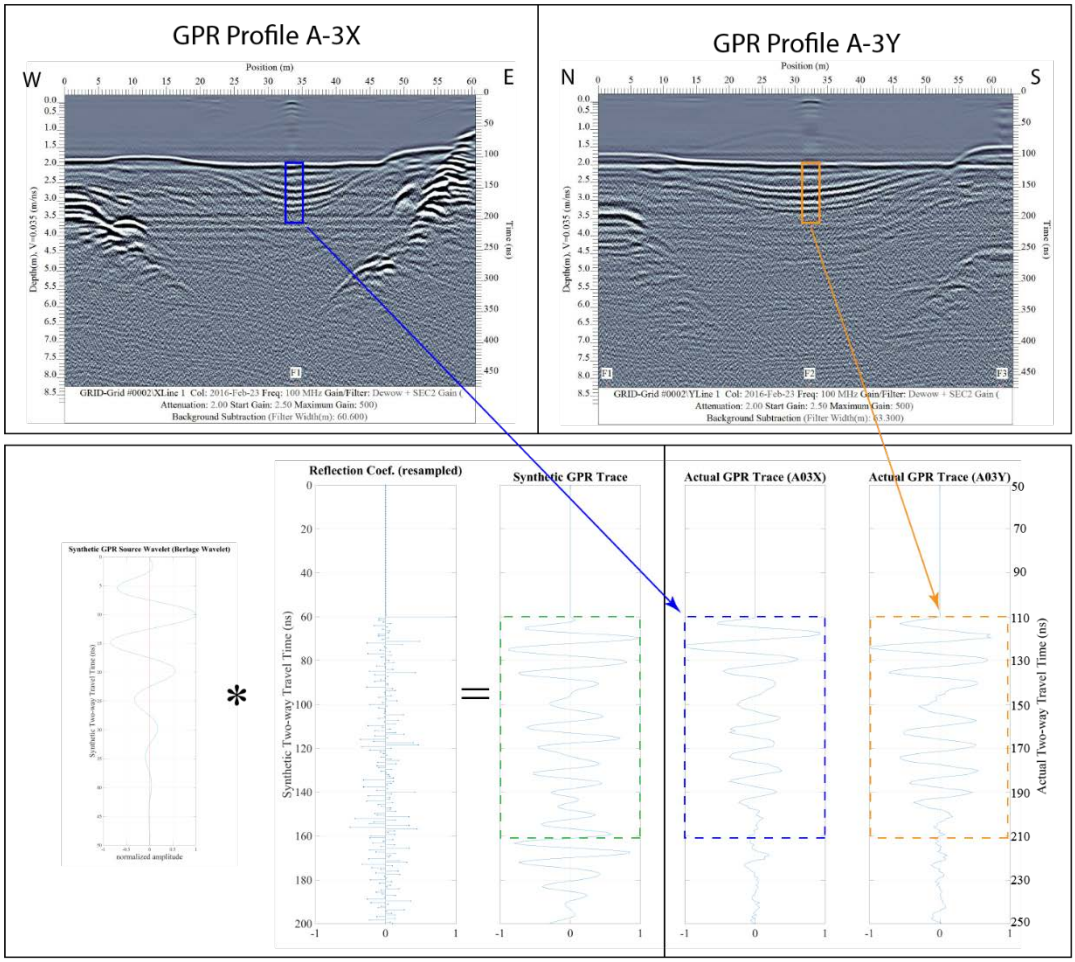

Figure 5.3 The comparison between the synthetic GPR trace and the actual GPR traces at the location of core A-3. The synthetic signal is based on the convolution of the GPR source wavelet (Berlage wavelet) and the resampled reflection coefficients converted from the gamma density logging of the first 2.5m of core A-3. The synthetic model does not include the attenuation factor,

while the actual GPR signals in profile A-3X and A-3Y are naturally attenuated starting from 200 ns.

Since the density log of the first two sub-sections of core A-3 is well calibrated and its calculated water content agrees well with the measured water content, we used the density data of the first 2.5 meters to simulated its GPR responses (Figure 5.3). Another reason to use the density data of only the first 2.5m of Core A-3 is that the GPR traces of these top sections are strong, which helps in the model evaluation. The model shows the pattern and relative strength of the simulated GPR trace matches the actual traces from both two GPR profiles in two surveying directions. This result indicates that the GPR reflections within the lake sediments are caused by water content change in the sediments.

Combined with the core geochemical analysis, the water content variation is likely related to changes in the lithic input which may be linked to climate variations. We speculate that the layer structure may be made possible by the high organic content of the sediments, and low density giving it a gel-like consistency which allows this structure to be preserved for thousands of years instead of the water rich layers being squeezed shut by the weight of heavier material above.

Our carbon analysis and sediment volume estimation suggest that such a small inland water body as Grassy Pond contains about 29 kg/m^2 carbon. Compared to a well-drained upland forest with a 6-10 kg/m^2 carbon in the soil (Ziegler et al., 2017) and a boggy forest even more than twice that much (S. Ziegler, pers. Comm.), the carbon budget of Grassy Pond is significantly high. Thus, a small fresh water lake like Grassy Pond in Eastern Newfoundland is a particularly good sink for carbon.

References

Aldridge, D. F. (1990). The berlage wavelet. *GEOPHYSICS, 55*(11), 1508-1511.

Annan, A. (1992). *Ground penetration radar workshop notes. Sensors and Software Inc., Mississauga*. Retrieved from

Annan, A. (1999). Practical processing of GPR data. *Sensors and software, Ontario*.

Annan, A. (2009). *Electromagnetic principles of ground penetrating radar* (Vol. 1): chapter.

Annan, A. P. (2005). 11. Ground-Penetrating Radar *Near-Surface Geophysics* (pp. 357-438).

Appleby, P. (2002). Chronostratigraphic techniques in recent sediments *Tracking environmental change using lake sediments* (pp. 171-203): Springer.

Birks, J. B., Lotter, A. F., Juggins, S., & Smol, J. P. (2012). *Tracking environmental change using lake sediments: data handling and numerical techniques* (Vol. 5): Springer Science & Business Media.

Björck, S., & Wohlfarth, B. (2002). 14C chronostratigraphic techniques in paleolimnology *Tracking environmental change using lake sediments* (pp. 205-245): Springer.

Booth, A. D., Endres, A. L., & Murray, T. (2009). Spectral bandwidth enhancement of GPR profiling data using multiple-frequency compositing. *Journal of Applied Geophysics, 67*(1), 88-97.

Bourgeois, J. M., & Smith, G. S. (1996). A fully three-dimensional simulation of a ground-penetrating radar: FDTD theory compared with experiment. *IEEE Transactions on Geoscience and Remote Sensing, 34*(1), 36-44.

Bowman, J. P., & McCuaig, R. D. (2003). Biodiversity, community structural shifts, and biogeography of prokaryotes within Antarctic continental shelf sediment. *Applied and Environmental Microbiology, 69*(5), 2463-2483.

Bradley, R. S. (1999). *Paleoclimatology: reconstructing climates of the Quaternary* (Vol. 68): Academic Press.

Brown, S. R. (1956). A piston sampler for surface sediments of lake deposits. *Ecology, 37*(3), 611-613.

Buchanan, L. (2005). *USING A DUAL FREQUENCY ECHO SOUNDER FOR THE DETERMINATION OF SUSPENDED SEDIMENT IN THE WATER COLUMN*. Paper presented at the Proceedings of the Western Dredging Association 25th Annual Dredging Conference, New Orleans, LA USA.

Budzinski, H., Jones, I., Bellocq, J., Pierard, C., & Garrigues, P. (1997). Evaluation of sediment contamination by polycyclic aromatic hydrocarbons in the Gironde estuary. *Marine chemistry, 58*(1), 85-97.

Calvert, S., & Pedersen, T. (1993). Geochemistry of recent oxic and anoxic marine sediments: implications for the geological record. *Marine Geology, 113*(1-2), 67-88.

Cassidy, N. J. (2009). *Electrical and magnetic properties of rocks, soils and fluids* (Vol. 2): chapter.

Cassidy, N. J., & Jol, H. (2009). Ground penetrating radar data processing, modelling and analysis. *Ground penetrating radar: theory and applications*, 141-176.
Clark, I. D., & Fritz, P. (1997). *Environmental isotopes in hydrogeology*: CRC press.
Clough, J. W. (1976). Electromagnetic lateral waves observed by earth-sounding radars. *GEOPHYSICS, 41*(6), 1126-1132.
Cohen, A. S. (2003). *Paleolimnology: the history and evolution of lake systems*: Oxford University Press.
Cole, J. J., Prairie, Y. T., Caraco, N. F., McDowell, W. H., Tranvik, L. J., Striegl, R. G., . . . Middelburg, J. J. (2007). Plumbing the global carbon cycle: integrating inland waters into the terrestrial carbon budget. *Ecosystems, 10*(1), 172-185.
Crann, C. A., Murseli, S., St-Jean, G., Zhao, X., Clark, I. D., & Kieser, W. E. (2016). First status report on radiocarbon sample preparation techniques at the AE Lalonde AMS Laboratory (Ottawa, Canada). *Radiocarbon*, 1-10.
Daniels, D. J. (1996). Surface-penetrating radar. *Electronics & Communication Engineering Journal, 8*(4), 165-182.
Daniels, D. J. (2004). *Ground penetrating radar* (Vol. 1): Iet.
Davidson, J., Biggar, J., & Nielsen, D. (1963). Gamma-radiation attenuation for measuring bulk density and transient water flow in porous materials. *Journal of Geophysical Research, 68*(16), 4777-4783.
Davis, J., & Annan, A. (1989). GROUND-PENETRATING RADAR FOR HIGH-RESOLUTION MAPPING OF SOIL AND ROCK STRATIGRAPHY1. *Geophysical Prospecting, 37*(5), 531-551.
Dean Jr, W. E. (1974). Determination of carbonate and organic matter in calcareous sediments and sedimentary rocks by loss on ignition: comparison with other methods. *Journal of Sedimentary Research, 44*(1).
Department of Natural Resouces, N. a. l. (2018). Geoscience Atlas.
Douglas, P. M. J., Brenner, M., & Curtis, J. H. (2016). Methods and future directions for paleoclimatology in the Maya Lowlands. *Global and Planetary Change, 138*, 3-24. doi:http://dx.doi.org/10.1016/j.gloplacha.2015.07.008
Eden, D. N., & Page, M. J. (1998). Palaeoclimatic implications of a storm erosion record from late Holocene lake sediments, North Island, New Zealand. *Palaeogeography, Palaeoclimatology, Palaeoecology, 139*(1), 37-58.
Ellis, D. V., & Singer, J. M. (2007). *Well logging for earth scientists* (Vol. 692): Springer.
Fisher, S. C., Stewart, R. R., & Jol, H. M. (1996). Ground penetrating radar (GPR) data enhancement using seismic techniques. *Journal of Environmental and Engineering Geophysics, 1*(2), 89-96.
GEOTEK. (2008). *MSCL Manual*. Retrieved from
Gilbert, R., & Glew, J. (1985). A Portable Percussion Coring Device for Lacustrine and Marine Sediments: RESEARCH METHOD PAPER. *Journal of Sedimentary Research, 55*(4).
Glew, J. R. (1991). Miniature gravity corer for recovering short sediment cores. *Journal of Paleolimnology, 5*(3), 285-287.
Glew, J. R., Smol, J. P., & Last, W. M. (2002). Sediment core collection and extrusion *Tracking environmental change using lake sediments* (pp. 73-105): Springer.

Goodman, D. (1994). Ground-penetrating radar simulation in engineering and archaeology. *GEOPHYSICS, 59*(2), 224-232. doi:10.1190/1.1443584

Gunn, D., & Best, A. (1998). A new automated nondestructive system for high resolution multi-sensor core logging of open sediment cores. *Geo-Marine Letters, 18*(1), 70-77.

Hasted, J. B. (1973). *Aqueous dielectrics*: Chapman and Hall.

Hessler, R. R., & JuMARS, P. A. (1974). *Abyssal community analysis from replicate box cores in the central North Pacific.* Paper presented at the Deep Sea Research and Oceanographic Abstracts.

Heteren, S. V., Fitzgerald, D. M., Mckinlay, P. A., & Buynevich, I. V. (1998). Radar facies of paraglacial barrier systems: coastal New England, USA. *Sedimentology, 45*(1), 181-200.

Jansen, J., Van der Gaast, S., Koster, B., & Vaars, A. (1998). CORTEX, a shipboard XRF-scanner for element analyses in split sediment cores. *Marine Geology, 151*(1), 143-153.

Jol, H. M., & Bristow, C. S. (2003). GPR in sediments: advice on data collection, basic processing and interpretation, a good practice guide. *Geological Society, London, Special Publications, 211*(1), 9-27.

Kamber, B. S., Greig, A., & Collerson, K. D. (2005). A new estimate for the composition of weathered young upper continental crust from alluvial sediments, Queensland, Australia. *Geochimica et Cosmochimica Acta, 69*(4), 1041-1058.

Kansanen, P., Jaakkola, T., Kulmala, S., & Suutarinen, R. (1991). Sedimentation and distribution of gamma-emitting radionuclides in bottom sediments of southern Lake Päijänne, Finland, after the Chernobyl accident. *Hydrobiologia, 222*(2), 121-140.

Karageorgis, A. P., Katsanevakis, S., & Kaberi, H. (2009). Use of enrichment factors for the assessment of heavy metal contamination in the sediments of Koumoundourou Lake, Greece. *Water, air, and soil pollution, 204*(1-4), 243.

Kieser, W., Zhao, X.-L., Clark, I., Cornett, R., Litherland, A., Klein, M., . . . Alary, J.-F. (2015). The André E. Lalonde AMS Laboratory–The new accelerator mass spectrometry facility at the University of Ottawa. *Nuclear Instruments and Methods in Physics Research Section B: Beam Interactions with Materials and Atoms, 361*, 110-114.

Lamoureux, S. (2002). Varve chronology techniques *Tracking environmental change using lake sediments* (pp. 247-260): Springer.

Leroy, S. A., & Colman, S. M. (2002). Coring and drilling equipment and procedures for recovery of long lacustrine sequences *Tracking environmental change using lake sediments* (pp. 107-135): Springer.

Lichte, F. E., Meier, A. L., & Crock, J. G. (1987). Determination of the rare-earth elements in geological materials by inductively coupled plasma mass spectrometry. *Analytical Chemistry, 59*(8), 1150-1157. doi:10.1021/ac00135a018

Livingstone, D. (1955). A lightweight piston sampler for lake deposits. *Ecology, 36*(1), 137-139.

Mahler, B. J., Van Metre, P. C., & Callender, E. (2006). Trends in metals in urban and reference lake sediments across the United States, 1970 to 2001. *Environmental Toxicology and Chemistry, 25*(7), 1698-1709.

Martin, K., Spooner, I., & Williams, P. (2003). *The nature and distribution of postglacial sedimentation in shallow, organic lakes.* Paper presented at the Northeastern Geological Society of America–Atlantic Geoscience Society Joint Meeting.

Moorman, B. J. (1990). Assessing the ability of ground penetrating radar to delineate subsurface fluvial lithofacies.

Moorman, B. J. (2002). Ground-penetrating radar applications in paleolimnology *Tracking environmental change using lake sediments* (pp. 23-47): Springer.

Moorman, B. J., & Michel, F. A. (1997). Bathymetric mapping and sub-bottom profiling through lake ice with ground-penetrating radar. *Journal of Paleolimnology, 18*(1), 61-73.

Moreno-Amich, R., & Garcia-Berthou, E. (1989). A new bathymetric map based on echo-sounding and morphometrical characterization of the Lake of Banyoles (NE-Spain). *Hydrobiologia, 185*(1), 83-90.

Morgan, L., Shanks, W. C., Lovalvo, D., Johnson, S., Stephenson, W., Pierce, K., . . . Webring, M. (2003). Exploration and discovery in Yellowstone Lake: results from high-resolution sonar imaging, seismic reflection profiling, and submersible studies. *Journal of Volcanology and Geothermal Research, 122*(3), 221-242.

Neal, A. (2004). Ground-penetrating radar and its use in sedimentology: principles, problems and progress. *Earth-Science Reviews, 66*(3–4), 261-330. doi:http://dx.doi.org/10.1016/j.earscirev.2004.01.004

Olhoeft, G. R. (1998). *Electrical, magnetic and geometric properties that determine ground penetrating radar performance.* Paper presented at the Proceedings of GPR.

Olsson, O., Falk, L., Forslund, O., Lundmark, L., & Sandberg, E. (1992). Borehole Radar Applied to the Characterization of Hydraulically Conductive Fracture Zones in Crystalline ROCK1. *Geophysical Prospecting, 40*(2), 109-142.

Overpeck, J., Hughen, K., Hardy, D., Bradley, R., Case, R., Douglas, M., . . . Jennings, A. (1997). Arctic environmental change of the last four centuries. *Science, 278*(5341), 1251-1256.

Pachur, H.-J., Wünnemann, B., & Zhang, H. (1995). Lake evolution in the Tengger Desert, Northwestern China, during the last 40,000 years. *Quaternary Research, 44*(2), 171-180.

Ramsey, C. B. (2009). Bayesian analysis of radiocarbon dates. *Radiocarbon, 51*(1), 337-360.

Reynolds, J. M. (2011). *An introduction to applied and environmental geophysics*: John Wiley & Sons.

Sanders, J., & Imbrie, J. (1963). Continuous cores of Bahamian calcareous sands made by vibrodrilling. *Geological Society of America Bulletin, 74*(10), 1287-1292.

Santamarina, J. C., Klein, A., & Fam, M. A. (2001). Soils and waves: Particulate materials behavior, characterization and process monitoring. *Journal of Soils and Sediments, 1*(2), 130-130.

Schindler, D. W., Curtis, P. J., Parker, B. R., & Stainton, M. P. (1996). Consequences of climate warming and lake acidification for UV-B penetration in North American boreal lakes. *Nature, 379*(6567), 705-708.

Scholz, C. A. (2002). Applications of seismic sequence stratigraphy in lacustrine basins *Tracking environmental change using lake sediments* (pp. 7-22): Springer.

Scott, D. B., Mudie, P. J., Vilks, G., & Younger, D. C. (1984). Latest Pleistocene—Holocene paleoceanographic trends on the continental margin of eastern Canada: Foraminiferal, dinoflagellate and pollen evidence. *Marine Micropaleontology, 9*(3), 181-218.

Sensors&Software. (1999). *PulseEKKO 100 User's Guide*. Retrieved from Mississauga, Ontario:

Sensors&Software. (2005). *User's Guide: EKKO Project with Processing, Bridge Deck Condition and Pavement Structrure Modules*. Retrieved from Mississauge, Ontario:

Sheriff, R. E., & Geldart, L. P. (1995). *Exploration seismology*: Cambridge university press.

Søndergaard, M., Jensen, J. P., & Jeppesen, E. (2003). Role of sediment and internal loading of phosphorus in shallow lakes. *Hydrobiologia, 506*(1-3), 135-145.

Sparkes, G., & Dunning, G. (2014). Late Neoproterozoic epithermal alteration and mineralization in the western Avalon Zone: a summary of mineralogical investigations and new U/Pb geochronological results. *Current Research, Newfoundland and Labrador Department of Natural Resources Geological Survey, Report*, 14-11.

St-Jean, G., Kieser, W. E., Crann, C. A., & Murseli, S. (2016). Semi-Automated Equipment for CO 2 Purification and Graphitization at the AE Lalonde AMS Laboratory (Ottawa, Canada). *Radiocarbon*, 1-16.

Theimer, B. D., Nobes, D. C., & Warner, B. G. (1994). A study of the geoelectrical properties of peatlands and their influence on ground-penetrating radar surveying1. *Geophysical Prospecting, 42*(3), 179-209.

TopCon. (2015). *HiPer V Dual-Frequency GNSS Receiver Manual*. Retrieved from

Topp, G. C., Davis, J., & Annan, A. P. (1980). Electromagnetic determination of soil water content: Measurements in coaxial transmission lines. *Water resources research, 16*(3), 574-582.

Vallentyne, J. (1955). A modification of the Livingstone piston sampler for lake deposits. *Ecology, 36*(1), 139-141.

Van Dam, R. L. (2001). Causes of ground-penetrating radar reflections in sediment. *Amsterdan, The Netherlands: Vrije Universiteit, Academic Dissertation, 110p*.

Van Overmeeren, R. (1997). Imaging groundwater ‘steps’ in push moraines by georadar. *Geological Society, London, Engineering Geology Special Publications, 12*(1), 63-73.

Wadleigh, M., Burden, E., Colbo, M., Davenport, P., Gogan, N., & Scott, P. (2002). The Terrestrial Environment: Selected Indicators of Sustainability. In R. E. Ommer (Ed.), *The Resilient Outport: Ecology, economy and society in rural Newfoundland*.

Wall, A. (2017). *Delineating the alteration zone at the Big Easy Prospect using geophysical methods.* (M.Sc.), Memorial University of Newfoundland, St. John's, Newfoundland.

Weber, M. E., Niessen, F., Kuhn, G., & Wiedicke, M. (1997). Calibration and application of marine sedimentary physical properties using a multi-sensor core logger. *Marine Geology, 136*(3), 151-172.

Wright, H. (1990). An improved Hongve sampler for surface sediments. *Journal of Paleolimnology, 4*(1), 91-92.

Wyseure, G., Mojid, M., & Malik, M. (1997). Measurement of volumetric water content by TDR in saline soils. *European Journal of Soil Science, 48*(2), 347-354.

Ziegler, S. E., Benner, R., Billings, S. A., Edwards, K. A., Philben, M., Zhu, X., & Laganière, J. (2017). Climate warming can accelerate carbon fluxes without changing soil carbon stocks. *Frontiers in Earth Science, 5*, 2.

Zolitschka, B., Mingram, J., Van Der Gaast, S., Jansen, J. F., & Naumann, R. (2002). Sediment logging techniques *Tracking environmental change using lake sediments* (pp. 137-153): Springer.